MSc. Dissertation

Evaluation of satellite laser ranging errors associated with pressure sensor height offsets

By

Benedict Paul Mmtoni Barasa

Submitted in partial fulfilment of the requirements for the degree

MASTER OF SCIENCE

in the Faculty of Natural and Agricultural Sciences

University of Pretoria

Pretoria

February, 2020

Evaluation of satellite laser ranging errors associated with pressure sensor height offsets

Supervisor : Prof. Ludwig Combrinck[1,2]

Co-supervisor : Dr. Joel Botai[1,3]

Department : [1]Department of Geography, Geoinformatics and Meteorology, University of Pretoria, Pretoria 0002, South Africa.

[2]Hartebeesthoek Radio Astronomy Observatory (HartRAO), P.O. Box 443, Krugersdorp 1740, South Africa

[3]South African Weather Services, Eco Glades 1 Block B, Eco Park, Centurion 0157, South Africa

Degree : Master of Science

Declaration of Originality

This is to declare that the research work presented here is entirely my own work, unless or otherwise explicitly acknowledged by citation of published and unpublished sources.

This research work has not been submitted previously for assessment in any form to the University of Pretoria or to any other institutions for any other purposes.

Signature: ____________________________

Date: February 10, 2020

Abstract

In this study an evaluation of the satellite laser ranging (SLR) errors associated with pressure sensor height offsets was conducted. Site log sheets from satellite ranging stations were retrieved from the International Laser Ranging Services (ILRS) and examined. It was noted that some log sheets were updated more than a decade ago. In order to ascertain and assess the accuracy of height offsets between the pressure sensor and the telescope invariant point (IVP), an electronic survey was conducted. The feedback received was compared with the site log sheet data and some discrepancies were noted. Furthermore, in order to determine the effect of pressure variations on the range bias, simulations were performed on the same dataset but with different barometric pressure values. This was accomplished by adjusting pressure values in the source code of the analysis software, the Satellite Data Analysis Software (SDAS), before each run. The SDAS was developed by Prof. Ludwig Combrinck at the Hartebeesthoek Radio Astronomy Observatory (HartRAO), South Africa. The focus was to examine the standard deviation of the Observed minus Computed (O-C) results where it was noted that each alteration of pressure caused a variation of the O-C residuals. The differences of pressure sensor height offsets (pressure as a function of height) and SLR range biases were characterized across the SLR network and the station range bias (Rb) examined to determine if there is any correlation with the O-C residuals whenever pressure values changed. Overall, the analysis illustrated that, while the current atmospheric models are robust and capable of achieving sub-millimetre level accuracy, it is crucial to put more emphasis on the site activities that, if unattended will contribute to the ranging errors. It is vital to monitor constantlythe stability of pressure sensors. For example, it was noted in May 2019 at the Geodetic Observatory Wettzell, that their instrument had developed pressure drifting of -0.025 hPa/year. The Wettzell incident underscores the need for regular calibration of pressure instruments especially those that have been in service for more than a decade. Further, the site log sheets ought to be updated regularly and stations that reported estimated height offsets should be encouraged to measure them accurately. Additionally, the height of a meteorological instrument is currently ambiguous and ought to be explicitly stated.

Acknowledgements

This task has been arduous. Throughout my journey often along this lonely path, I have met and made friends. I lost many too along the way. However, despite the challenging times, I wish to sincerely thank and acknowledge Prof. Ludwig Combrinck for having unbelievable faith in me. His support has been magnanimous, just as his noble guidance throughout my studies. He kept me focused, motivated and offered support at my most overwhelming moments. He will remain a true father in my intellectual quest and I am delighted to have lived up to his expectations.

I recognise Dr. Joel Botai who has been like a brother to me. His input in shaping up the final dissertation was crucial. I thank him for his insight, encouragement, contribution and assistance. When the going got tough Dr. Cilence Munghemezulu was at hand to keep me motivated along this journey. Further, I note with appreciation Prof. Serena Coetzee's advice and intervention that kept me enthused. I also extend my gratitude to the University of Pretoria's staff members at the Client Centre, Faculty and especially at the Department of Geography, Geoinformatics and Meteorology for their support. I am deeply indebted to some Hartebeesthoek Radio Astronomy Observatory (HartRAO) staff members and fellow research students who provided a warm and cordial working environment throughout my stay at the station.

This work would not have been possible without the gargantuan support of Nonjabulo Mndawe for being an incessant fountain of encouragement and shoulder to lean on. She remains my epitome of virtue in this regard. Her unrelenting prayers and spiritual conviction helped me find tranquillity in my troubled soul. I thank you Nonjabu!

I am grateful to my parents, for the upbringing that nurtured me to be what I am. Their unwavering military doctrine ensured compliance and high standards which groomed me to be resilient, obedient, and mostly to live with people amicably.

Lastly but not least, those that paid the greatest price are my children Romeo, Ray and Prince Mmtoni. It was never easy to be away from my boys as I thought about them constantly. I therefore inscribe their names deliberately so that they may find solace in seeing themselves in this scholarly book of perpetual reference. I have searched and determined that there is no greater honour than this gesture. I pray that they will all grow with a yearning desire to acquire intellectual excellence and demeanour!

Conference Presentations

Parts of this dissertation were presented at local conferences and workshops orally and/or as abstracts. Supervisors of this research co-authored these presentations as listed:

1. **Barasa, B. P. M.**, Combrinck W. L. and Botai O. J. (2014). Evaluating the effect of meteorological parameters on the accuracy of Satellite/Lunar Laser Ranging (S/LLR) range measurements. Presented at the Department of Geography, Geoinformatics and Meteorology - Centre for Geoinformation Science - Space geodesy, Earth and atmospheric observation research focus group, 10th March 2014, University of Pretoria.
2. **Barasa, B. P. M.**, Combrinck W. L. and Botai O. J. (2014). Evaluating the effect of meteorological parameters on the accuracy of Satellite/Lunar Laser Ranging (S/LLR) range measurements. Presented at the Science and Technology Train and Space Geodesy Observatory Workshop, Matjiesfontein, Cape Town.
3. **Barasa, B. P. M.**, Combrinck W. L. and Botai O. J. (2015). The effect of incorrect meteorological measurements on Lunar/Satellite ranging solution. Presented at the 5th Combined Science and Technology Train and Space Geodesy Observatory Workshop. Matjiesfontein, Cape Town, South Africa.

Table of Contents

List of Figures

List of Tables

Abbreviations

Abbreviation	**Details**
AIRS	Atmospheric Infrared Sounder
ANOVA	Analysis of Variance
CCR	Corner Cube Retroreflectors
CDDIS	Crustal Dynamics Data Information System
CNES	Centre Nationale d'Etudes Spatiale (France)
CPF	Consolidated Prediction Format
CRD	Consolidated Laser Ranging Data format
DORIS	Doppler Orbitography and Radiopositioning Integrated by Satellite
ECMWF	European Center for Medium Weather Forecasting
EOP	Earth Orientation Parameters
ESA	European Space Agency
EU	European Union
FAGS	Federation of Astronomical and Geophysical Data Analysis Services
GEO	Geostationary Earth Orbit
GGOS	Global Geodetic Observing System
GLONASS	Globalnaya Navigatsionnaya Sputnikovaya Sistema
GNSS	Global Navigation Satellite Systems
GPS	Global Position System
GSFC	Goddard Space Flight Centre
GSO	Geosynchronous Orbit
HartRAO	Hartebeesthoek Radio Astronomy Observatory
HEO	High Earth Orbit
IAC	Information and Analysis Center
IAG	International Association of Geodesy
ICRF	International Celestial Reference Frame
IERS	International Earth Rotation Service
IGS	International GNSS Service
IGSO	Inclined Geosynchronous Orbit
ILRS	International Laser Ranging Services
IRNSS	Indian Regional Navigational Satellite System

Abbreviation	**Details**
ITRF	International Terrestrial Reference Frame
IUGG	International Union of Geodesy and Geophysics
IVP	Telescope Invariant Point
IVS	International VLBI Service
LAGEOS	LAser GEOdynamics Satellite
LOD	Length of Day
LEO	Low Earth Orbit
LLR	Lunar Laser Ranging
MANOVA	Multivariate Analysis of Variance
MEO	Medium Earth Orbit
MF	Mapping Functions
MJD	Modified Julian Date
MOBLAS	Mobile Laser System
NASA	National Aeronautics and Space Administration
NCEP	National Center for Environmental Prediction
O-C	Observed minus Computed
P	Pressure
ppm	Parts per million
QZO	Quasi-Zenith Orbit
QZSS	Quasi-Zenith Satellite System (Japan)
Rb	Range bias
RH	Relative Humidity
RMS	Root Mean Square
RNSS	Regional Navigation Satellite System (India)
S/LLR	Satellite/Lunar Laser Ranging
SAO	Smithsonian Astrophysical Observatory
SD	Standard Deviation
SDAS	Satellite Data Analysis Software
SLR	Satellite Laser Ranging
SRP	Station Reference Point
T	Temperature

Abbreviation	**Details**
ToF	Time-of-Flight
TRP	Telescope Reference Point
UN	United Nations
UNGGI	United Nations Global Geospatial Information
UN-GGIM	United Nations Committee of Experts on Global Geospatial Information Management
UT	Universal Time
VLBI	Very Long Baseline Radio Interferometry
WGS	World Geodetic System
ZD	Zenith Delay

Chapter 1 Introduction

Satellite laser ranging (SLR) and Lunar laser ranging (LLR) are space geodetic techniques which use short-pulse laser transmitters and optical receivers (single or multiple photon) as well as timing electronic devices to record the total time of flight (ToF) of a laser pulse from ground stations to retro-reflectors affixed to Earth orbiting satellites and located on the Moon respectively. With the SLR technique, satellites equipped with a corner cube reflector or an array of corner cube retroreflectors (CCRs) are tracked by an optical telescope, which has a sensitive light detector at its receiving end (Combrinck 2010). Regarding the LLR, there are 5 retroreflector arrays on the Moon placed by both the Apollo program (USA) and the Soviet Lunokhod program (Russia). Typically, for LLR to be successful, it requires larger telescopes than SLR, as the distance to the Moon is much greater than the distance to an Earth orbiting satellite. In both cases the signal amplitude reduces by the inverse of the range cubed.

The international laser ranging activities fall under the auspices of the International Laser Ranging Service (ILRS, see https://ilrs.cddis.eosdis.nasa.gov), which provides SLR and LLR data and their derived products to support research in geodesy, geophysics, Lunar science and fundamental constants. Other areas of operational applications include the International Terrestrial Reference Frame (ITRF) and its ties to the International Celestial Reference Frame (ICRF) through the Earth orientation parameters (EOP). In addition, SLR and LLR techniques are routinely used for the calibration of satellite microwave tracking, monitoring the three-dimensional deformations of the solid Earth and tectonic plate motion. During ranging, the troposphere causes bending of the ideal straight path of the laser pulse that results in an increase in the apparent path length. This curvature forms the largest error component in laser ranging measurements. Given the fundamental importance of laser ranging as a space geodetic technique, there is need for the development of more accurate, improved and robust atmospheric models to support these high precision geodetic and geophysical applications. According to Hulley and Pavlis (2007), current models assume a spherically symmetric atmosphere. Although the assumption of uniformity makes it easier to model the atmosphere contribution to the range bias, it ignores localized atmospheric perturbations.

There are several weather instruments used globally to collect meteorological data for SLR use. Rarely however, are exact measurements of the same parameters obtained using different instruments or even same instruments at the same location. These differences are attributed to the sensitivity of the instruments, the impracticability of having the instruments at the same spot, the calibration and installation procedures. There are two categories of weather information relevant to SLR ranging. The first category comprises meteorological observations such as temperature, humidity and pressure used during post-processing of SLR observations and are incorporated with normal point data. The second category consists of wind speed and direction, rainfall, visibility, dew point and cloud conditions that are vital for SLR observation scheduling. Ranging cannot be conducted during cloudy or rainy days as this inhibits the visibility of the spacecraft while rain will cause damage to the electronics of the ranging system. This study focuses on the influence of category one meteorological data on the SLR.

The emphasis of this research was to investigate the influence of incorrect pressure sensor height on the SLR determined range. The resulting range error is contained within the Observed - Computed (O-C) residuals and affects other parameters such as station position. The observed range (O) is the SLR measured range whereas the computed range (C) is the modelled range. This observed range must be corrected for an additional delay (apparent range increase) due to refraction in the atmosphere; this additional delay is modelled by using meteorological parameters and the barometric pressure plays the error component in this modelling. One of the objectives of SLR is to attain an accuracy of 1 mm in ranging to allow accurate modelling and thus the estimation of several parameters (gravity field, station position, satellite orbit, EOP, relativistic parameters etc.). In this study, determination of the exact location of the barometric pressure sensor centre with respect to the SLR station reference point (SRP) is sought. The terms SRP, the IVP and a reference monument, although often used interchangeably, refer to different physical or virtual entities. The differences and similarities are addressed to determine whether usage of the terms SRP, IVP and monument are used appropriately. It is also examined if the correct values of meteorological instrument height minus the IVP are being used during range determination.

1.1 Problem outline

SLR stations are all equipped with integrated meteorological units containing a pressure sensor. The exact offset in height between the IVP and the pressure sensor varies from station to station. What is the effect in theory and in practice of an erroneous offset on the range solution?

The intention of this study was to evaluate the magnitude of errors as expressed by the standard deviations of O-C residuals resulting from incorrect pressure measurements. The on-site instruments were identified, and site log sheets examined for any system biases or physical changes that may have been recorded. Such changes include physical movement of the instrument from initial location, adjustment of instrument height, periodic calibration, a complete replacement of an obsolete or irreparable unit (by a similar unit – make and model, same make but newer model, or different make).

Other factors that may cause pressure data anomalies are due to instrument aging or configuration exhibiting random errors or causing a constant bias. It was noted that some sites use estimated offset values.

In this study, the SLR data processing involves a maximum of twenty iterations, where the solve for parameters are adjusted by applying the least squares approach on each iteration. A solution is derived when no further improvement in the O-C residuals are found. An observation is detected as an outlier and rejected if the O-C residual of a specific observation is higher than a pre-set value (0.8 sigma) of the mean of the O-C residuals. Consequently, some stations end up with insufficient data for analysis. Loss of such critical data renders the station unsuitable for contribution towards better ranging solutions. The poor data quality sites especially in the Southern Hemisphere may suffer from reduced funding with more funding being redirected to more productive sites, yet the SLR network is skewed in favour of the Northern Hemisphere. In order to realize ranging solutions at millimetre level both ranging precision and accuracy must be achieved and sustained.

1.2 Rationale of the project

Globally, 37 of the 45 or 82% of the SLR ranging sites are in the Northern Hemisphere, making it critical that the 8 in the Southern Hemisphere provide high quality data. The South African site at the Hartebeesthoek Radio Astronomy Observatory (HartRAO), where this study was conducted, is a global fiducial site equipped with all four of the main space geodetic instruments, which are GNSS, VLBI, DORIS and SLR. The HartRAO site is also uniquely equipped with two active SLR telescopes, and it is the only active ILRS station on the African continent. The other three co-location sites are: Greenbelt MD in the USA, Badary in Russia and Yarragadee in Australia as confirmed by the Secretary, ILRS Central Bureau, Carrey Noll on 6th December 2018 through personal correspondence.

Intervention to lessen site errors must be made to ensure that the SLR data from the HartRAO site is of good quality. Usable data will ensure that the Southern Hemisphere also contributes substantially towards ILRS products such as station positions within the ITRF, calibration of satellite orbits and EOP. The ILRS EOP describes the irregularities of the Earth’s rotation. They are the parameters which provide the rotation of the ITRS to the ICRS as a function of time (https://www.iers.org). Through further personal correspondence with Carey Noll in July 2018 she confirmed that although La Plata in Brazil is on the ILRS map, it was not generating data. Four of the eight working southern SLR stations are in two countries, namely Australia and South Africa. These stations are Yarragadee and Mt. Stromlo which are located in Australia while Hartebeesthoek is located in South Africa. The other Southern Hemisphere ranging sites are Tahiti (France Polynesia), Arequipa (Peru), San Juan (Argentina), La Plata (Argentina) and Brasilia (Brazil).

Some of the more problematic areas to investigate include measuring the exact position of the meteorological instruments and the precise identification and determination of the SRP. Ideally, professional surveyors perform this function during site-tie surveys.

In addition, proper recording and updating of any SLR system activities in the station log sheet at the ILRS repository is crucial. Overall, the following were key questions for determination:

a) What are the current offset heights of the meteorological instruments?
b) Are these offsets measured or estimated?
c) What is the unit of measure and the subsequent error margin of the offset height of these instruments?
d) What effect if any does an error in the offset heights have on the derived O-C residuals?
e) If the error is determined to be significant, how can this anomaly be alleviated?

1.3 Aim and specific objectives

The aim of this study is to evaluate the ranging errors introduced by pressure sensor height offsets in SLR measurements.

In order to accomplish the aim, the following specific objectives are addressed.

1. To assess the accuracy of the height offsets between meteorological sensors and the SLR I recorded in the SLR site log sheets.
2. To determine the effect of pressure differences due to simulated sensor height offsets on the SLR range biases.
3. To characterize the differences of the sensor height offsets and SLR range biases across the SLR network.

1.4 Problem Statement

The accuracy of current space-based geodetic systems such as SLR, Very Long Baseline Interferometry (VLBI), the Global Positioning System (GPS) and Doppler Orbitography and Radiopositioning Integrated by Satellite (DORIS) or Satellite Altimetry all suffer from limitations due to signal (radio or optical) propagation through the atmosphere. The extent of this error budget is however dependent on the nature of the signal form as well as its wavelength.

Laser ranging measurements are greatly affected by the troposphere since optical signals are used. Tropospheric delay can be separated into the wet and the dry components. The dry component accounts for 90% and the wet component for 10% of the entire troposheric delay as noted by Hegarty and Chatre (2008). Estimates to the dry component can be made accurately. However, the wet component is difficult to model due to the high non-linear variability of the atmosphere caused by variations in the water vapour content, temperature, air pressure and altitude.

In laser ranging analysis, modelling of atmospheric refraction involves the determination of the atmospheric delay in the zenith direction and the subsequent projection to a given elevation angle, using mapping functions (MF). The current models of atmospheric delay computation for SLR observations assume a spherically symmetric atmosphere. The assumption ignores the exact horizontal gradients in the refractive index of the atmosphere at a specific ranging site. To improve these existing atmospheric delay models, horizontal gradients in the atmospheric refractive index need to be understood, modelled and adapted for a specific site. In this regard, it is vital to determine the suitability of certain parameters, especially given the skewed distribution of satellite ranging sites to represent a specific location in the Southern Hemisphere. Such a provision may cater for each site’s unique geographic position and characterize the local atmospheric influence on the estimated SLR range bias caused by the atmosphere. The SLR measurements and derivation of the O-C is greatly influenced by the ranging site’s measurements of the atmospheric temperature, relative humidity and atmospheric pressure.

At HartRAO, the actual meteorological unit height was surveyed and measured to millimetre level accuracy. These measured values were compared with the recordings in the site log sheet at the ILRS and found to be inconsistent. Upon enquiry, it was determined that a mounting bracket for the meteorological unit had been replaced. It was not clear when these adjustments were made. The instrument was later repositioned to its original position. A survey to the other ranging sites confirmed that some log files were not updated timeously causing incorrect heights to be used during range determination.

1.5 Document structure

This dissertation has five chapters. The key highlights in Chapter 1 are the problem outline, rationale as well as the aim and objectives, and the problem statement. Chapter 2 contains an introduction to space geodesy and a brief overview of the four main space geodetic techniques. It further provides a review of the laser ranging technique. Chapter 3 contains the methodology while the results and a discussion of the results are presented in Chapter 4. The conclusion and recommendations are contained in Chapter 5 followed by References. The technical specifications of a MET4 meteorological instrument are included in Appendix A1. Appendix A2 contains a description of the ILRS format for SLR data. The plots depicting changes in the standard deviation of O-C and stepwise variation of pressure are contained in Appendix A3. The charts for the clustered standard deviation of O-C residuals at different pressure levels are included as Appendix A4. The ILRS system performance standards are contained in Appendix A5 while Appendix A6 contains the SLR global performance report card. An overview of the Consolidated Laser Ranging Data (CRD) format is in Appendix A7 and lastly Appendix A8 contains a list of tables with summaries of statistics and Analysis of Variance (ANOVA) for O-C and Range Bias (Rb).

Chapter 2 Background and introduction of space geodetic techniques

2.1 Introduction to space geodesy

What is Geodesy? The classical definition by Friedrich Robert Helmert (1843 – 1917) states that geodesy is the "Science of measurements and mappings of the Earth's surface" (Plag and Pearlman, 2009). The inclusion of "measurements' and 'mappings' implies that this field of science also entails the shape, size, gravity field as well as its position in space. The key words in geodesy are *high precision measurements* using different space geodetic techniques. In the past, geodesy was done by using Earth-based surveying tools to measure the distances between points. Today space based tools are used to measure points on the Earth's surface. In order to enable SLR products to become more suitable for practical applications, the Global Geodetic Observing System (GGOS) set the O-C ranging error margin to 1 mm. Consequently, the ILRS network nodes continue to improve their solutions to meet the set target.

Why high precision?

According to the ILRS, space geodesy allows us to quantify changes of the Earth system in space and time: Earth rotation, its gravity field and their irregularities, global and regional sea level variation, tectonic motion and deformation, post-glacial rebound, geocenter motion, large scale deformation due to Earthquakes, local subsidence and other ruptures as well as crustal dislocations. Furthermore, only space geodesy can realize precise satellite orbit determination for satellite positioning and other practical applications in geo-information which fundamentally depend on the availability of a global reference system.

Geodetic research is multi-disciplinary and incorporates facets from geosciences, mathematics, engineering, computing and communication technology. Briefly, geodesy plays a key role in monitoring the following:

- the liquid Earth, such as sea level and ice cover in the polar regions,
- variations in the Earth's rotation, for example, the length of day (LOD) and polar motion, and
- the Earth's atmosphere, for example, tropospheric composition.

There are four main space geodetic techniques namely the Global Navigation Satellite Systems (GNSS), SLR, Very Long Baseline Radio Interferometry (VLBI), and Doppler Orbitography and Radiopositioning Integrated by Satellite (DORIS) as described by Combrinck (2010). Some if the main products and applications of these space geodetic techniques are highlighted below. The specific techniques that contribute to each are given in brackets.

International Terrestrial Reference Frame, ITRF:

i. Station positions and velocities (SLR, GNSS, VLBI, DORIS).
ii. Terrestrial Reference Frame (TRF) scale and temporal variations (SLR, VLBI).
iii. Network densification (GNSS).
iv. Homogenous network distribution (DORIS).

International Celestial Reference Frame, ICRF:

i. Precise orbit determination (VLBI).
ii. Accurate satellite ephemerides (SLR, GNSS, DORIS).
iii. Calibration and validation for remote sensing missions and instruments (SLR, GNSS).
iv. Sea level monitoring (SLR, GNSS, DORIS).

Earth Orientation Parameters, EOP:

i. Polar motion and rates (SLR, VLBI, GNSS, DORIS).
ii. Length-of-day (SLR, GNSS, DORIS).
iii. UT1-UTC and long-term stability of nutation (VLBI).

Fundamental Physics:

i. General relativity and alternative theories (SLR/LLR).
ii. Light bending, time dilation (VLBI).

The atmosphere:

i. Tropospheric zenith delays (GNSS, VLBI).
ii. Global maps of ionosphere mean electron content (GNSS, DORIS).
iii. Limb sounding for global profiles of water vapour (GNSS).

Gravity:

1. Static and time-varying coefficients of the Earth's gravity field (SLR, DORIS).
2. Total Earth mass (SLR).
3. Temporal variations of network origin with respect to Earth centre of mass (SLR).

Each of these techniques has a unique contribution to geodesy, and where applicable they are used to complement one another in enhancing a deeper understanding of various geophysical phenomena. For example, the science requirement on the ITRF is becoming more demanding and stringent, aiming for a precise reference frame at the level of 1 mm and 0.1 mm/yr stability (Gross,2009). The accuracy of space geodetic measurements is therefore critical.

The main space geodetic techniques are illustrated in Figure 1 and explained briefly in the following subsections.

Figure 1. An illustration of the four main space geodetic techniques. The illustration represents a generic GNNS satellite, although in reality they are of different shapes and sizes; SLR's geodetic satellites like LAser GEOdynamics Satellite (LAGEOS) are spherical; VLBI relies on Earth based parabolic dishes; DORIS has dedicated antennas on ground stations. Source: NASA, 2018.

2.1.1 Global Navigation Satellite Systems (GNSS).

GNSS is a worldwide set of satellite navigation constellations, civil aviation augmentations, and user equipment (Hegarty and Chatre, 2008). This system is integrated into the International GNSS Service (IGS), formerly the International GPS Service. It is a voluntary federation of more than 200 worldwide agencies that pool resources with permanent GPS and Globalnaya Navigatsionnaya Sputnikovaya Sistema (GLONASS) data to generate precise GPS and GLONASS products (NASA, 2018) while other regional constellations for example, Galileo from the European Union (EU) segment, BeiDou concentrating on the Chinese region, the Quasi-Zenith Satellite System (QZSS) for the Japanese portion, and the Indian Regional Navigational Satellite System (IRNSS) covering the Indian sub-continent are being gradually integrated. The foundation of the IGS is a global network of over 450 permanent and continuously operating stations of geodetic quality which track signals from GPS. Increasingly signals from GLONASS, Galileo, Bei-Dou, QZSS, and several Space-Based Augmentation Systems (SBAS) are also tracked (Johnston et al., 2017). The general principle of GNSS is illustrated in Figure 2. The satellites transmit ranging codes on two radio-frequency carriers, allowing the locations of GNSS receivers to be determined. The IGS centres manage approximately 10 terabytes (TB) of data (over 100 million files) with around 10,000 regular users per year (Fisher et al. 2016).

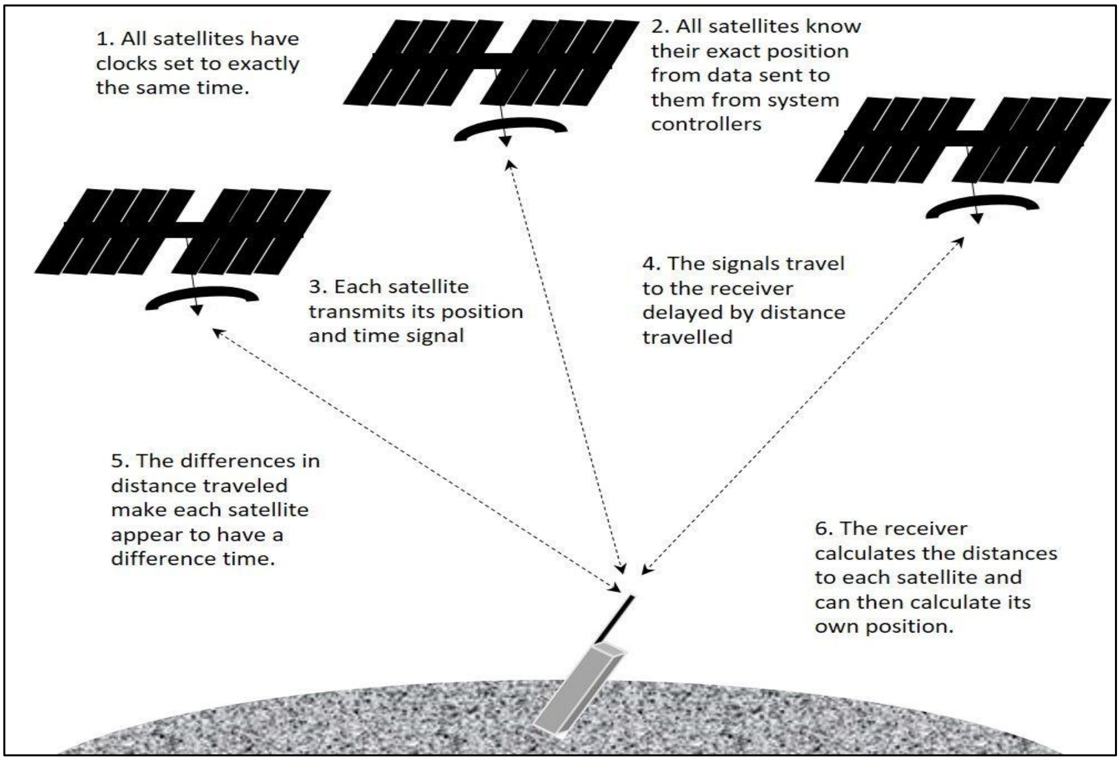

Figure 2. An illustration of how the GNSS technique works. The GNSS receivers detect, decode, and process signals from the GNSS satellites. Source: IGS, 2018.

The global distribution of current IGS tracking stations is depicted in Figure 3. This conglomeration provides the highest quality data and products in support of GNSS Earth science research, as well as many other multidisciplinary applications including education. (Mohinder et al. 2013). Some of the GNSS satellites are geosynchronous (GSO), while others are geostationary (GEO). Satellites in GEO and GSO orbits have a period of one sidereal day (approximately 24 hrs) while semi-synchronous satellites take half a sidereal day (about 12 hrs). All GEO satellites are GSO but not vice versa since a GEO satellite must be on the Equatorial plane. The GNNS technique relies on the following satellite segments:

- GPS (USA) – operates in 6 orbital planes with 24 active satellites at an inclination angle of 55° (NASA, 2018).
- GLONASS (Russia) – operates in 3 orbital planes with 24 active satellites at an inclination of 64.8° (IAC, 2018).
- European Union's (EU) Galileo has 9 operational satellites in 3 equally spaced orbital planes and have an inclination angle of 56° (ESA, 2018).
- Chinese's BeiDou (also referred to as COMPASS) has 15 operational satellites of which 3 are medium Earth orbit (MEO), 6 GEOs and 6 are in the Inclined Geosynchronous Orbit (IGSO) at 55° inclination angle (IGS, 2018).
- Japan's QZSS consists of 4 satellites with 3 in the Quasi-Zenith Orbit (QZO) and 1 GEO, at an inclination angle of 41° (QZSS, 2018).
- India's IRNSS has 7 operational satellites, 3 are GEOs and 4 GSOs. The 8th satellite (IRNSS-1I) was launched on 12th April 2018 (ISRO, 2018).

The data obtained by using the GNSS technique enhances the study/studies of the motions of tectonic plates, displacements associated with earthquakes, and Earth orientation.

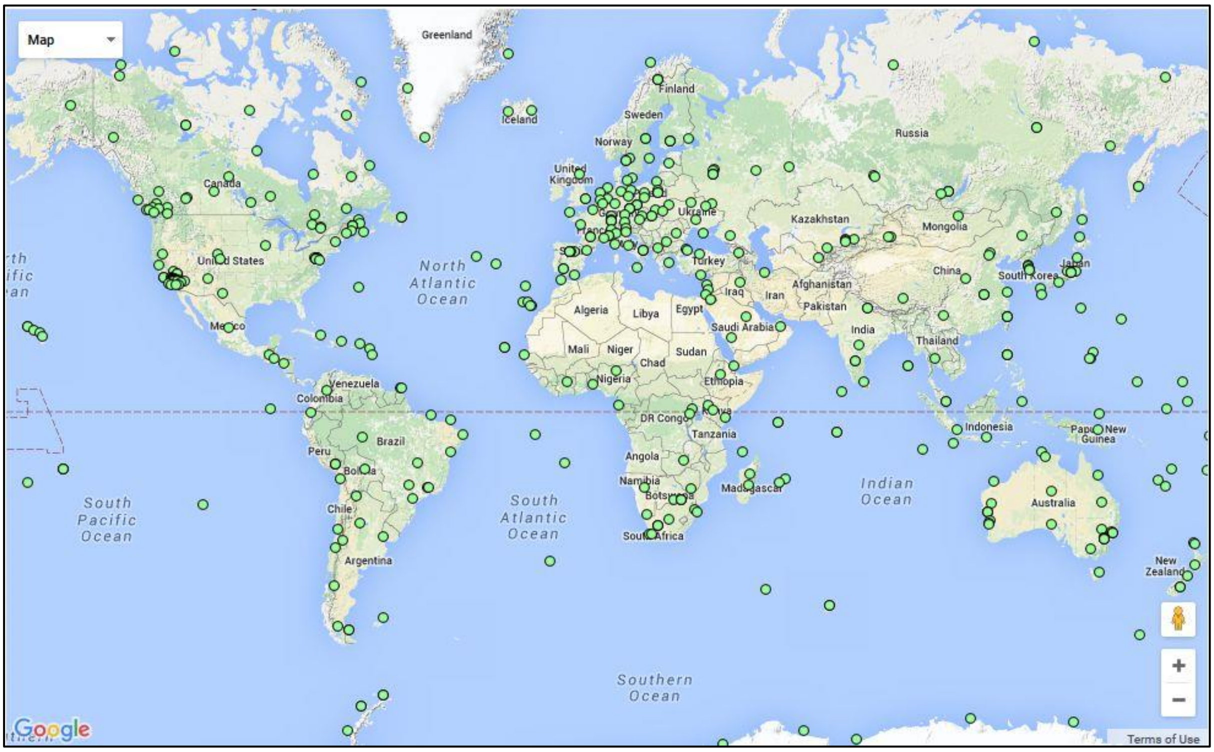

Figure 3. This is a map showing the locations of current IGS tracking stations on Earth. These stations are well distributed across the globe. Source: NASA, 2018.

2.1.2 Very Long Baseline Interferometry (VLBI)

Another space geodetic technique is the VLBI, which falls under the International VLBI Service for Geodesy and Astrometry (IVS). The IVS is an international collaboration of organizations that operate or support VLBI instruments and activities. The radio telescopes in a VLBI network can be separated by thousands of kilometres, where all the telescopes observe the same astronomical sources at the same time. Signals from all the telescopes in the network is then combined. These networks of radio telescopes can be used for both astronomical or geodetic VLBI observations. The signal from a radio source is detected at each of the radio telescopes in the network, where it is then amplified, digitized and sent to a correlator, where the signals from each telescope is then combined. This technique is essential for the realization of both terrestrial and celestial reference frames since its point of reference for its observations are quasars which are distant extragalactic radio sources that appear to be nearly fixed in angular position (Petrachenko et al. 2012). With the latest innovations in computing technology, the traditional sequence of storing data on disks or tapes and then shipping them to correlation centres is being replaced by the e-VLBI technique where signals are stored on high- density disks and sent over high-speed data networks of up to 32 Gbps. The correlator cross-correlates and Fourier transforms the signals from each pair of antennas and the output is used to determine the brightness distribution of the sky at radio frequencies (Middleberg and Bach 2008) for astronomical VLBI. However, for geodetic VLBI, the output is used to determine source positions or in the reverse process station coordinates. The main observable of the VLBI technique is the geometric delay. An illustration of the VLBI technique is shown in Figure 4 while the global network distribution of VLBI telescopes that participate in geodetic observations are illustrated in Figure 5.

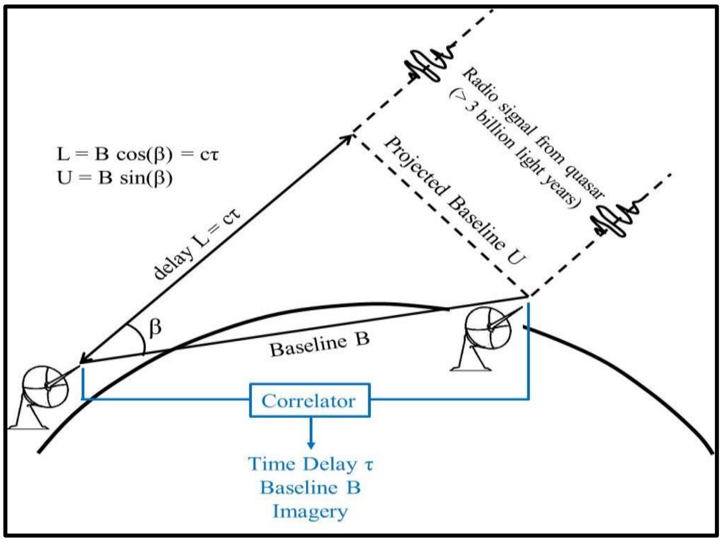

Figure 4. An illustration of the VLBI technique, which uses radio telescopes for astronomical or geodetic observations. The geometry delay, L, is due to the difference in arrival time of a radio signal at two observing stations, where B is the distance between the two stations, called a baseline, and U is the projected baseline. The main observable of the VLBI technique is the geometry delay. Source: NASA, 2018.

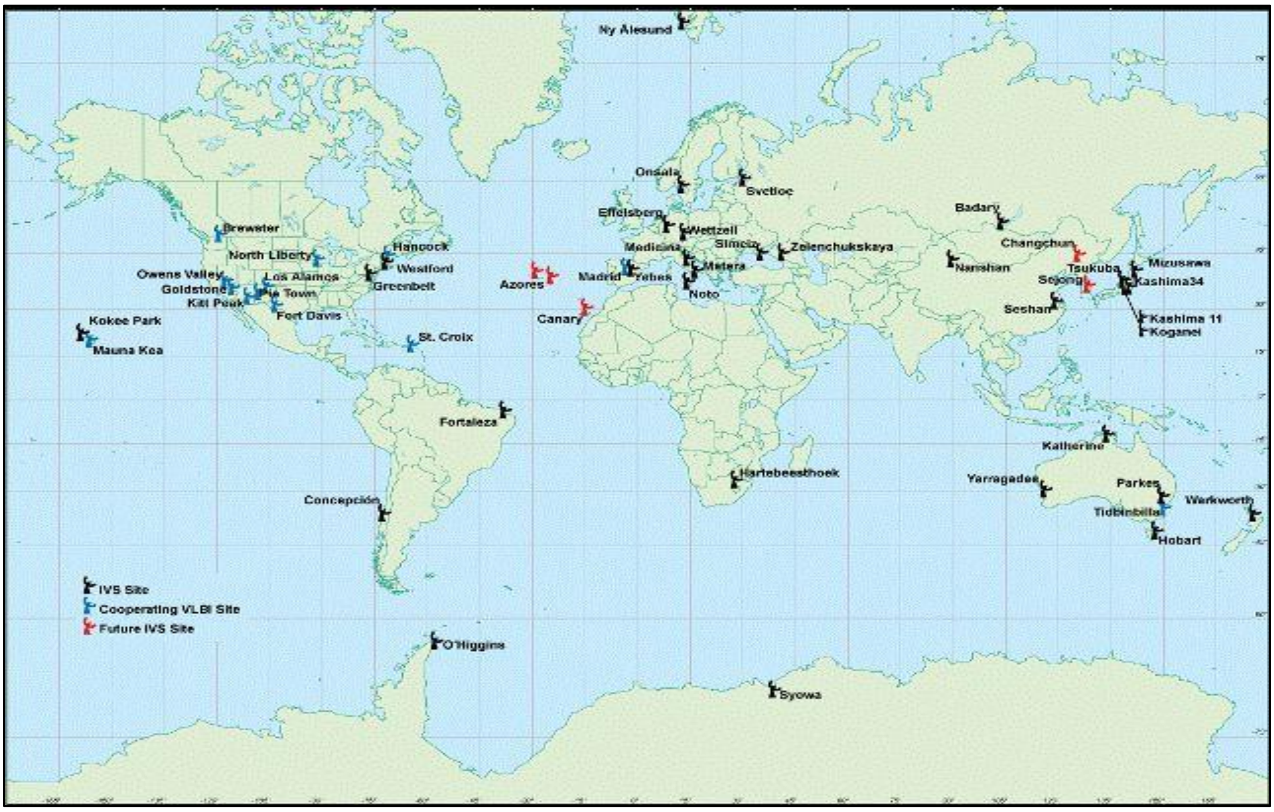

Figure 5. The global IVS network that provides data and products such as the International Terrestrial Reference Frame (ITRF), the International Celestial Reference Frame (ICRF), and Earth orientation parameters (EOP). The geodetic VLBI network has unequal distribution of stations over the globe, with poor geometry in the Southern Hemisphere. Source: NASA, 2018.

2.1.3 Doppler Orbitography and Radiopositioning Integrated by Satellite (DORIS)

A French system named DORIS is another space geodetic technique that is administered by the International DORIS Service (IDS). The IDS provides a service to support geodetic and geophysical research activities through DORIS data and derived products. The DORIS technique was developed to provide precise orbit determination and high accuracy location of ground beacons for point positioning. This approach entails making an accurate measurement of the Doppler shift on radio frequency signals emitted by a dense network of ground beacons and received on the satellites equipped with DORIS receivers (Doornbos and Willis, 2007). An illustration of DORIS is shown in Figure 6 and its global network of ground beacons is indicated in Figure 7.

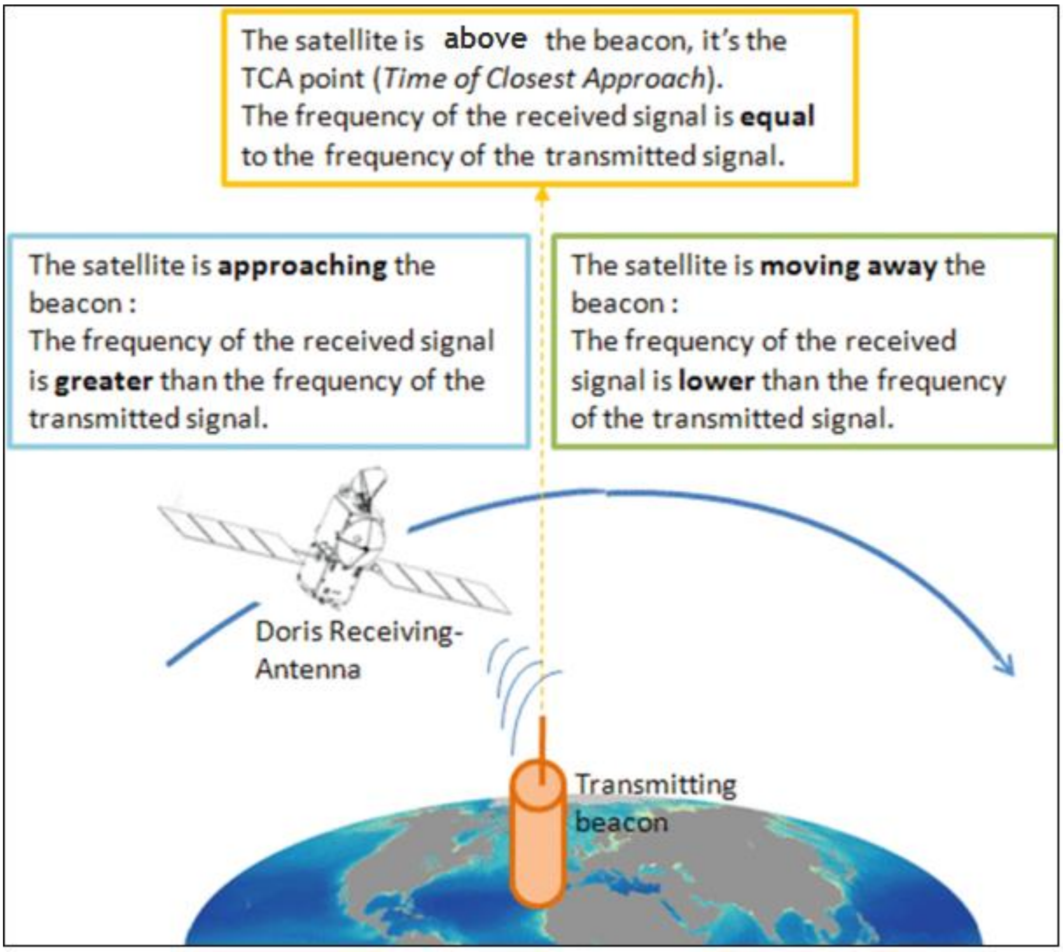

Figure 6. An illustration of the DORIS technique in which the signals are received by the spacecraft transmitted from the Earth based beacons. DORIS plays a complimentary role alongside SLR, VLBI and GNSS in space geodetic research. Source: AVISO+Satellite Altimetry Data, 2018.

Figure 7. This is a map showing the locations of current DORIS ground based beacons. The network shows well-balanced nodes in both the Northern and Southern Hemispheres. Source IDS, 2018.

The other space geodetic technique is SLR and LLR and since the crux of this study is focused on this technique, it will be expounded in more detail.

2.2 History of Laser Ranging

2.2.1 Introduction to Laser Ranging

The current geometry of ranging sites favours the Northern Hemisphere which has 36 of the 45 active SLR ranging stations in the ILRS network. Pearlman and Taggart (ILRS Annual Report 1999) concluded that *"Laser Ranging is the only calibration method for the other modern space geodetic techniques because in the optical and near infrared domain of the electromagnetic spectrum the signal delays due to the Earth's atmosphere may be taken into account on the level of one centimetre or better, provided pressure, temperature and humidity are continuously monitored at the SLR/LLR tracking sites"*. This observation was made nearly twenty years ago, and it still stands undisputed.

Further, the authors also noted that SLR observations only rely on the following factors:

- the constancy of the speed of light in vacuum (which is the basis of the theory of relativity),
- modern Laser technology producing very short light pulses of 50 – 100 picoseconds with a very small divergence,

- artificial or natural satellites being equipped with retroreflectors to send back the light in the incident direction and,
- extremely accurate time interval counters or event timers allowing measurement of the light travelling time with picosecond resolution.

Given that the accuracy of the laser ranging technique is dependent on the continuous monitoring of atmospheric conditions at the ranging sites, the effects of pressure measurements on the ranging solutions are investigated in this study.

2.2.2 Satellite /Lunar Laser Ranging (S/LLR).

Both SLR and LLR (S/LLR) are space geodetic techniques which use short-pulse laser optical receivers and timing electronics to measure a two-way ToF from ground stations to retroreflector arrays on Earth orbiting satellites or the Moon (Shimon et al. 2014).

This technique is used to accurately measure the distance from ground stations to retroreflectors (see Figure 8) on Earth orbiting satellites or on the Moon.

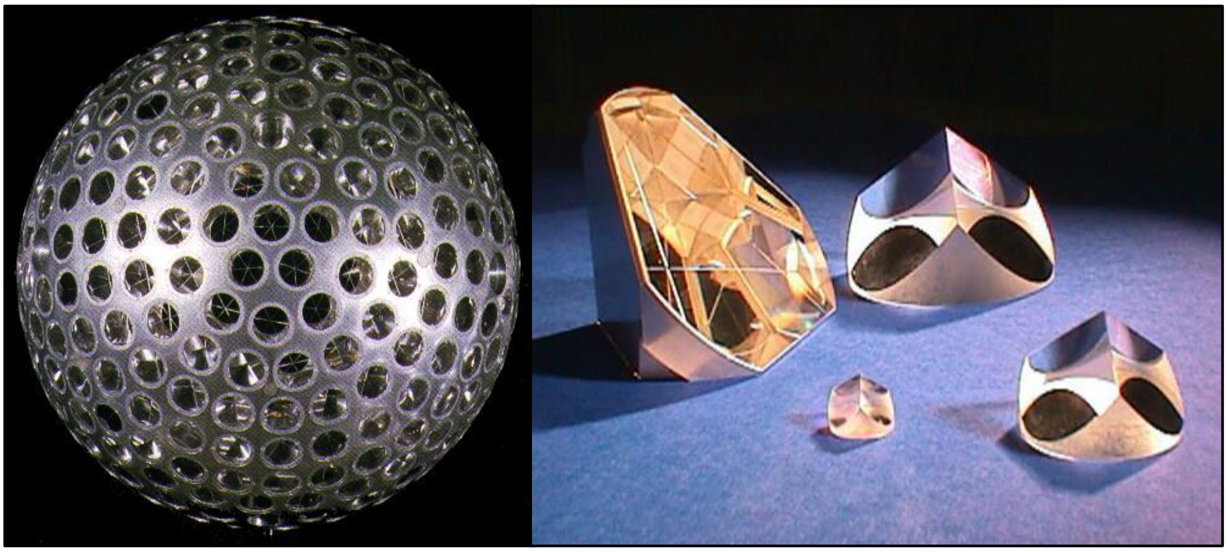

Figure 8. The LAGEOS Satellite (Left Panel) is a 60 cm sphere that is covered with 426 retroreflectors of which 422 are made of glass while 4 are germanium for infrared signalling. Prototypes of retroreflectors are inset (Right Panel). Source: NASA, 2018.

By making these measurements over a long time, the absolute positions of the stations relative to the centre of mass (CoM) can be determined, enabling computation of any changes in the positions of the stations relative to one another (NASA, 2018). The SLR technique is the most precise approach for realizing the physical centre of mass of the entire Earth system and it is one of the fundamental space geodetic techniques used in defining the ITRF. The Earth’s CoM is considered as the natural origin for the ITRF (ILRS). Precise and accurate measurements have made it possible to detect small irregularities in the Earth’s rotation, caused by the movement of mass in the atmosphere and oceans, and polar motion - the migration of the planet’s axis of rotation.

The United Nations Committee of Experts on Global Geospatial Information Management (UN-GGIM) adopted the resolution “Global Geodetic Reference Frame for Sustainable Development” on 26th February 2015 underscoring the importance of a global geodetic frame of reference. The resolution outlines the value of ground-based observations and remote satellite sensing for tracking changes in populations, ice caps, oceans and the atmosphere over time. These geospatial measurements support sustainable development, sound policymaking, climate change monitoring and natural disaster management.

To improve global participation and collaboration, the United Nations Global Geospatial Information (UNGGI) acknowledges that ranging solutions have a wide range of applications in transport, agriculture and construction among other civil applications (UN, 2018). The illustration in Figure 9 depicts the principle of the laser ranging technique while the global network of SLR stations is depicted in Figure 10.

In this technique, a very short high-powered laser pulse is fired to a satellite that has retroreflectors. These retroreflectors reflect the laser back to the transmitting station where photons are detected and measured. The ToF is used to compute the distance after factoring in the atmospheric refraction effect, site related biases and hardware or system biases. As noted by Combrinck, (2010) not only is SLR a valuable tool to measure these small centimetre-level station position variations resulting from geophysical processes but it also provides important contributions to the development of gravity models of the Earth.

One of the notable involvements relates to the use of SLR data from GEOS-1 (20th January 1977 through to 14th December 1978) in the development of gravity model EGM96. This ranging technique is also instrumental for observing the slow-varying geodynamic processes of Earth and the long wavelength components of the gravity field and their variation in time.

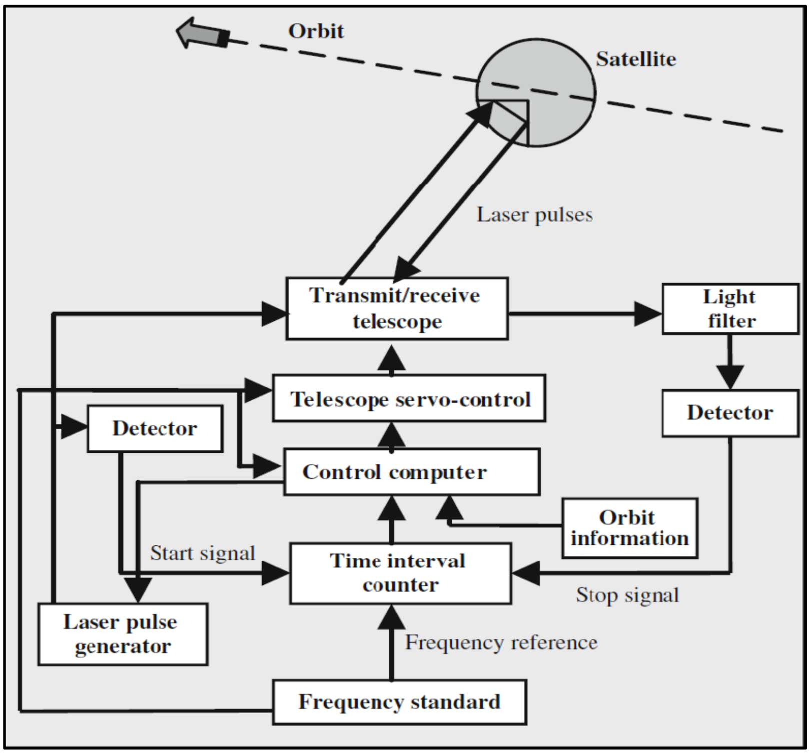

Figure 9. An illustration of the working principle and basic components of an SLR system. Source: Combrinck, 2010.

A geodetic satellite like LAGEOS-1 (see Figure 8), has been orbiting for more than 40 years and has a very long lifespan making it an ideal and stable long-term scientific reference tool.

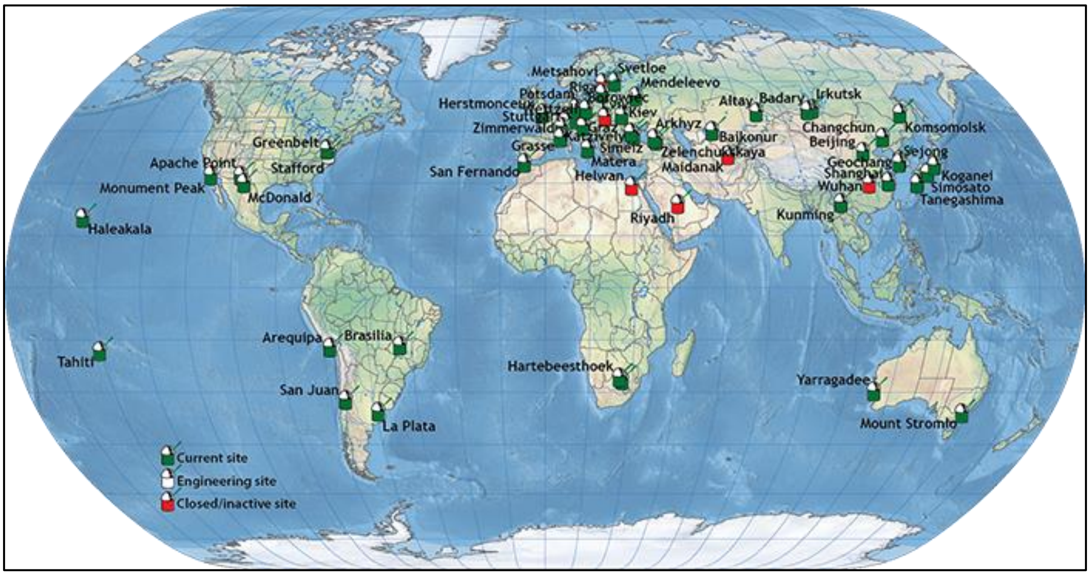

Figure 10. Satellite Laser Ranging (SLR) station network. The only active station on the African continent at Hartebeesthoek, South Africa. HartRAO has two ranging stations Mobile Laser System, MOBLAS-6 (USA) and Sazhen – TM (Russia). The geometry of the SLR network is skewed in favour of the Northern Hemisphere accounting for 82% of the total. Source: NASA, 2018.

A summary of current ILRS stations is listed in Table 1 with those located in the Southern Hemisphere highlighted.

Table 1. Worldwide active ILRS stations as at July 2018. Although La Plata in Argentina is mentioned elsewhere, it is omitted from this table since it is not generating data at the moment. Source: ILRS, 2018.

Monument	Code	Location Name, Country	Date of Latest Site Log	Hemisphere
1. **1824**	GLSL	Golosiiv, Ukraine	2018/06/08	N
2. **1868**	KOML	Komsomolsk-na-Amure, Russia	2014/01/27	N
3. **1873**	SIML	Simeiz, Ukraine	2017/03/22	N
4. **1874**	MDVS	Mendeleevo 2, Russia	2013/08/14	N
5. **1879**	ALTL	Altay, Russia	2009/03/25	N
6. **1884**	RIGL	Riga, Latvia	2017/07/27	N
7. **1886**	ARKL	Arkhyz, Russia	2012/02/15	N
8. **1887**	BAIL	Baikonur, Kazakhstan	2012/02/13	N
9. **1888**	SVEL	Svetloe, Russia	2012/01/31	N
10. **1889**	ZELL	Zelenchukskya, Russia	2012/01/31	N
11. **1890**	BADL	Badary, Russia	2012/01/31	N
12. **1891**	IRKL	Irkutsk, Russia	2014/09/02	N
13. **1893**	KTZL	Katzively, Ukraine	2011/08/02	N
14. **7045**	APOL	Apache Point, NM	2009/06/29	N
15. **7080**	MDOL	McDonald Observatory, Texas	2017/03/09	N
16. **7090**	YARL	Yarragadee, Australia	2018/12/13	S
17. **7105**	GODL	Greenbelt, Maryland	2018/03/20	N
18. **7110**	MONL	Monument Peak, California	2017/06/07	N
19. **7119**	HA4T	Haleakala, Hawaii	2018/05/04	N
20. **7124**	THTL	Tahiti, French Polynesia	2012/10/31	S
21. **7237**	CHAL	Changchun, China	2018/04/10	N
22. **7249**	BEIL	Beijing, China	2012/01/03	N
23. **7308**	KOGC	Koganei, Japan(CRL)	2002/10/21	N
24. **7358**	GMSL	Tanegashima, Japan	2017/05/09	N
25. **7394**	SEJL	Sejong City, Republic of Korea	2018/09/06	N
26. **7395**	GEOL	Geochang, Republic of Korea	2018/09/25	N
27. **7403**	AREL	Arequipa, Peru	2018/01/19	S
28. **7406**	SJUL	San Juan, Argentina	2006/04/04	S
29. **7407**	BRAL	Brasilia, Brazil	2014/08/26	S
30. **7501**	HARL	Hartebeesthoek, South Africa	2018/12/05	S
31. **7503**	HRTL	Hartebeesthoek, South Africa	2018/09/04	S
32. **7810**	ZIML	Zimmerwald, Switzerland	2018/03/05	N
33. **7811**	BORL	Borowiec, Poland	2018/06/15	N
34. **7819**	KUN2	Kunming, China	2018/02/08	N
35. **7821**	SHA2	Shanghai, China	2015/11/14	N
36. **7824**	SFEL	San Fernando, Spain	2015/06/11	N
37. **7825**	STL3	Mt Stromlo, Australia	2018/07/20	S
38. **7827**	SOSW	Wettzell, Germany	2017/05/11	N
39. **7838**	SISL	Simosato, Japan	2018/03/27	N
40. **7839**	GRZL	Graz, Austria	2018/06/26	N

Monument	Code	Location Name, Country	Date of Latest Site Log	Hemisphere
41. **7840**	HERL	Herstmonceux, United Kingdom	2018/02/05	N
42. **7841**	POT3	Potsdam, Germany	2018/11/14	N
43. **7845**	GRSM	Grasse, France (LLR)	2018/03/06	N
44. **7941**	MATM	Matera, Italy (MLRO)	2014/09/02	N
45. **8834**	WETL	Wettzell, Germany (WLRS)	2018/07/27	N

2.2.3 Chronology of Satellite Laser Ranging

The SLR technique was at infancy stages in the 1960's and 1970's and some challenges were experienced during ranging experiments. It was a technique conceived and developed from basic principles of optical and atmospheric characteristics as well as lessons learnt from the existing space radiowave-based techniques. Some of the main challenges included the telescope pointing and steering hardware, laser quality, ranging software, range analysis and availability of more accurate parameters regarding the gravitational influence exerted by the solar system. For instance, even after nearly 50 years in operation, it was noted in the ILRS 2007-2008 report that some ranging errors were attributed to the use of a particular time-of-flight counter which generated small but significant range errors. Most of the problematic areas have now been addressed as the SLR community has adopted a continuous improvement approach to development. For example, a higher accuracy of sub-centimetres is achieved when using normal point techniques (ILRS, 2018).

The first successful laser ranging experiment was made to an artificial satellite (Explorer 22/Beacon Explorer-B). This satellite was constructed at the National Aeronautics and Space Administration (NASA) Goddard Space Flight Centre (GSFC) and was equipped with retroreflector arrays. The launch of the spacecraft was on 9th October 1964 with an inclination of 79.7°, an apogee of 1,100 km and a perigee of 939 km. Beacon Explorer-B was magnetically stabilized and equipped with fused quartz optical retroreflectors (Degnan, 1985). A telescope mounted with a ruby laser was used and had an expected range accuracy of approximately 3 m. Significant improvements have been made since 1964 and the current SLR accuracy is at the level of 1 – 2 cm (Combrinck 2010).

However, the Explorer 22/Beacon Explorer-B satellite was insufficient due to the limited coverage that it provided, and this ignited a push for more geodetic satellites. By 1967 there were six satellites equipped with retroreflector arrays of which four were NASA's Explorer series (22, 27, 29 and 36) and the other two were the French Diadem 1C and 1D satellites (Johnson et al. 1967). The ranging experiments provided satellite position errors with a better precision than those obtained with the Baker-Nunn optical observations that were undertaken simultaneously. Prior to SLR, Astronomical Cassegrain Telescopes (see Figure 11) and later Baker-Nunn satellite tracking cameras (see Figure 13) were used for astronomical observations. A copy of the first photo taken of ‘Sputnik’, the Soviet Satellite Rocket with a Baker-Nunn satellite tracking camera is presented in Figure 12.

According to Degnan (2006), the microwave radar technology prevailing in the 1960’s provided an accuracy of at least 50 m whereas the initial laser ranging results provided 2 to 3 m accuracy.

The success of ranging measurements motivated the formulation of long-term plans for the application of space geodetic techniques including SLR to enhance in-depth study of the solid Earth dynamics. This led to the resolution to achieve 1 cm level accuracy for laser ranging (Kaula, 1982). An execution of a collocation experiment between NASA’s MOBLAS-1 and a Smithsonian Astrophysical Observatory (SAO) system at Mt. Hopkins Observatory Arizona from October 1969 to January 1970 yielded range biases of 1 to 2 m (Degnan, 2006). Subsequently, after assimilation of data from both SLR and Baker-Nunn experiments the adoption of a unified global geodetic datum with ± 5 m accuracy came into effect by 1973.

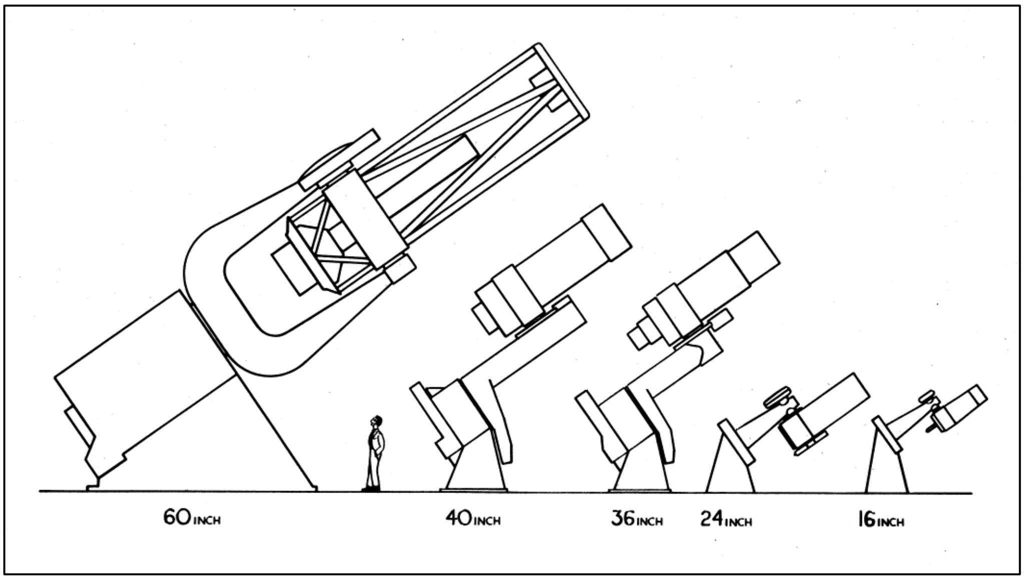

Figure 11. An illustration of the early Astronomical telescopes used in the 1950’s. These led to the development of Baker-Nunn satellite tracking cameras named in honour of the optical designer, Dr. James Baker, and the mechanical designer, Joseph Nunn. Source: Boller and Chivens, 2020.

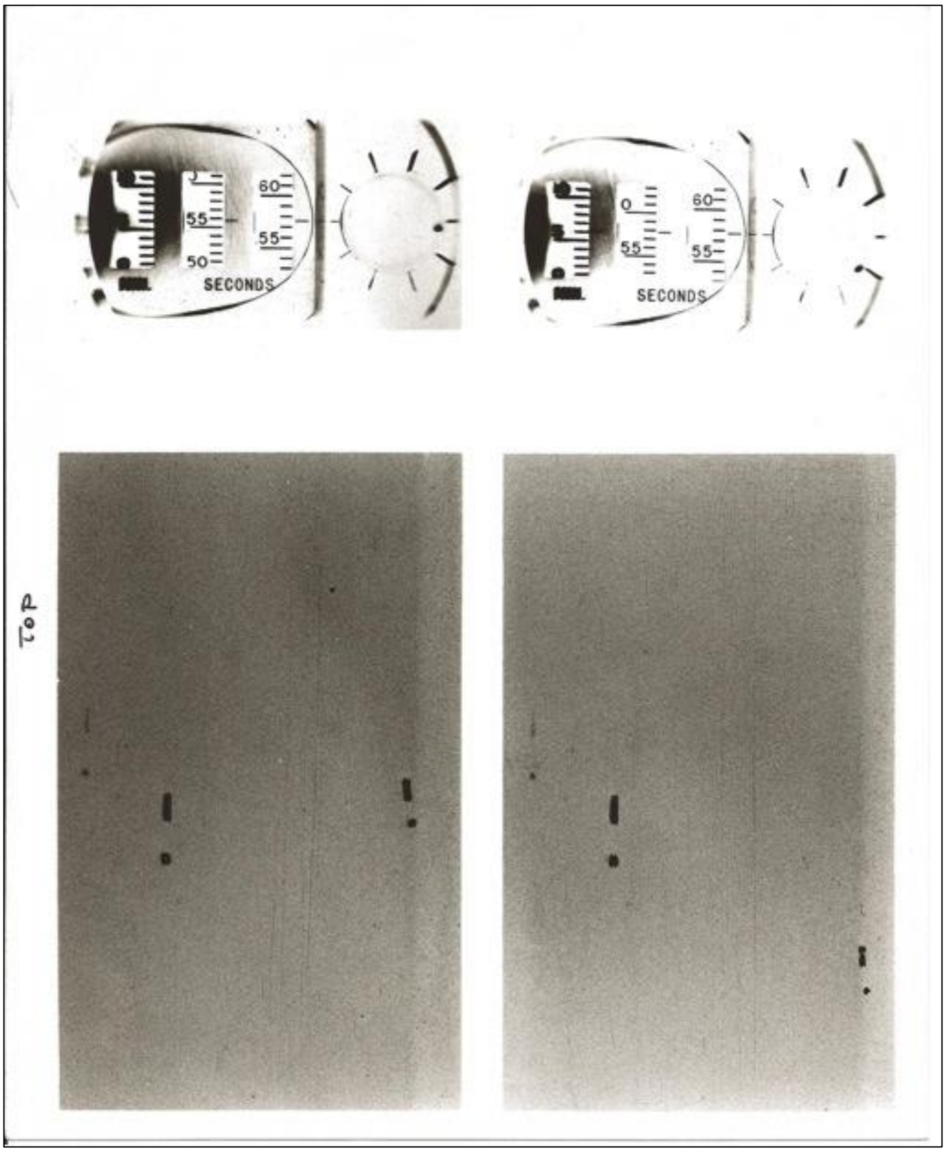

Figure 12. The first photos taken of "Sputnik", the Soviet Satellite Rocket, with the first of twelve Baker Nunn STRAC satellite tracking cameras as it passed over Boller and Chivens' assembly building on October 17, 1957. Source: Boller and Chivens, 2020.

In order to improve the global satellite network, the French launched another satellite (Starlette) in 1975 dedicated solely to laser ranging for the improvement of the gravity field and station position estimates. In the same year, the Americans also launched another satellite (GEOS-3) as the first operational radar altimeter satellite equipped with retroreflectors (McGuinigal et al. 1975). Later in 1976 NASA launched (LAGEOS-1), the first satellite dedicated exclusively to high precision laser ranging. Sixteen years later in 1992, LAGEOS-2 was launched by the Italians in collaboration with Americans based on the LAGEOS-1 design (ILRS, 2018). With the increased number of satellites having ranging capability, the

SLR technique provided a stable, high altitude, low drag inertial platform that was well suited for more precise gravity field and geodetic studies (Combrinck 2010).

Figure 13. This is an image of the first deliverable Baker-Nunn camera. In the foreground, Karl Heinz, the principle investigator for Smithsonian’s Satellite Tracking program and Audrey Stinett is in front of the Norman Time Standard clock. Source: Boller and Chivens, 2020.

One of the highlighted limitations to ranging was the quality of lasers available at that time. The first-generation ruby lasers with Q-switching had pulse lengths of 10 to 40 ns, which resulted in 1 to 6 m range accuracy. These have been replaced by lasers with shorter pulse lengths with picosecond resolution. The term Q-switching, Q-spoiling or giant pulse formation refers to a technique where a laser produces a pulsed output beam (Früngel 1965). A more efficient approach was later developed by enabling production of light pulses with an extremely high peak power of up to gigawatts, compared to the same laser operated in a continuous wave output mode.

The second-generation lasers had 2 to 5 ns pulse lengths corresponding to a 30 to 100 cm range accuracy. Currently, most of the SLR tracking sites use the third-generation, mode-locked Neodymium-doped Yttrium Aluminium Garnet (Nd:YAG) lasers that have pulse lengths of 0.1 to 0.2 ns (or 100 to 200 picoseconds) with a 1 to 3 cm accuracy. Third generation lasers have single photon detection capability. It is envisioned to develop laser systems with capability of 1 to 3 mm range accuracy, low eye-safe energy and capability of high-grade autonomous tracking (Degnan, 2006).

A brief history and milestones of SLR are listed in Table 2. Thereafter, the range bias derived by in using the SLR technique from observations at French SLR stations are summarised in by Combrinck (2010).

Table 2. A brief history and milestones of satellite laser ranging. The Neodymium-doped Yttrium Aluminium Garnet (Nd-YAG) lasers have replaced ruby laser systems in SLR systems (Pugh, 2004). The error budget includes all the sources of error (and their associated errors) that contributes to the SLR technique. It also provided the sum of all these errors (sum of component parts).

Year	Laser Ranging Milestone	Error budget
1964	• First successful use of SLR technique by NASA to measure the orbit height of the Beacon Explorer-B satellite fitted with retroreflectors. The measurement of the station position was within 30 m.	30.0 m
1969	• Station positions with 20 m error margin achieved by using SLR. • NASA Apollo 11 places the first retroreflector array on the Moon.	20.0 m
1968 – 1976	• NASA, Centre Nationale d'Etudes Spatiale (CNES), and Smithsonian Astrophysical Observatory (SAO) focus on global geodetic and gravity field measurements using remote sensing satellites equipped with retroreflectors.	0.1 -1.0 m

Year	Laser Ranging Milestone	Error budget
1974	• Laser ranging achieved ranging to satellites by ± 0.1 m, • Lunar ranging to ± 1 m, and • Station positions ± 5 m.	
1975	• CNES (France) launched passive satellite (Starlette) on 06/02/1975 dedicated to SLR research.	0.1 - 0.2 m
	• A satellite (GEOSAT) was launched on 09/04/1975 for ocean altimetric missions.	
1976	• NASA launched LAGEOS-1 (04/05/1976) dedicated to SLR research.	
	• SEASAT (27/06/1976) launched for ocean altimetric missions.	
1979	• Ranging to satellite positions achieved less than 0.1 m error margin. • SLR used to define orbits to calibrate altimeter satellite positions to measure land and sea levels.	< 0.1 m
1984	• SLR provides data to enable measurement of plate tectonics.	
1989	• SLR achieved sub-centimetre errors while ranging to satellites. • Provided station positions at ± 1.0 - 2.0 m.	<0.01 m
1992	• Another geodetic satellite LAGEOS-2 was launched on 22/11/ 1992.	<0.01 m
1994	• SLR used to measure contemporary tectonic plate motion to mm/yr resolution. • Ocean topography and wave height measured at cm level with altimeter satellites, and showed 3 mm/yr rates in global mean sea level rise.	<0.01 m
1998	• SLR used to measure tidally induced motion of the geocentre of the Earth.	
2005	• Observations standard set to millimetre accuracy.	0.001 m

Table 3. Laser ranging error budget for French SLR stations. These values are still representative of most modern SLR stations (Exertier et al. 2000). It is important to distinguish precision and accuracy of a system. During ranging sessions, it is possible to attain high precision but with low accuracy for example, if the telescope is not well calibrated. The objective is to ensure that the SLR systems and both precise and accurate.

Origin	Precision (mm)	Accuracy (mm)
Laser	4.0 – 5.0	
• Pulse	1.0	
• Width	4.0 – 5.0	
Detector		
• Start	3.0 – 6.0	
• Stop	1.0 – 3.0	
Timer	2.0 – 3.0	
Clock	1.0 – 2.0	
Calibration	1.0	2.0 – 6.0
• Geometry		1.0 – 2.0
• Electronic		1.0 – 4.0
Depend (Azimuth, Elevation)	1.0 – 3.0	
Instrument	6.0 – 9.0	2.0 – 6.0
Atmosphere	3.0 – 5.0	5.0 – 8.0
• Pressure		1.0 – 2.0
• Temperature		1.0
• Humidity		4.0 – 5.0
Target signature		
• LAGEOS	1.0 – 3.0	1.0 – 3.0
Single shot	7.0 – 12.0	
Normal point	1.0 – 3.0	8.0 – 18.0

In the next section, some key areas of space geodetic research where SLR plays a crucial role are illustrated.

2.2.4 Advantages of SLR

Some advantages of the SLR geodetic technique and its applications are:

a) Enables the study of the solid Earth and its surface, contributes to Lunar science, and can be used to test relativity,
b) SLR is utilised in the study of temporal variations in the geopotential.
c) Contributes to the maintenance of Earth scale and the determination of the centre of figure of the Earth and a global geodetic reference frame,
d) Enhances the determination of Earth Love numbers and their frequency dependence, the refinement of low and intermediate harmonics of the static geopotential, the determination of the Earth's total mass and vertical processes,
e) Contributes towards the study of the Earth's gravitational field which provides global constraints on the mass movements and exchanges occurring within the Earth's hydrosphere-atmosphere systems,
f) Used in determining the resolution of the long wavelength non-tidal component of the temporal variations of the geopotential,
g) Contributes to the estimation of the elastic response of the solid Earth at tidal frequencies,
h) Used in defining the frame origin - Earth CoM,
i) Enables realization of the orientation of the Earth's spin axis as well as periodic and secular variations in its spin rate – EOP,
j) Provides basic reference frame and gravity information and
k) Supports oceanographic and ice missions through precise determination of the satellite orbit in a geocentric reference frame and periodic calibration of on-board microwave altimeters.

In concert with the VLBI technique, SLR verified the tectonic plate movements to a few mm per year (Smith et al. 1990).

Reference points

In order to any space geodetic technique to provide useful data, there is need for a stable reference point. A SRP may refer to a physical monument like a brass plate that is fixed on bed rock for long term stability. The actual geodetic coordinates are determined by survey and henceforth used as a reference point for the geodetic site. An Invariant Point, Telescope Invariant Point (IVP) or Telescope Reference Point (TRP) as indicated in Figure 14 is defined by Combrinck (2010) as being determined by the intersection of the telescope axes (if XY mount) or the axis offset and its right-angle projection from the elevation axis onto the azimuth axis (if an Az-El mount). This virtual point is determined by surveying the other reference points with known coordinates and the IVP derived geometrically. Other SRPs could be pins or brass plates (see Figure 15) anchored on concrete slabs, piers, bedrock or any stable base with known coordinates.

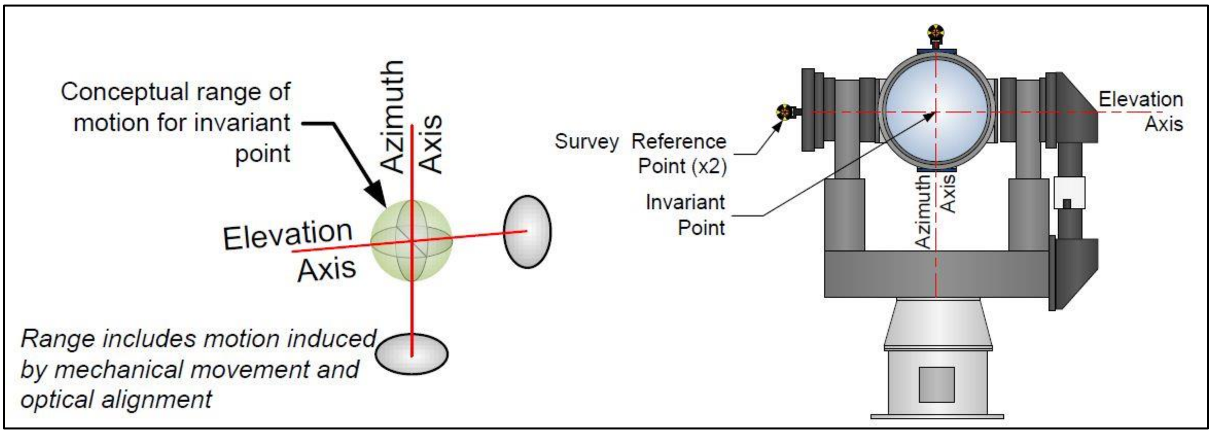

Figure 14. Depiction of a SLR telescope invariant point (IVP). Source: Donovan et al., 2016.

Figure 15. A stainless steel plate as a ground mark directly above the MOBLAS 6 telescope at HartRAO. The red arrow points to the SRP. Source: HartRAO, 2018.

In the next section a review of the range equation and atmospheric correction are examined.

2.3 A review of SLR observation equation and atmospheric correction

Laser ranging to artificial satellites or the Moon is affected by atmospheric conditions (e.g. refraction and turbulence), the CoM of both the Earth and the object of interest, the station's range and time bias, and relativistic factors which have been expounded by Combrinck, (2010).

Short arc range biases (which could be based on daily or weekly data sets for Low Earth Orbiting (LEO satellites) or longer durations (month) for High Earth Orbiting (HEO satellites) are difficult to compute due to the correlation between range bias and station position, especially the vertical component. According to Combrinck (2010) the other factors which contribute to the range bias include non-linearities in the interval counter (creating a non-linear bias) or errors in the barometric pressure, temperature and relative humidity sensors (these last three parameters affect atmospheric delay modelling). Further, Combrinck (2010) also noted that the determined station position also referred to as the ITRF point, an error in system delay, an error in the tie or eccentricity between the station coordinate reference point and the SLR telescope reference point could be added to the range error budget. Despite these attributes, the most critical factor affecting the SLR technique is the atmosphere which has the greatest error budget. The sensitivity of SLR products/data processing results to range biases has been illustrated by Coulot et al. (2006), for the Grasse SLR station (ILRS code 7835), as shown in Figure 16, where some modifications had been made to the system in 1997.

The “Up” component time series computed in Figure 16 was computed without any range bias. The time series reveals a sudden jump around September 1997, which corresponds to a modification of the detection system. Consequently, this modification introduced systematic errors in the solution emphasizing the need to address and promptly record and update any station biases or activities to the SLR system.

Improvements in atmospheric modelling regarding the SLR technique have been made as documented by Schutz et al. (1983) and Pearlman (1984) which was earlier developed by Marini and Murray (1973). The atmospheric correction model includes a correction of the atmospheric refraction based on the computed index of refraction at the tracking station (Marini and Murray, 1973). The Marini and Murray model requires the actual measurements of temperature, pressure and relative humidity from the ranging site. As given in Pearlman (1984), pressure at the tracking station is a dominant factor as expressed in Equation (1).

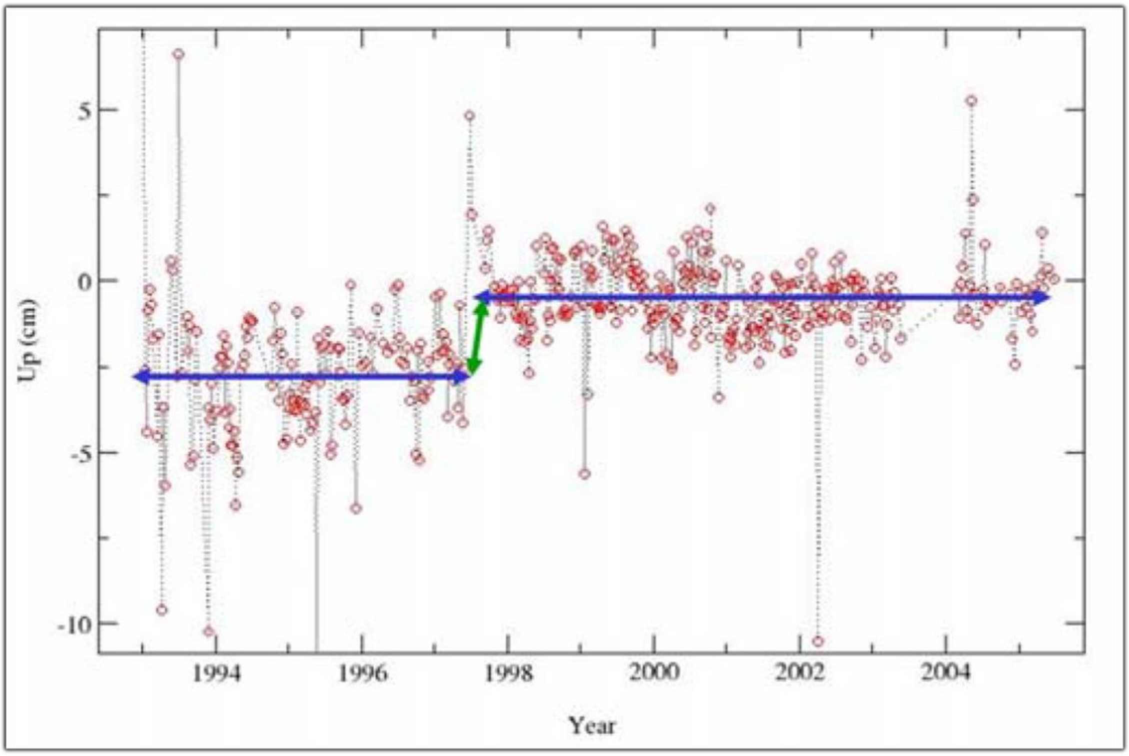

Figure 16. The Up component time series (in cm) of Grasse SLR station (7835) in ITRF2000, where no range bias has been estimated nor applied during computation. Modifications were made on the SLR system in September 1997 causing a sudden jump as indicated by the green arrow. Source: Coulot et al. (2006).

$$\partial \Delta R = \frac{0.0024}{\sin E} \partial P. \tag{1}$$

The change $\partial \Delta R$ in the range correction ΔR is in mm, and ∂P is the change in atmospheric pressure in mbar.

Other areas that have been improved upon include the laser generation system, hardware modules, software for pointing, steering and ranging, the mounting, electronics, timers, photon detection systems and other auxiliary components. Similarly, improvements in atmospheric modelling and more advanced orbital modelling with inclusion of other interactive forces such as those from the Moon, Sun and planets as well as the varying gravity field of Earth that perturbs satellite orbits and therefore range measurement modelling are now better understood. Both the observed and the computed SLR range to the satellites have therefore improved; this has made modelling and estimation of many parameters more accurate. Some system errors are caused by the components, which affect the efficiency, cause attenuation or deformation due to heat or electromagnetic interference that preclude achieving an error free solution. These attributes are however possible to model while deriving the range solution. Station related error sources must however be minimized to improve range solutions. Following this brief overview of the error sources that affect the SLR data processing results, the remainder of this section is dedicated to a review and discussion of the SLR observation equation.

Freeman (1962) developed a range error compensation model by assuming that the atmosphere is spherically symmetrical. In referring to the works of Thayer and Freeman who expressed atmospheric corrections in terms of error functions, Rowlandson and Moldt (1969) replaced the error functions with their asymptotic expressions hence providing closed form equations. In 1969, Hopfield (1969) made modifications to the expression by treating the dry and wet air components independently and represented each component as a fourth-degree function of height above the geoid by using a least squares fit to obtain the height parameters. Marini (1972) based his approach on the Freeman (1962) assumption of a spherically symmetrical atmosphere but used an exponential profile. Later Mendes et al. (2002) developed mapping functions (MF) to model the elevation angle dependence of atmospheric delay for SLR data analysis, which produced improved results at low elevation angles. The advantage of the MF developed by Mendes et al. (2002, FCULb) was that it does not depend on any meteorological data and is adapted from the model for global mapping functions for the atmospheric delay at radio wavelengths developed by the Niell (1996) approach.

Another technique in atmospheric correction modelling is by Abshire and Gardner (1985) by use of lasers with different wavelengths or two-colour lasers to measure the differential signal transit time. Lasers at two different frequencies are fired to the satellite and due to the atmospheric refractivity the dispersion in the optical path length differs. The difference is used to estimate the atmospheric correction.

In 2007 Hulley and Pavlis (2007) applied another alternative using ray-tracing by including the effects of horizontal refractivity gradients. Ray tracing is used to obtain constant radiosonde measurements of altitude, pressure, temperature, relative humidity and other meteorological parameters as the balloon ascends after being launched.

In this study an overview of the Marini-Murray model is given. The focus however is on the Mendes et al. (2002) model as modified in Combrinck and Suberlak (2007). A summary of the efforts towards atmospheric correction are illustrated in Figure 17 followed by a brief overview of the relevant expressions.

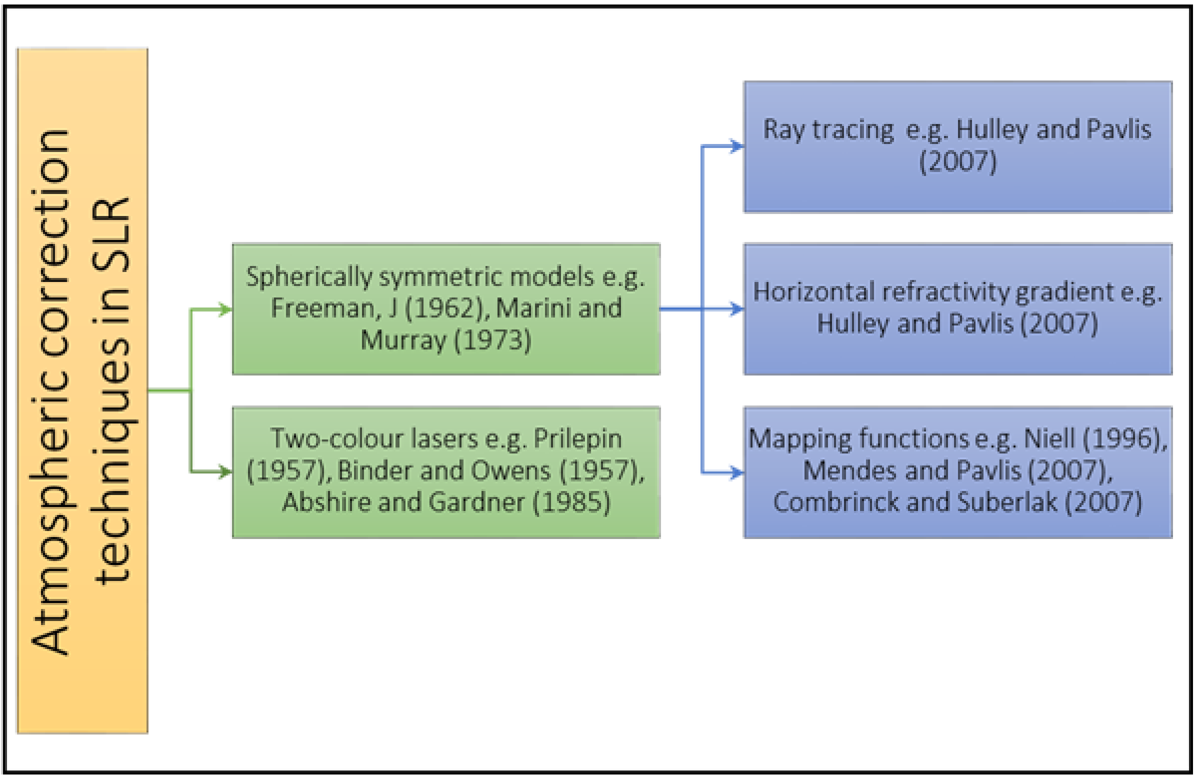

Figure 17. Atmospheric correction techniques in SLR.

The atmospheric correction formula adopted during the 13th General Assembly of the International Association of Geodesy (IAG) is expressed in Equation (2) which forms the basis of later developments.

$$N = \left(287.604 + \frac{1.6288}{\lambda^2} + \frac{0.0136}{\lambda^4}\right)\left(\frac{P}{1013.25}\right)\left(\frac{1}{1+0.003661t}\right) - 0.055\left(\frac{760}{1013.25}\right)\left(\frac{e}{1+0.00366t}\right) \tag{2}$$

where

$N \equiv 10^6\left(n-1\right)$,

$\lambda \equiv$ wavelength of radiation in microns,

$P \equiv$ atmospheric pressure in millibar (mbar),

$e \equiv$ partial water vapour pressure in mbar, and

$t \equiv$ temperature in degrees Celsius.

Saastamoinen (1972b) noted that a barometer measures the weight of the overlying atmosphere. By the law of Gladstone and Dale, the height integral $\int (n-1)\,dr$ of the atmospheric refractivity for light taken from ground level up to the top of the atmosphere is directly proportional to the ground pressure. The atmospheric correction for astronomical refraction at zenith distances not exceeding 75 degrees is expressed in Equation (3):

$$\Delta z_0'' = 16''.271 \tan z \left[1 + 0.0000394 \tan^2 z \left(\frac{p - 0.156e}{T}\right)\right]\left(\frac{p - 0.156e}{T}\right) - 0''.0749\left(\tan^3 z + \tan z\right)\left(\frac{p}{1000}\right) \tag{3}$$

where z is the apparent zenith distance in inches, p is the total pressure in millibar (mbar) and e is the partial pressure (mbar) of water vapour, and T is the absolute temperature in degrees Kelvin (K). A schematic illustration of astronomical refraction in a spherically layered atmosphere can be seen in Figure 18.

Marini and Murray (1973) made further improvements to correct laser range tracking data for atmospheric refraction at low elevations by specifically focussing on the works of Saastamoinen’s (1972b) where the range correction for troposphere and stratosphere to be subtracted from the observed microwave distance was given by Equation (4).

$$\Delta s = 0.002277z\left[p + \left(1255/T + 0.05\right)e - 1.16 \tan^2 z\right] \tag{4}$$

where Δs is in metres, constant 0.002277 in seconds, z is the zenith distance, p is the total barometric pressure in mbar and e is the partial pressure of water vapour in mbar, and T is the absolute temperature in degrees (K).

Although other corrections for atmospheric refraction had already been done by Freeman (1962), Rowlandson and Moldt (1969), Hopfield (1969), Marini (1972), and Saastamoinen (1972a), there was need for more accurate ranging solutions to meet the practical applications such as the development of a stable ITRF.

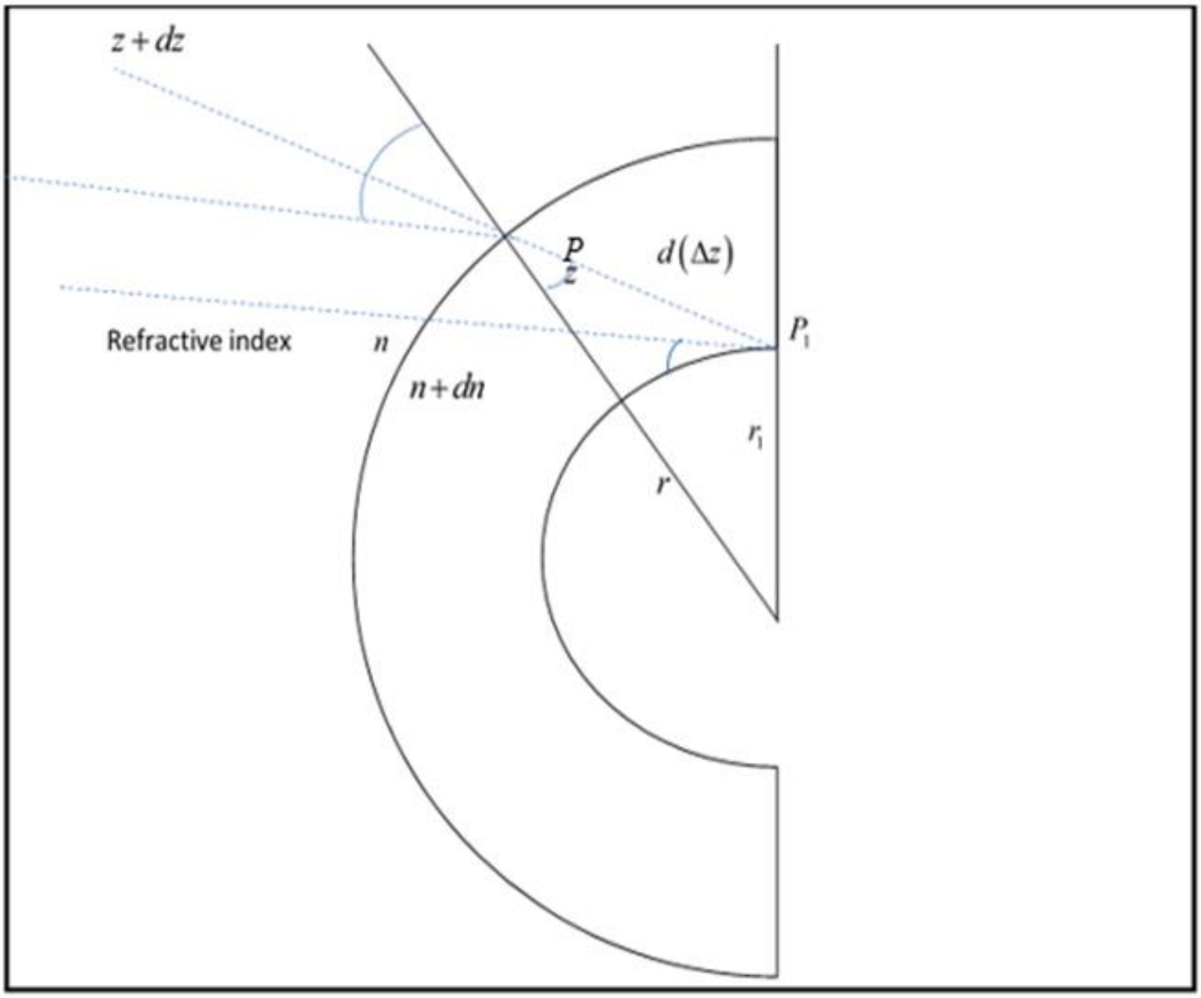

Figure 18. A schematic illustration of astronomical refraction $d(\Delta z)$ due to refraction at P in a spherically layered atmosphere. Source: Saastamoinen 1972b.

According to Marini and Murray (1973), the group refractivity of air which is dispersive at optical frequencies is expressed by Equation (5) as

$$N_g = \frac{d}{df}(fN) = N - \lambda \frac{dN}{d\lambda} \ . \tag{5}$$

where f is the frequency.

The group refractivity in Equation (5) can be expanded as:

$$N_g = 80.343 f(\lambda)\frac{P}{T} - 11.3\frac{e}{T} \ . \tag{6}$$

where P = total air pressure (mbar), e = partial pressure of water vapour (mbar), T = temperature (K) and

$$f(\lambda) \equiv 0.9650 + \frac{0.0164}{\lambda^2} + \frac{0.000228}{\lambda^4} \tag{7}$$

The prevailing assumption is that the atmosphere is symmetrical, and the refractivity is taken to be a function of height only. The geometry of a satellite tracking site configuration is illustrated in Figure 19 where h denotes the measured height from the tracking station upward, the subscript 0 implies that measurements are evaluated at the tracking site while subscript 1 denotes quantities evaluated at the satellite. The curved line indicates the ray path between the tracking site and the satellite. The true range R illustrated by the straight line denotes the distance between the tracking site and the satellite and the true elevation angle E is the angle between this straight line and the horizontal line at the site. The nominal Earth radius used for r_e is 6 378 km.

The height of the tracking site above sea level is denoted by H. It therefore means that the correction is the difference between the true value and the measured value of the range, which is given by:

$$\Delta R \equiv R_e - R \tag{8}$$

A further expansion of ΔR is given in Marini (1972). The final formula used by Marini and Murray (1973) is expressed as Equation (9) with integrals being functions of pressure, temperature and relative humidity of the surface air at the tracking site (which is like the Saastamoinen, 1972b approach). Therefore

$$\Delta R = \left[10^{-6}\int N_g dh\right].\frac{1}{\sin E} - \left[\frac{10^{-6}}{r_0}\int hN_g dh + 10^{-12}\int\left(NN_g - \frac{1}{2}N^2\right)dh\right]\frac{1}{\sin^3 E} + \ldots \tag{9}$$

Further evaluation of integrals yields the Equations (10), (11) and (12).

$$10^{-6}\int N_g dh = \frac{f(\lambda)}{f(\varphi, H)}\left[0.002357P_0 + 0.000141e_0\right] \tag{10}$$

The latitude of the tracking station is denoted by φ degrees above the equator.

$$\frac{10^{-6}}{r_0}\int hN_g dh = f(\lambda)(1.084\times10^{-8})P_0T_0K \tag{11}$$

$$10^{-12}\int\left(NN_g - \frac{1}{2}N^2\right)dh = f(\lambda)(4.734\times10^{-8})\frac{P_0^2}{T_0}.\frac{2}{3-1/K} \tag{12}$$

where

$$f(\varphi, H) = 1 - 0.0026\cos 2\varphi - 0.00031H$$

and

$$K = 1.163 - 0.00968\cos 2\varphi - 0.00104T_0 + 0.00001435P_0$$

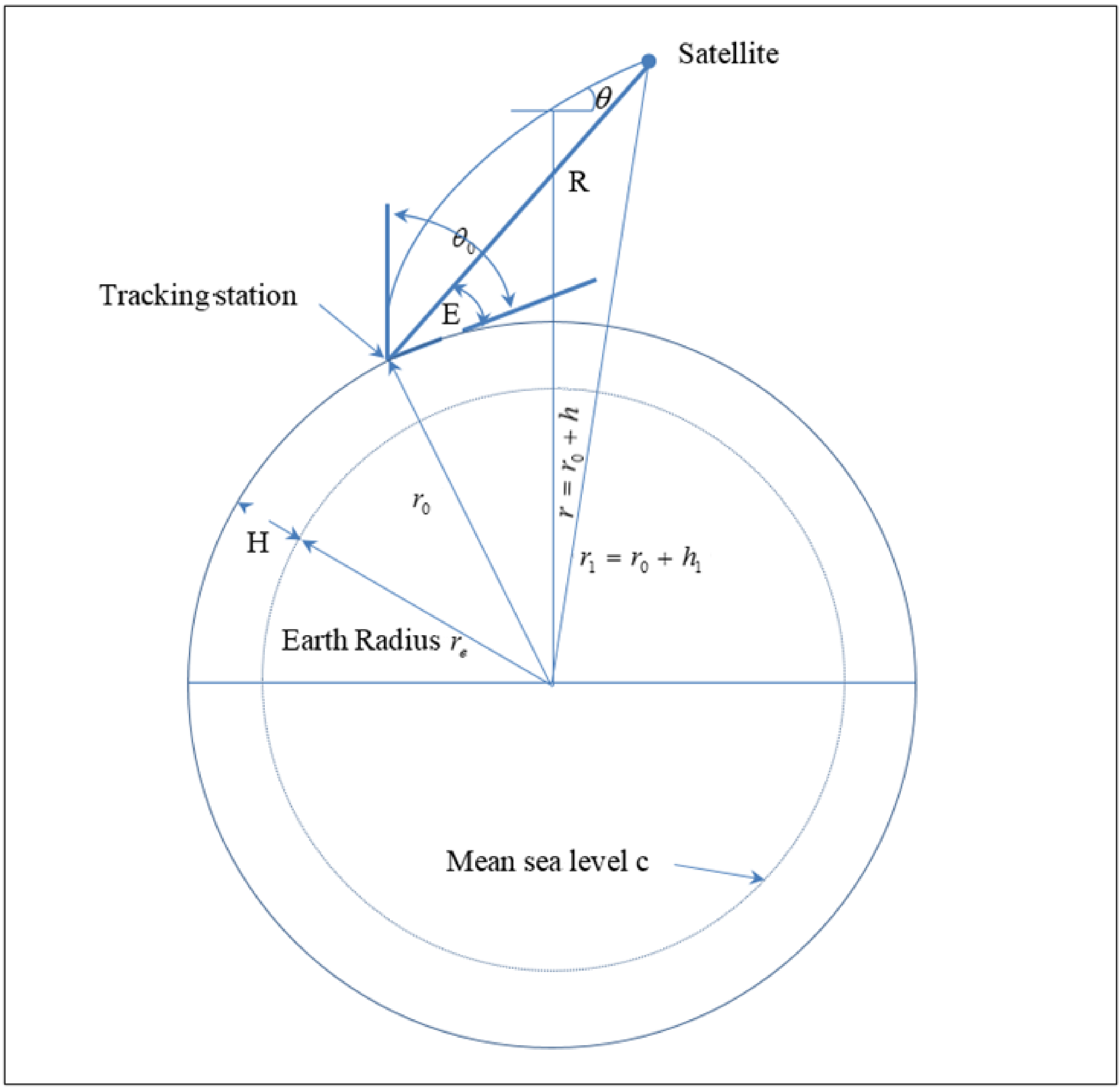

Figure 19. The geometry of a satellite tracking station. Adapted from Marini and Murray,1973.

Regarding Equation (9) used for determining the range error ΔR, Marini and Murray (1973) observed that correction of the laser range tracking data for atmospheric refraction at elevations above 10° can be obtained by using a continued fraction form expressed as Equation (15).

$$\Delta R = \frac{f(\lambda)}{f(\varphi, H)} \cdot \frac{A+B}{\sin E + \dfrac{B/(A+B)}{\sin E + 0.01}} \quad \textbf{(13)}$$

where ΔR = range correction (m), E = true elevation of the satellite, P_0 = atmospheric pressure at the laser ranging station (mbar), T_0 = atmospheric temperature as the laser ranging station (K), e_0 = water vapour pressure at the laser ranging station (mbar), $f(\lambda)$ = 1 for ruby laser (as defined in Equation (7)), $f(\varphi, H)$ = 1 for a laser ranging site at 45° latitude and at sea level.

The results based on the Marini and Murray (1973) model were compared with the ray-tracing technique and the maximum mean error of the algorithm at 10° was 0.16 cm and at 80° the error was 0.07 cm. Ray tracing correction included measurements of pressure, temperature and relative humidity being taken at various altitudes as the balloon was ascending, and these values used to construct spherically symmetric refractivity profiles above the balloon's launch point. On comparing the results derived from both the spherically symmetric atmospheric correction and ray-trace correction approach for spherically symmetric refractivity it was determined that the two techniques achieved similar results even at low elevation angles. The standard deviation of the difference between the methodologies can be attributed to both the modelling errors in the formula and errors in the measured values of pressure, temperature and relative humidity. The Marini and Murray (1973) model is a good benchmark for atmospheric correction for laser ranging data as results have confirmed that spherically symmetric (SC) is a nearly unbiased estimator of the spherically symmetric ray-trace correction RT.

Abshire and Gardner (1985) also noted that the two main spherical models which provide accuracies of few centimetres at 20° were developed by Saastamoinen (1972c) and Marini and Murray (1973) but that these hold true only in the troposphere, and that horizontal refractivity gradients could introduce centimetre level errors into the spherical-correction models at low elevation angles.

To further improve the ranging accuracies, a gradient correction model based on surface meteorological measurements was developed by Gardner (1977).

Briefly, the general form of the atmospheric correction models can be expressed as:

$$AC = SC + GC \tag{14}$$

where the term AC denotes the atmospheric correction model, SC models for the spherically symmetric atmosphere and GC models the horizontal refractivity gradients. This can further be expressed by Equation (15) as

$$GC = \frac{C}{\sin E \tan E} n \cdot \nabla \left(P_s T_s K_s \right) + \frac{D\left(1 + 1/2 \cos^4 E\right)}{\sin^3 E \tan E} n \cdot \nabla \left[\frac{P_s T_s^2 K_s^2}{2 - K_s} \right] \tag{15}$$

where

$$f\left(\theta, H\right) = 1 + 0.0026 \cos 2\theta - 0.0031H \tag{16}$$

$$K_s = 1.163 + 0.00968 \cos 2\theta - 0.00104 T_s + 0.00001435 P_s \tag{17}$$

$$A = 0.002347 P_s + 0.00141 e_s \tag{18}$$

$$B = \left(1.084 \times 10^{-8}\right) P_s T_s K_s + \left(4.735 \times 10^{-8}\right) \cdot \left(P_s^2 / T_s\right) 2\left(3 - 1/K_s\right) \tag{19}$$

$$C = 80.343 f\left(\lambda\right) \frac{R^2}{\left(Mg\right)^2} 10^{-6} = 6.915 \times 10^{-2} f\left(\lambda\right) \tag{20}$$

$$D = -80.343 f\left(\lambda\right) \frac{2}{r_0} \frac{R^3}{\left(Mg\right)^2} 10^{-6} = -6.362 \times 10^{-7} f\left(\lambda\right) \tag{21}$$

and

e_s is the water vapour pressure at ranging the station (mbar),

P_s is the surface pressure at the ranging site (mbar),

T_s is the surface temperature at the ranging site (K),

θ is the colatitude of ranging site,

H is the altitude of ranging site above sea level (km),

M = 28.966 (the molecular weight of dry air),

R = 8314.36 $J\left(K\right)^{-1}$ (kg-mole)$^{-1}$ (the universal gas constant),

g = 9.784 m/s^2 (the acceleration of gravity),

r_0 = 6378 km (the nominal radius of the Earth),

$n = \sin\alpha x + \cos\alpha y$ where x and y are the East and North unit vectors, α is the satellite azimuth angle $(\alpha = 0 = \text{North})$ and E is the satellite geometric (unrefracted) elevation angle (see Figure 19).

The SC and GC values are in metres if the values of A, B, C and D are expressed as m^{-1}.

The challenge facing the GC approach lies in obtaining measurements of horizontal pressure and temperature gradients at the ranging site due to terrain features such as mountains, large water bodies, and vegetative cover believed to have greater influence on meteorological conditions near the ground – consequently causing a distortion in temperature and pressure values near the laser site. These biases cause both amplitude and phase errors in applications of the GC model (Abshire and Gardner, 1985). Although this methodology has an added advantage of improving the SC model, Gibbs and Majer, (1981), together with Dunn et al. (1984) reveal that relatively large temperature variations over short spatial scales of approximately 10 km may cause distortions in the calculated values of the GC model. An outline of the methodology is given in Chapter 3.

The range is calculated by determining the number of photons that return to the receiving telescope which can be estimated by the radar range equation (Combrinck 2010). The mean number of photoelectrons detected by the SLR sensor N_{pe} is expressed in Equation (22).

$$N_{pe} = \eta_q \left(E_T \frac{\lambda}{hc} \right) \eta_t G_t \sigma_{sat} \left(\frac{1}{4\pi R^2} \right)^2 A_R \eta_r T_a^2 T_c^2 \theta \qquad \textbf{(22)}$$

where

η_q is the detector quantum efficiency (the fraction of the total radiation incident that is actually detected),

E_T is the pulse power (average power divided by pulse repetition rate),

λ is the wavelength of the laser,

h is Planck's constant,

c is the speed of light in a vacuum,

η_t is the efficiency of the transmitter optics,

G_t is the transmitter gain, with σ_{sat} is the satellite optical cross-section and R is the slant range to the satellite.

The other parameters are:

A_R as the effective area of the SLR telescope receiving aperture,

η_r is the efficiency of the receive optics,

T_a is the one-way atmospheric transmission and if cirrus cloud (thin, wispy cloud, occurring at altitudes > 6 km, composed of ice crystals is present, and

T_c is the one-way transmissivity of cirrus cloud.

The ranging expression as described by Combrinck (2010) is illustrated as Equation (23):

$$NPR_i = \left(\frac{NP_{tof_i}}{1x10^{12}} \times c \right) \Big/ 2 - \Delta a_i + \Delta CoM_i - \Delta R_{bi} - \Delta GR_i - \Delta \varepsilon_i \qquad \textbf{(23)}$$

where NPR_i is the normal point range (a normal point is the mean value of several single shots). In the case of LAGEOS a normal point consists of 66 data points or single shots). NP_{tof_i} is the normal point time-of-flight (in picoseconds). The velocity of light is symbolised by c in ms^{-1} while the atmospheric effects (e.g. refraction) are denoted by Δa_i. The centre-of-mass correction is $\Delta \mathrm{CoM}_i$ and the range bias (this is the propagation delay experienced by a laser signal), general relativity correction and a correction for unknown random errors are expressed as ΔRb_i, ΔGR_i and $\Delta \varepsilon_i$ respectively.

The atmospheric propagation delay is the most significant error source that affects the accuracy of SLR measurements as illustrated in Figure 20. The range increases at low elevation angles and improves as the satellite approaches the azimuth. Tracking a LEO satellite is a challenging task as it moves very fast overhead and the tracker has little time to point and receive successful photon returns. It get more daunting if the tracking procedure is in interleaving mode where multiple satellites are tracked simultaneously. Such practical limitations therefore require more refinement in the modelling to improve on the accuracy at lower elevations.

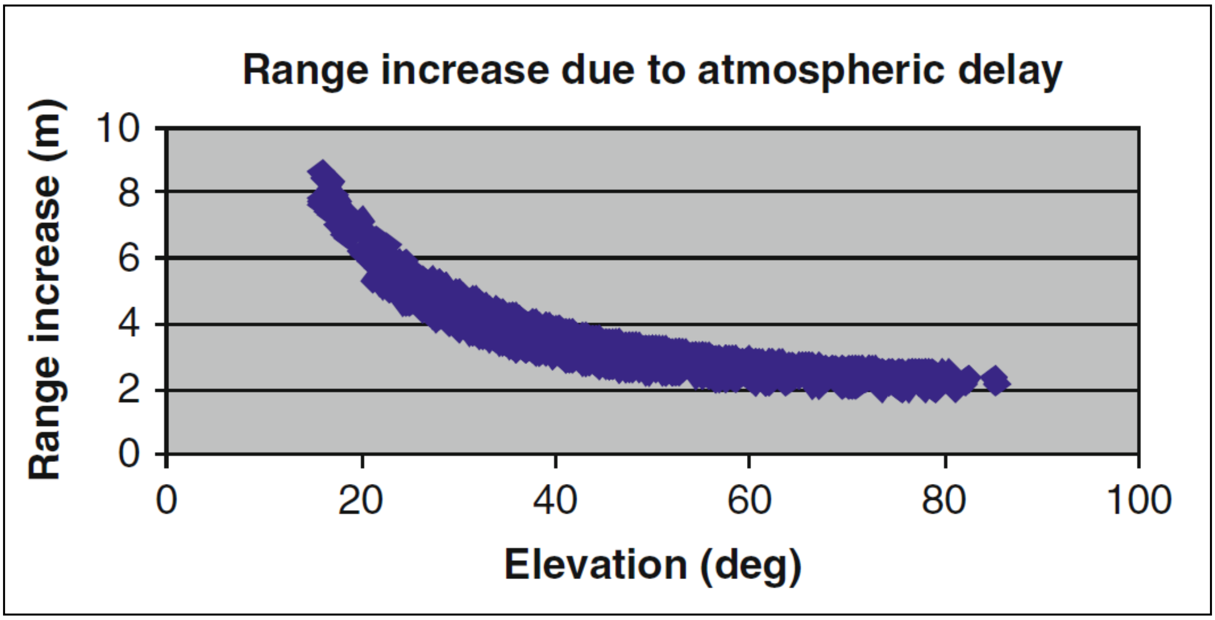

Figure 20. An illustration of the increase in range due to atmospheric delay (Combrinck, 2010).

Correction to the one-way range measurement is given by

$$\Delta R = \frac{f(\lambda)}{g(\phi,\mathrm{H})}\cdot\frac{\mathrm{A+B}}{\sin E + \dfrac{B/(A+B)}{\sin E + 0.01}} \tag{24}$$

with

$$A = 0.002357P + 0.000121e$$

$$B = \left(1.084\times10^{-8}\right)PTK + \frac{\left(4.734\times10^{-8}\right)2P^{2}}{T\left(3-1/K\right)}$$

$$K = 1.163 - 0.00968\cos 2\phi - 0.00104T + 0.00001435P$$

$$f(\lambda) = 0.965 + \frac{0.0164}{\lambda^{2}} + \frac{0.000228}{\lambda^{4}}$$

$$f(\lambda) = 1.02579\ for\,\lambda = 0.532\mu m\ \text{(Nd: YAG Laser)}$$

$$g(\phi,H) = 1 - 0.0026\cos 2\phi - 0.00031H$$

$$e = \frac{R_h}{100}\times 6.11\times10^{s}$$

$$s = \frac{7.5\left(T-23.15\right)}{273.3+\left(T-273.15\right)}$$

Variable ΔR is the correction in metres; E denotes the true elevation angle of satellite; P is the atmospheric pressure at the tracking station in (mbar); T represents the atmospheric temperature at tracking the station in (K); R_h signifies the relative humidity at the tracking station in (%); λ is the laser wavelength in microns $(\mu\mathrm{m})$; ϕ is the latitude of the tracking station; H indicates the height of the tracking station above mean sea level (km). Abshire and Gardner (1985), noted that a 1 mbar error in P introduces approximately 14 mm error in the range after applying the spherical model (SC). This is illustrated in Figure 21.

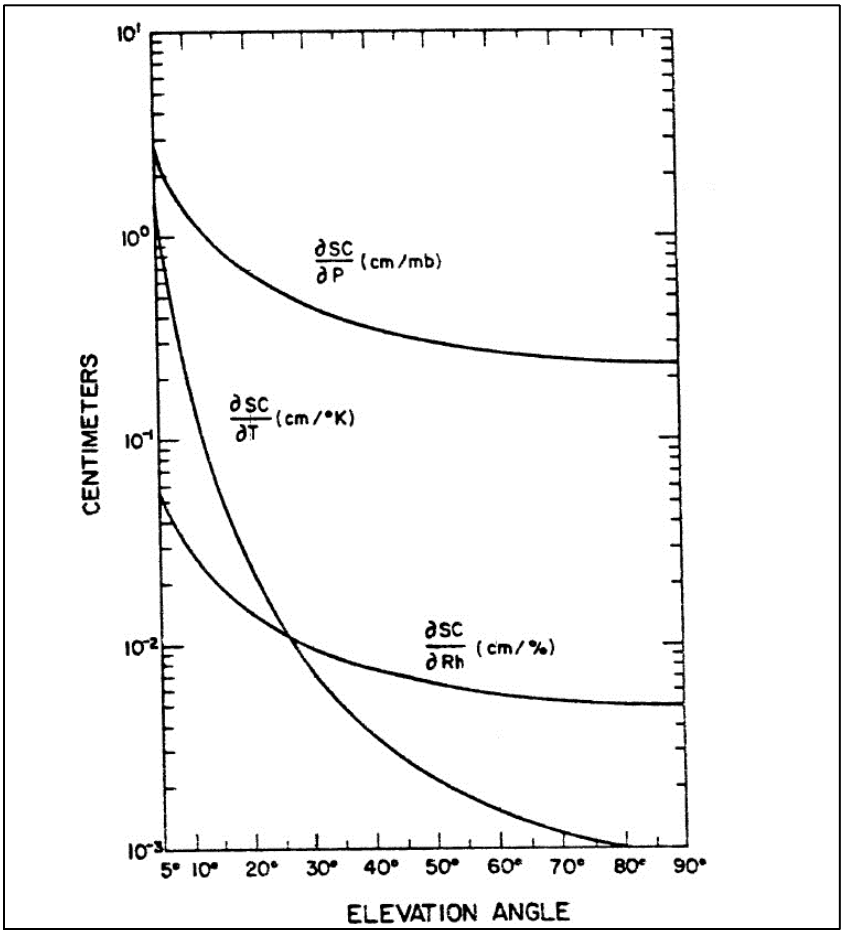

Figure 21. Variation of the spherical correction formula with respect to Pressure (P), Temperature (T) and Relative humidity (Rh). Source: Abshire and Gardner, 1985.

The relation regarding temperature measurement is given by Equation (25)

$$\partial \Delta R = \frac{1\times 10^{-5}}{\sin^3 E}\partial T \tag{25}$$

The change in temperature ∂T is expressed in Kelvin.

The atmospheric propagation delay d_{atm}^{z} experienced by a laser signal in the zenith direction is defined by

$$d_{atm}^{z} = 10^{-6}\int_{r_s}^{r_a} N dz = \int_{r_s}^{r_a} (n-1) dz \tag{26}$$

By splitting the zenith delay into both the hydrostatic and non-hydrostatic components then we obtain

$$d_{atm}^{z} = d_{h}^{z} + d_{nh}^{z} = 10^{-6}\int_{r_s}^{r_a} N_h dz + 10^{-6}\int_{r_s}^{r_a} N_{nh} dz + \tag{27}$$

where the hydrostatic component is (d_{h}^{z}) and non-hydrostatic is (d_{nh}^{z}), $N = (n-1)\times 10^{6}$ is the total group refractivity of moist air, n is the total refractive index of moist air, N_h is the hydrostatic component of refractivity and N_{nh} is the non-hydrostatic component of the refractivity, r_s is the geocentric radius of the laser station, r_a is the geocentric radius of the top of the (neutral) atmosphere, and dz has length units.

According to Ciddor (1996) the dry air component N_{gaxs} can be expressed as

$$N_{gaxs} = 10^{-2}\left[k_1 \frac{\left(k_0 + \sigma^2\right)}{\left(k_0 - \sigma^2\right)^2} + k_3 \frac{\left(k_2 + \sigma^2\right)}{\left(k_2 - \sigma^2\right)^2} \right] C_{CO_2} \tag{28}$$

where k_0 = 283.0185 μm^{-2}, k_1 = 5792105 μm^{-2}, k_2 = 57.362 μm^{-2}, k_3 = 167917 μm^{-2}, σ is the wave number and, $C_{CO_2} = 1 + 0.534\times 10^{-6}\left(x_c - 450\right)$.

Currently, both stations at HartRAO (HARL 7501 and HRTL 7503) use the Nd:YAG laser with wavelength λ = 532 nm. The group refractivity for the dry air component for Nd:YAG is computed as

$$N_{gaxs}^{532} = 10^{6} x \left(n_{gaxs}^{532} - 1\right) \approx 289.736 \tag{29}$$

Thus:

$$N_h = 289.736 f_h(\lambda)\left(\frac{T_d}{P_d}\right) Z_d \rho R_d \tag{30}$$

Or

$$N_h = K_1^L f_h(\lambda) Z_d \rho R_d \tag{31}$$

where K_1^L = 0.8239568 K Pa^{-1} while the modified group refractivity for dry air, $f_h(\lambda)$ is the dispersion equation the hydrostatic component expressed in Equation (29).

$$f_h(\lambda) = 10^{-2}\left[k_1^* \frac{\left(k_0+\sigma^2\right)}{\left(k_0-\sigma^2\right)^2} + k_3^* \frac{\left(k_2+\sigma^2\right)}{\left(k_2-\sigma^2\right)^2}\right] C_{CO_2} \tag{32}$$

with k_1^*= 19990.975 μm^{-2} and k_3^*= 579.55174 μm^{-2}

$$d_h^z = 10^{-6} K_1^L f_h(\lambda)\, \mathrm{Z}_d\, R_d \int_{r_s}^{r_a} \rho dz \tag{33}$$

By applying the hydrostatic equation

$$\int_{r_s}^{r_a} \rho dz = -\int_{P_s}^{0} \frac{dP}{g} = \frac{P_s}{g_m} \tag{34}$$

The surface barometric pressure P_s in Pascal, and g_m is the gravitational acceleration at the CoM of the vertical column of air in metres per second as observed in Saastamoinen, (1972b). Therefore, the final equation for the zenith hydrostatic delay in m is:

$$d_h^z = 0.00002416579 \frac{f_h(\lambda)}{f(\varphi, H)} P_s \tag{35}$$

While the expression for the zenith non-hydrostatic delay after replacing the known constants becomes:

$$d_{nh}^z = 10^{-6}(5.316 f_{nh}(\lambda) - 3.759 f_h(\lambda)) \frac{e_s}{f(\varphi, H)} \tag{36}$$

From Equation (45) we note that P_s the surface barometric pressure or station pressure is critical in determining the hydrostatic delay in satellite laser ranging and thus reinforces the need to ensure that station pressure is captured accurately.

In the next section we evaluate the effect of pressure changes to the O-C residuals.

Chapter 3 Methodology

3.1 Introduction

A survey was conducted to determine the height of the meteorological instruments at HartRAO using a South Total Station (NTS-350L). The immediate concern was to understand the correct interpretation of the height of an integrated meteorological instrument, in this case MET4 from Paroscientific, which has no visible marker. It was however difficult to determine the exact position of the pressure sensor in the instrument even after reference from user manual hence a mid-point was used. A technical drawing was retrieved later (see Figure 22) and the barometric port level is shown to be halfway. Ranging was then done to two of the existing reference piers (Pier_6 and Pier_12) fitted with retroreflectors (see Figure 23). The other targets were the GNSS receiver GNSS (HRAO), the MET4 unit next to the GNSS receiver (Met4_) and the MET4 unit next to the SLR (SLR Met4). The height offset between the pressure sensor and the SLR MOBLAS-6 SRP was then determined and thereafter the offset from the pre-determined coordinates of the IVP were used. The offset was compared to the site log sheet from the ILRS repository and found to be consistent.

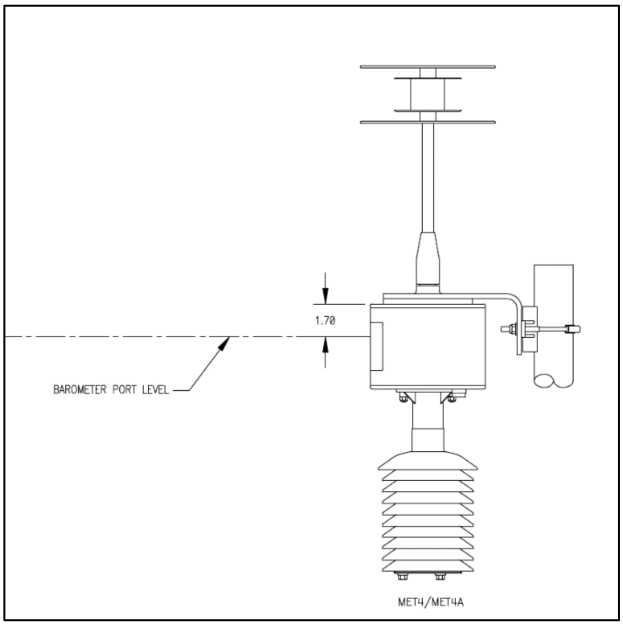

Figure 22. Image of a Met4 meteorological instrument. It is equipped with temperature, pressure and relative humidity sensors. Source: Paroscientific, 2020.

The coordinates of HartRAO’s SRP for the MOBLAS-6 SLR Station based on ITRF 2005 and WGS84 (epoch 2000.0) are contained in Table 4. The WGS84 is the World Geodetic System adopted in 1984. In order to determine HartRAO’s height above the geod, the WGS84, an Earth-centred, Earth-fixed terrestrial reference system and geodetic datum was applied. It comprises of a reference ellipsoid, a standard coordinate system, altitude data and a geod. GPS uses the WGS84 as its reference coordinate system.

The SRP for HartRAO is a brass plate mounted on bedrock underneath the MOBLAS-6 telescope. It is aligned to the IVP and has a pendulum blob pointing to the centre of the plate.

Table 4. The coordinates of the SLR SRP at HartRAO. Source: HartRAO, 2018.

X = 5085401.106 ± 0.001 m Y = 2668330.130 ± 0.001 m Z = 2768688.814 ± 0.001 m	X, Y, Z are Cartesian coordinates
dX = 0.0006 ± 0.0002 m/year dY = 0.0214 ± 0.0003 m/year dZ = 0.0154 ± 0.0002 m/year	dX, dY and dZ are annual drifts in the direction of the Cartesian axes
$\phi = -25.8897088^{\circ} = 25^{\circ}53'22''.951$ South $\lambda = +27.6861746^{\circ} = 27^{\circ}41'10''.228$ East H = 1406.786 ± 0.001 m	ϕ, λ and H are ellipsoidal coordinate system
dN = 0.0184 ± 0.0003 m/year dE = 0.0187 ± 0.0002 m/year dH = 0.0027 ± 0.0002 m/year	dN, dE and dH are drifts in the local target plane coordinates often called the local East, North and Up coordinates.
The WGS84 ellipsoid is 25.259 m above the EGM96 geoid at HartRAO.	

Figure 23. Aerial map of HartRAO depicting targets during the site survey. Source: Google Earth.

In Figure 24 the three visible meteorological instruments at HartRAO are highlighted in cyan circles where (a) is a standalone MET4 unit, (b) is a MET3 unit with the longest lifespan at HartRAO and (c) is a MET4 unit that is tied to the SLR system. A MET4 has pressure resolution of better than 1 μbar with a total accuracy of 0.08 mbar over the extended barometric range of 620 to 1100 mbar (Paroscientific, 2018).

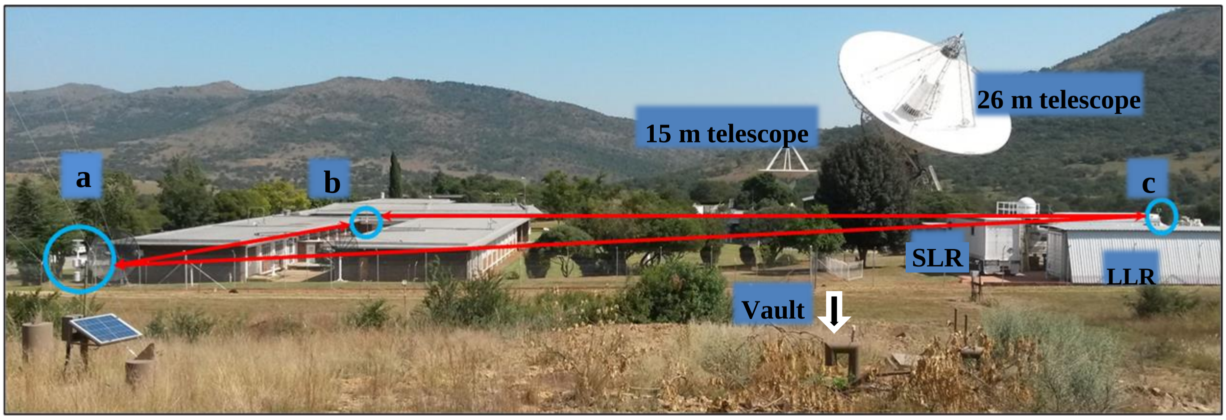

Figure 24. Meteorological instruments located at HartRAO. There are three Paroscientific meteorological instruments circled in cyan colour and depicted as (a) MET4, (b) MET3, and (c) MET4 (tied to the SLR).

The range bias analysis was done using 13 ILRS stations. The standard deviation of O-C residuals was extracted and tabulated as the baseline. Pressure values were then adjusted while keeping all other variables constant and the new O-C residuals were also extracted and tabulated. This process was repeated for all the pressure adjustments.

The dataset used in this analysis is within the ITRF definition and was chosen arbitrarily. This dataset has also been analysed by other interest groups and thus proved suitable for use and comparison. Plots of the standard deviation of the observed minus computed (O-C) values were generated with varying pressure adjustments.

A system performance plot obtained from the ILRS for active SLR sites is illustrated in Figure 25. It shows that Yarragadee, Australia has excellent throughput of data with 25 000 passes compared to the minimum of 3 500 passes. The number of passes for HartRAO is close to 5 000, which is equally good considering that only 17 out of the 39 stations between September 2017 and August 2018 achieved the threshold. To enable ease of use of the SLR data, each dataset adheres to strict guidelines as set out in Appendix A5. The periodic SLR global performance report card is contained in Appendix A6. The current SLR data format (see Appendix A7 CRD Format Overview) is referred to as the Consolidated Laser Ranging Data Format (CRD). The CRD format has replaced the Consolidated Prediction Format (CPF) data format that was used previously. Most SLR analytical programs have backward compatibility and therefore are able to read both data formats, or convert the CPF to CRD.

The metadata includes the site orthometric height, the description and position of the monument, the SRP, the SRP type, model and heights of the meteorological units as well as their heights from the SRPs. In addition, details regarding the SRP and the IVP (the intersection point of vertical and horizontal axes of the telescope lens) is provided. All these metadata parameters are function-called via the site eccentricity file during analysis. The error budget in the solution is dependent on the accuracy of these values.

Thirteen stations listed in Table 5 were selected for SLR analysis. SDAS software allows the selection of multiple stations and has multi-processing capability. All these stations have conducted SLR observations for several years and are deemed stable. Note that Mt. Stromlo in Australia has a redundant meteorological unit and hence appears twice in this list. It can be seen that the height difference to SRP is not uniform across the sites. Mt. Stromlo for example, has the maximum instrument offset of -2.3723 m. Four other stations have a zero offset. By manually adjusting pressure (as a function of height), we endeavour to determine if these offsets have a significant effect on the O-C residuals.

Table 5. Details regarding meteorological instruments in relation to the SRPs from SLR ranging sites. Source: ILRS, 2018.

Site Name	**Meteorological Sensor Model**	**Manufacturer**	**Recording Interval**	**Accuracy (mbar)**	**Height Diff to SRP (m)**	**Calibration interval**
1. Beijing, China	PUT-200	Vaisala, Finland	Per pass	0.50	-1.2000	Every 2 years
2. Greenbelt, Maryland USA	MET4	Paroscientific	Per pulse	0.08	-0.1500	Biyearly
3. Graz, Austria	DigiQuartz 740-16B	Paroscientific	Per calibration by linear fit for each return	0.10	0.0000	Yearly
4. Hartebeesthoek, South Africa	MET4	Paroscientific	Per pulse	0.08	-0.1500	Biyearly
5. Herstmonceux, United Kingdom	DPI 141	Druck	Every 5 minutes	0.15	0.0000	
6. Matera, Italy (MLRO)	1016B-01	Paroscientific	Every 5 minutes	0.10	2.0000	Every few years
7. McDonald Observatory, Texas USA	Met4	Paroscientific	Four times per hour	0.10	0.0000	As needed
8. Monument Peak, California USA	MET4	Paroscientific	Every pulse	0.08	-0.1500	Biyearly
9. Riyadh, Saudi Arabia	1720	Qualimetrics /Weathertronics	Per pulse	0.10	2.0000	(Yearly/ Monthly/etc)
10. Mt Stromlo, Australia	PTB220A	Vaisala Oyj	Daily	0.07	-2.3723	2 years
11. Mt Stromlo, Australia	WXT520	Vaisala Oyj	Every 10 seconds	0.50	0.2000	2 years
12. Wettzell, Germany (WLRS)	Digiquartz 740-16B	Paroscientific	Every 1 minute	0.10	0.0000	Yearly
13. Yarragadee, Australia	MET4	Paroscientific	Per pulse	0.08	0.0000	Yearly
14. Zimmerwald, Switzerland	Digiquartz 740-16B	Paroscientific	Every 30 minutes	0.20	2.0000	Every few years

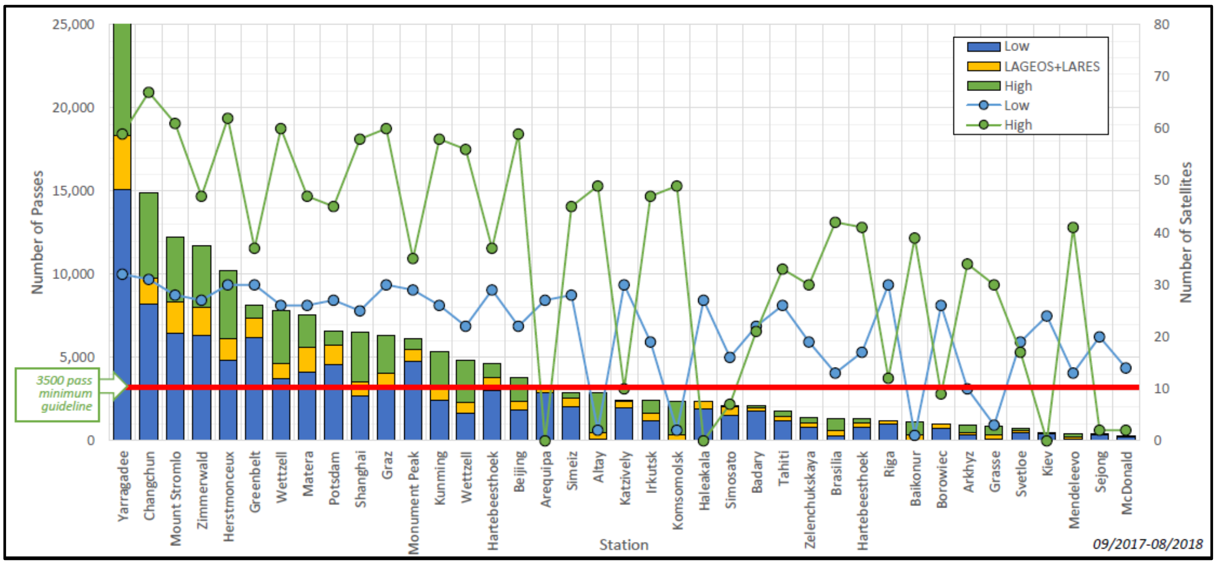

Figure 25. The ILRS global station performance report from September 2017 to August 2018. For this study, data collected from the MOBLAS-6 SLR system was used. It was also ideal because the majority of other ranging stations use MOBLAS systems for SLR ranging. It therefore provided a fairly uniform base to compare the results devoid of system biases. Source: ILRS, 2018.

3.2 Pressure conditions at ILRS stations

Before delving into the analysis, time series plots were retrieved from the ILRS repository and examined for any inconsistencies in pressure values and no abnormal data was detected. Beijing however exhibited a streak of lower than expected pressure values (see Figure 26). Similar plots for HartRAO and Yarragadee are shown in Figure 27 and Figure 28 respectively. It is also noted that Beijing had the highest error margin of ±17.11 mbar of average pressure. Regarding data throughput, Yarragadee had the highest number of normal points (256,327) with a ±5.34 mbar marginal error while HartRAO with ±3.64 mbar error margin had 47,970 normal points.

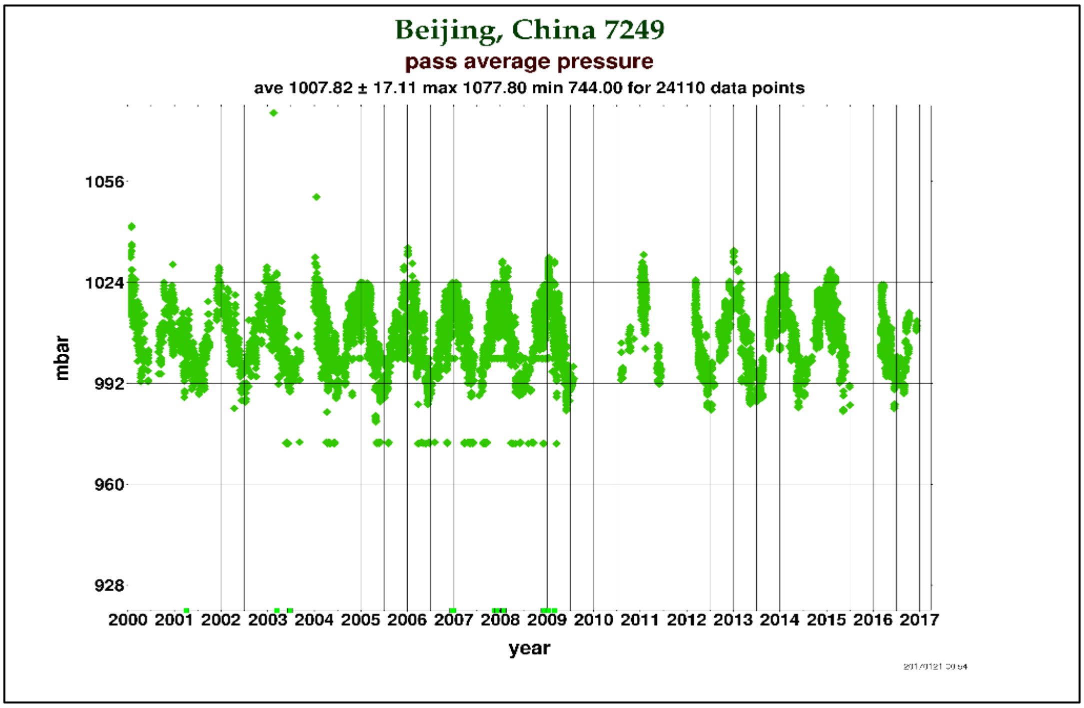

Figure 26. Average pressure at Beijing, China from 2000 – 2017. Source ILRS, 2018.

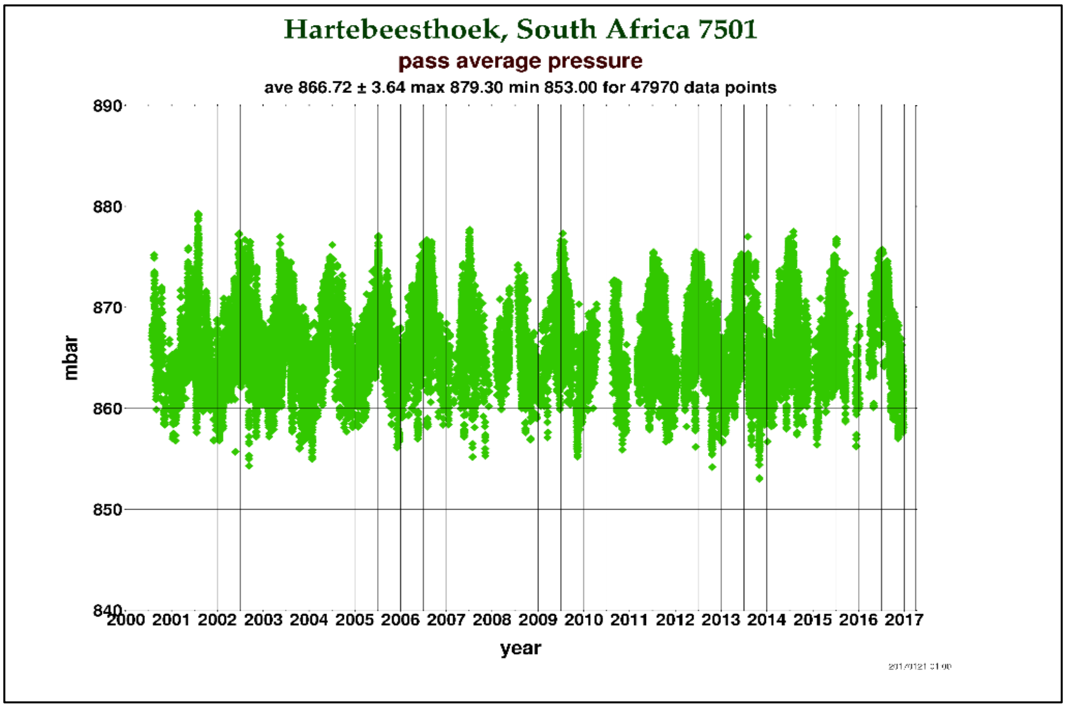

Figure 27. Average pressure at HartRAO, South Africa from 2000-2017. Source ILRS, 2018.

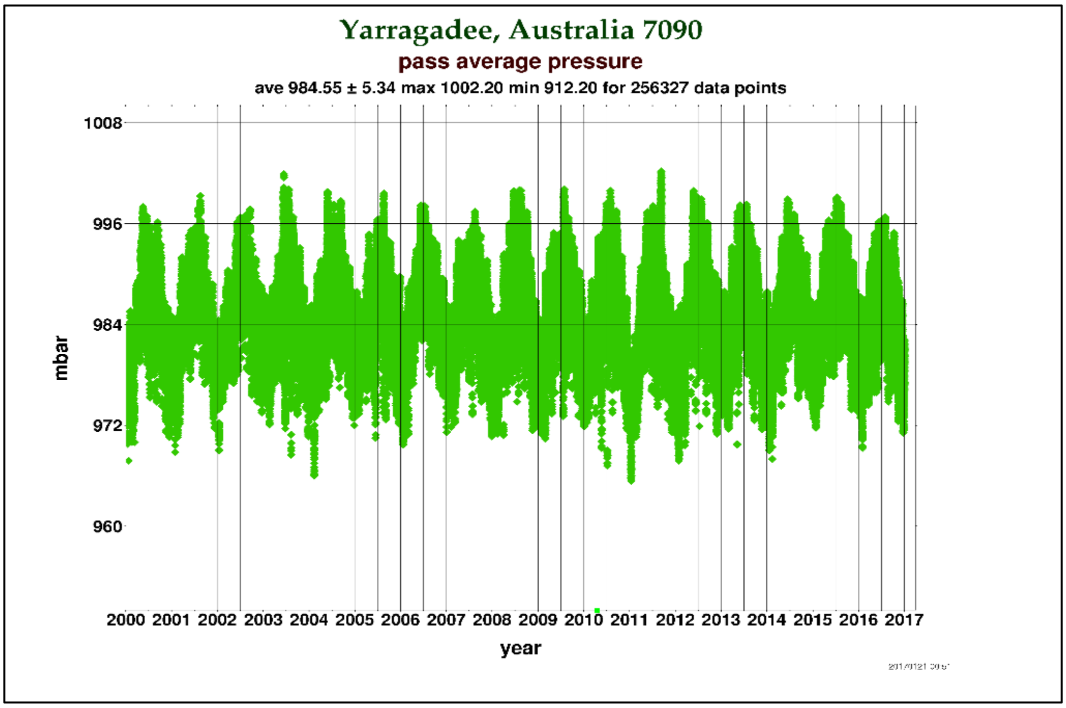

Figure 28. Average pressure at Yarragadee, Australia from 2000-2017. Source ILRS, 2018.

A summary of average pressure together with normal points realized from ranging observations are contained in Table 6. In the next section, an overview of the SDAS software is provided.

Table 6. Summary of ILRS stations depicting the number of normal points and pressure values from 2000 – 2017, Source: ILRS, 2018.

Station	No. of Normal points	Average Pressure (mbar)	Max (mbar)	Min (mbar)
1. Beijing, China	24110	1007.82±17.11	1077.80	744.00
2. Graz, Austria	108377	961.02±6.51	1,009.00	931.00
3. Greenbelt, Maryland (USA)	87380	1012.18±6.89	1,038.30	981.30
4. Hartebeesthoek, South Africa	47970	866.72±3.64	879.30	853.00
5. Herstmonceux, UK	98986	1015.37±9.18	1,041.80	964.00
6. Matera, Italy	68106	959.69±5.47	1,063.90	928.40
7. McDonald Observatory, Texas, USA	33855	800.15±3.73	996.90	728.00
8. Monument Peak, California, USA	88661	814.96±3.16	1,010.40	705.50
9. Mt. Stromlo, Australia	103595	927.81±7.69	946.70	-
10. Riyadh, Saudi Arabia	42495	926±10.06	946.40	600.20
11. Wettzell, Germany	103024	946.95±7.00	1,100.00	743.60
12. Yarragadee, Australia	256327	984.55±5.34	1,002.20	912.20
13. Zimmerwald, Switzerland	151919	916.45±5.39	951.57	883.93

3.3 Description of SDAS

The Satellite Data Analysis Software (SDAS) is a proprietary programme developed by Prof Ludwig Combrinck of HartRAO. It uses SLR data through a development and extension of the spaceflight dynamics library provided by Montenbruck and Gill (2000) of the Deutsches Zentrum für Luft- und Raumfahrt (DLR), Germany. The software is a robust application which incorporates the following attributes:

- The station position adjustment that depend on the tectonic plate movements,
- The corrections for site eccentricities,
- The Earth tide correction for station displacement,
- The solar reflection model for LAGEOS,
- The shadow function,
- The root mean square (RMS),
- The adjustment of the pole tides,
- The interpolation of pole offsets and correction to the exact time of observed epoch for pole tide,
- Range and time bias,
- Ocean loading,
- Relativistic corrections
- The corrections that relate to the gravity field data records which includes the model, Earth gravity constant, Earth radius, random errors, the reference epoch and tide system. The other parameters include satellite positions, velocities and epoch, station position, and atmospheric tide displacements.
- Satellite orbit perturbations due to Earth’s gravity field, the solid Earth tide, the Sun’s gravity, Moon and other planets; solar pressure, Earth’s radiation pressure (albedo); and atmosphere drag.
- SDAS uses Relative Humidity (%), Pressure (mbar) and Temperature (^{o}C).
- The azimuth and elevation of the satellite must be determined before ranging commences.
- The station inertial position, time and range bias are also key input parameters.
- Corrections due to the Earth, Ocean and the atmospheric tides are made.

- Lastly, the Centre of Mass correction, laser wavelength, atmospheric refraction correction, precession/nutation factors, radial or empirical bias and tectonic plate movements are also integral in the computations.

A more detailed description of the SDAS software is available in the publication by Combrinck and Suberlak, 2007. The analysis process is explained in the next section and a sequential process of the methodology is illustrated in Figure 29.

3.4 The analysis process

The first step was to retrieve SLR data, which is available at the ILRS archives. Preferred stations were identified and their metadata noted. The metadata includes station parameters such as the SRP, the IVP, the local site pressure, relative humidity and temperature; the types of meteorological instruments, the dates of installation or replacement, and more crucially, the height offset from the SRP. It was noted that some stations had not updated their details for several years. It was therefore important to verify and validate the metadata. An electronic questionnaire was send to contact persons of the ILRS network. Not all persons responded to the email. A summary of the responses was tabulated and compared with the information that was retrieved earlier. Some discrepancies were noted. In cases where variations were noted, a follow-up email was sent to seek more clarity. Some respondents replied while others did not.

After validating the metadata, the stations of interest were selected using the SDAS software. The software then loads relevant datasets and libraries. The option for atmospheric loading was deliberately unchecked so that the software does not attempt to correct atmospheric parameters (due to a predetermined threshold level). By default, the SDAS software completes a run after 20 iterations. Each subsequent iteration is an improved solution of the preceding. After roughly 15 iterations, the solution remains constant and the software may terminate before the 20th iteration. The solutions obtained from the 18th iteration were selected and tabulated. Thereafter, the SDAS code was deliberately altered by adjusting the station pressure (as a function of height) by small increments or decrements for example, +0.01 mbar or -0.01 mbar. The pressure increments were informed by the height offsets from the SRP.

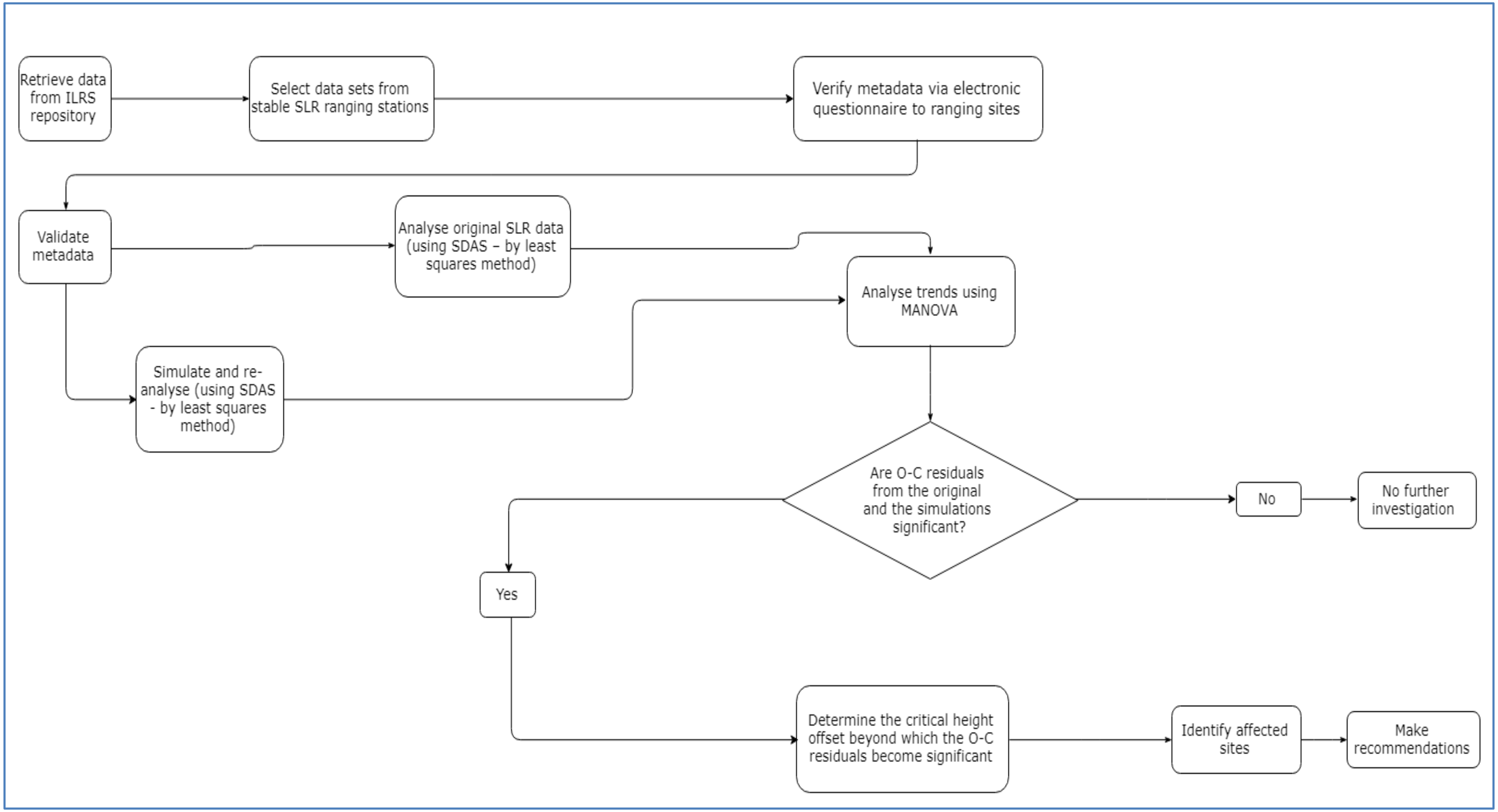

Figure 29. This is a flow diagram of the analysis process that was followed to evaluate the effect of pressure sensor height offsets to SLR observed minus computed (O-C) residuals.

The source code was saved, and used to analyse the same datasets. The analysis process was repeated up to ±1.0 mbar. The results tabulated and used to generate scatter plots.

It was evident by visual inspection that each adjustment to the station pressure had an effect on the O-C residuals. The other parameter of interest was the Rb. Both O-C and Rb were plotted against each other to determine if any correlation exists. To find out whether these visual changes were statistically significant, and whether there is any correlation between Rb and O-C, several tests were performed. The tests were F-Test, T-Test, ANOVA and Multivariate Analysis of Variance (MANOVA).

A detailed explanation of the analysis process using SDAS software is presented in the next section.

3.4 SLR data analysis

The SDAS system has a graphic user interphase (GUI) enabling the user to select or deselect some features. It relies on a library of constants stored in text files which are loaded by use of procedure or function calls. Some of these are listed as follows:

- The Earth Orientation Parameters (EOPs), the Gravity model (EGM2008) and the LAGEOS-2 drag model.
- The Earth, Pole and Ocean tides (displacements).
- Since our focus is on atmospheric parameters, and to avoid biases, the automatic atmospheric correction feature was disabled (this feature models possible azimuth effects).
- The planetary gravity perturbations considered include those of the Sun, Moon and Planets.
- Tides (gravity) used in this analysis are according to the IERS Technical Notes No 36, where IERS_3, Pole, and Ocean default values were selected. Further details are available at (https://www.iers.org).
- Adjustment to ITRF Epoch, Kalman filter, CoM (as provided by the ILRS),
- The average pole estimate and atmospheric delay.
- The reference frame epoch used was set to SLRF2005.
- Outlier values were set to be automatically rejected at 0.8 O-C sigma.
- The elevation mask was set to 10^{o}.

- Each arc was iterated 20 times and only the output from the 18th iteration were used. In few cases however, a solution was arrived at before the 18th iteration causing the run to be terminated. In such instances, the solution from the last loop was used.

The SDAS source code was modified by making minor adjustments to the pressure values and re-analysed. The baseline analysis was performed without making any changes to the data. The next run was at + 0.01 mbar then - 0.01 mbar, and the process repeated for all the alterations to the pressure values. The simulated results are indicative of what would happen to the range bias residuals if (a) there was an error with a similar magnitude in the values caused by instrument bias like pressure drift over time or (b) an error generated by altering the instrument height but not taking these into account during analysis (e.g. by not updating such changes in the site log file).

Chapter 4 Results and discussion

4.1 Survey results

A list of contact persons was compiled from the station log files that are available on the ILRS website. The log files contain details of both the primary and secondary contacts. An online survey requesting for specific information regarding the meteorological instruments at the ILRS tracking sites was done. The questionnaire consisted of the following:

- the pressure sensor model,
- the height offset between the SRP and the meteorological unit,
- the type of the SRP,
- the offset between the intersection of the telescope axes IVP and the SRP,
- whether the meteorological instrument is tied to the SRP and
- whether the heights provided are measured or estimated.

The responses were collated. Regarding height offsets, it was noted that some responses were filled with "~", for others approximate distances were provided and in other instances offsets were indicated as "unknown". These scenarios are omitted. Only 44 % of the respondents indicated that units have a zero offset. It was not clear from this feedback whether these units are measured from or estimated. Further enquiries for more clarity were unanswered.

It was noted that some metadata values obtained from the survey did not correspond with the site log sheets at the ILRS. For purposes of this study, values recorded in the site log sheet were used. Yarragadee provided the most detailed feedback, which included the error margin of their offsets to both the SRP and IVP. It was also noted that Yarragadee's site log file was up to date and information received from the survey tallied with what was retrieved from the site log. The feedback from respondents regarding the electronic questionnaire are contained in Table 7. The responses were recorded verbatim.

Table 7. The responses received in relation to the electronic questionnaire sent to the active ILRS stations. The header contains the information requested from the respondents.

#	Location Name, Country	Pressure Sensor Model	Height Difference to SRP (m)	What is your station SRP?	What is the offset between the intersection of the telescope axes and the SRP? (m)	Is this instrument tied to the SRP?	Is the distance measured or estimated?
1	Golosiiv, Ukraine	M67	-2.5	Intersection of the axes of the telescope	-2.5	-	-
2	Zelenchukskya, Russia	PTB220	0	Intersection of the telescope axes	0	Yes	Measured
3	Katzively, Ukraine	WMR928N	-3.5	Intersection of telescope axes	0	No	Measured
4	McDonald Observatory, Texas	MET4	0	The first non-translating mirror in the telescope	Complicated	-	Measured ± 1/4" or about 6.35 mm
5	Yarragadee, Australia	MET4	0	The monument is called Don95 - a brass plate below the telescope.	3.1820 ± 0.001	Not physically but distance between the SLR telescope IVP (Intersection of axis) and Don95 is resurveyed every two years.	Measured (see above). The reference height on the MET4A is set to match the IVP of the SLR telescope ± 5mm.
6	Monument Peak, California	MET4	-0.15	Monument/marker and the eccentricity together	0	They are the same	Eccentricity and monuments are measured by survey
7	Haleakala, Hawaii	MET4	0	Monument	2.632		Estimated
8	Beijing, China	PUT-200	-1.2	The intersection of the telescope axes	0	No	-
9	Hartebeesthoek, South Africa	MET4	-0.15	Intersection of Azimuth and Elevation axis	-0.15	Yes	Measured

#	Location Name, Country	Pressure Sensor Model	Height Difference to SRP (m)	What is your station SRP?	What is the offset between the intersection of the telescope axes and the SRP? (m)	Is this instrument tied to the SRP?	Is the distance measured or estimated?
10	San Fernando, Spain	EMA V	12*	A nearby point to the intersection between telescope axes.	<0.08	No	Measured by GPS
11	Mt Stromlo, Australia	PMT16A	-0.2863	Telescope IVP (intersection of axes)	-0.2863	No	Measured
12	Wettzell, Germany	Digiquartz 740-16B	0	Intersection of Azimuth and Elevation axis	0	Yes	Measured
13	Simosato, Japan	OW-7-420	-3	Center of operation device (telescope), i.e., intersection of the telescope axes	0	No, This instrument is set in the ground floor and telescope is set in the upper second floor.	Measured
14	Graz, Austria	DigiQuartz 740-16B	0	Telescope intersection	0	Yes	Measured
16	Herstmonceux, United Kingdom	MET3A	NO VALUE	Telescope axis intersection	0	No	Measured
17	Potsdam, Germany	PTU200	-5.2	The mid between the intersection of the telescope axes of transmit and receive telescope. (see comment)	-5.2	Yes	Measured

The intent of the questionnaire was to validate the metadata values on the log sheets and ascertain that the values in the site eccentricity file are accurate. Metadata per site is extracted into a site eccentricity file which is used during analysis.

4.2 Analysis of O-C residuals

4.2.1. O-C residuals across the whole SLR network

The derived O-C residuals represent the solution for the entire SLR network where 13 stations were analysed. Visual inspection of the baseline results compared with the output from adjusted pressure depict variations (see Figure 30 and Figure 31) where O-C residuals were plotted against modified Julian date (MJD). The two charts are for March and May 2006. They illustrate the diurnal variability accounted for by the fluctuations of environmental factors. In order to quantify these variations, further statistical analysis was conducted, and a summary of the findings is expounded in the Section 4.3.

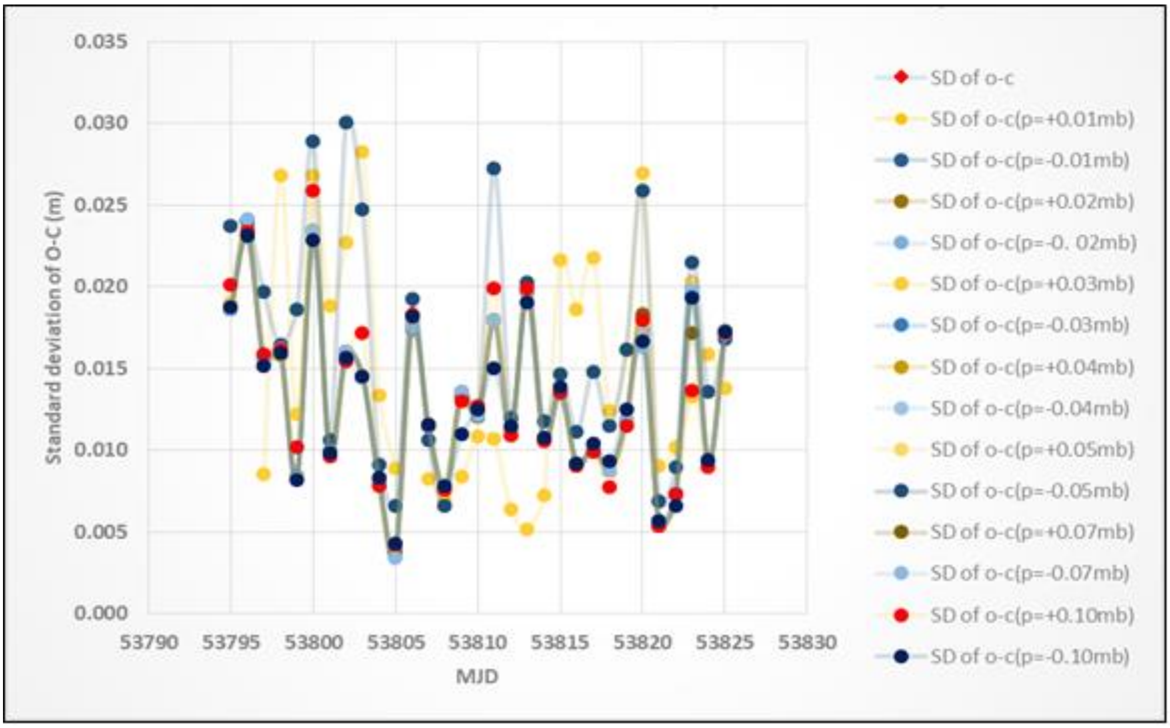

Figure 30. Standard deviation of O-C vs MJD for March 2006 for 13 stations.

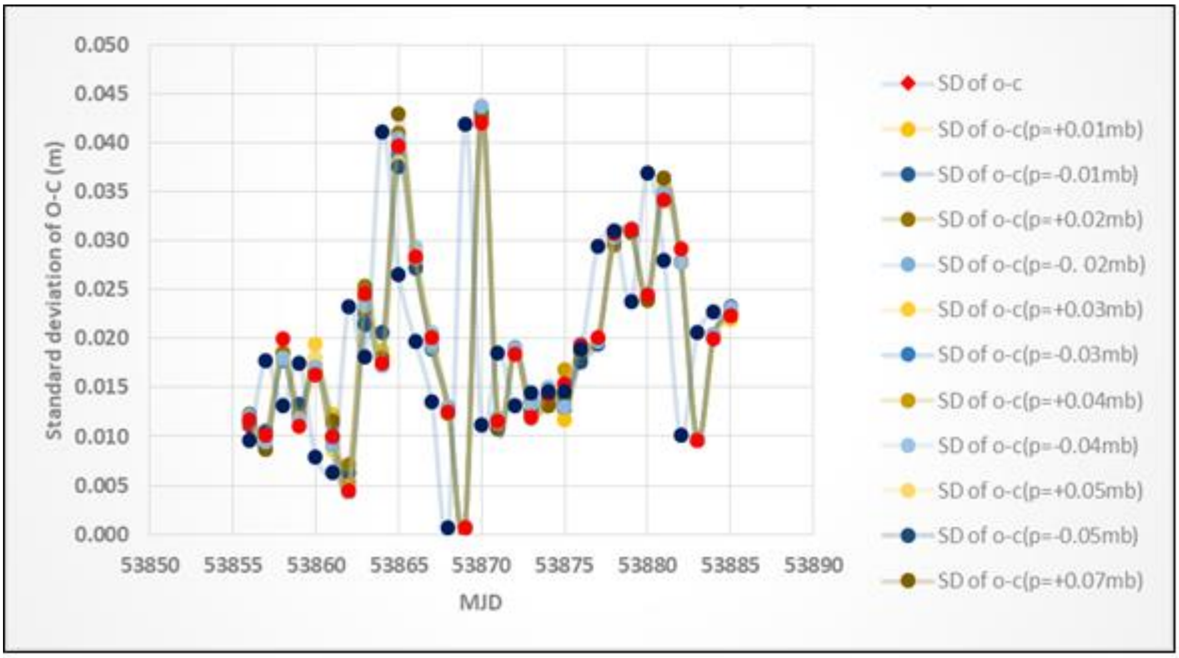

Figure 31. Standard deviation of O-C vs MJD for May 2006 across 13 stations.

To examine the influence of pressure changes on the SLR range biases at the SLR stations sites, Beijing and HartRAO were selected. Both stations have observations exceeding the minimum ILRS threshold of 3,500 passes and therefore suitable for comparison.

Further, Beijing is from the Northern Hemisphere while HartRAO from the Southern Hemisphere providing an opportunity for comparison. The two stations are also ranked closely in terms of their performance regarding the number of passes. The other station charts were similar and are appended in Appendix A3 Stepwise variation charts for O-C residuals. A brief discussion regarding the two stations is provided in the next section. In both charts, a rectangle with its top aligned with the maximum and the bottom to the minimum deviations of the baseline is superimposed. It is evident that pressure adjustments influence the range bias irrespective of the Hemisphere. This observation implies that global parameters being used currently are non-biased.

In each of the plots for Beijing, HartRAO and Yarragadee, a rectangle has been inserted to mark the minimum and maximum standard deviations of the O-C residuals. By visual inspection, it can be seen that whether the pressure alteration was positive or negative, the spikes exceeded the maximum and minimum values.

Beijing, China

Compared to the baseline Figure 32, larger spikes are observed when the pressure values are adjusted either negatively or positively (see the inset rectangle).

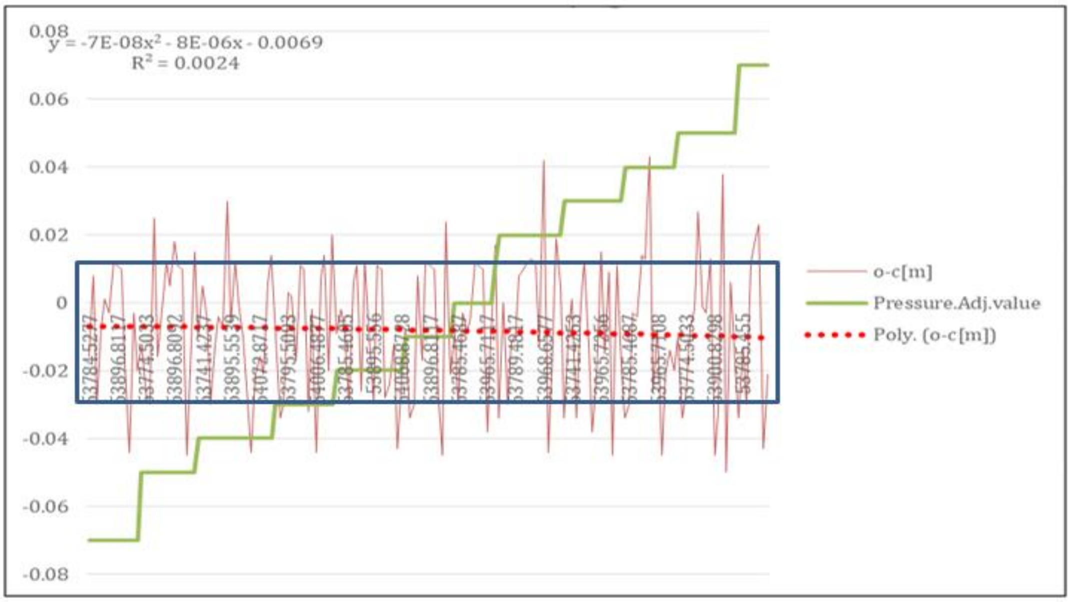

Figure 32. The O-C variations with stepwise adjustment of pressure for Beijing, China.

HartRAO, South Africa

The spikes also exceed the baseline values in both the negative and positive pressure adjustments (see the inset rectangle) as depicted in Figure 33.

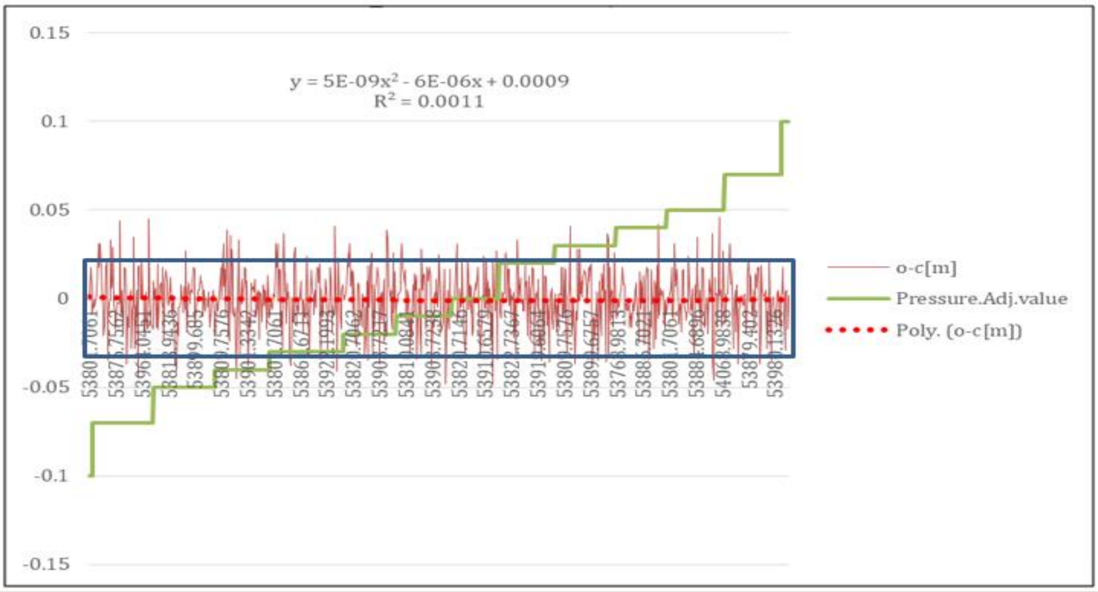

Figure 33 The O-C variations with stepwise adjustment of pressure for Hartebeesthoek, South Africa.

In general, it was expected that if pressure adjustments had no effect on the O-C residuals, the standard deviation of O-C could have matched the baseline i.e., remained within the rectangle in the inset. However, it is noted that larger spikes are evident on either side of the baseline points confirming the hypothesis that pressure influences the range computation. It is important to note that the variability pattern depicted in Figure 32 and Figure 33 are representative of the other stations.

Another dimension of the analysis was to zoom into HartRAO to determine if there is any correlation between the O-C residuals and the station range bias. Monthly means of both the range bias and the standard deviation of O-C was collated and plotted. The charts are contained in Figure 34 representing adjustment to the pressure values by -1 mbar (Top Row) , the 0 mbar or baseline (Middle Row) and +1 mbar (Bottom Row). More scattering in the plots where pressure was adjusted is noted.

The coupled variations depicted in Figure 34 arises because the objective of the model is to minimize the O-C residuals. In order to achieve this, other model parameterisations e.g., the range biases are adjusted. This is illustrated in Figure 35 and depicts the predicted plots for the average values at -1 mbar, baseline 0 mbar (i.e. no adjustment made to pressure) and +1 mbar. A linear fit is positive for pressure adjusted values in both the negative and positive pressure adjustments while it is negative for the baseline. This confirms that the model attempts to adjust the range bias among other parameters to minimize the standard deviation of the O-C residuals.

4.2.2. Site dependent O-C residuals

This analysis aimed at determining the influence of site dependent environmental factors on the O-C residuals. In order achieve this, a second set of analysis was conducted involving inserting a conditional loop in the source code where for station = 7501 (HartRAO) the pressure was adjusted by addition or subtraction of 1 mbar. In the baseline set of results (described in Section 4.2.1), no modification was made to the data sets. The O-C residuals were then plotted for daily, weekly and monthly time scales.

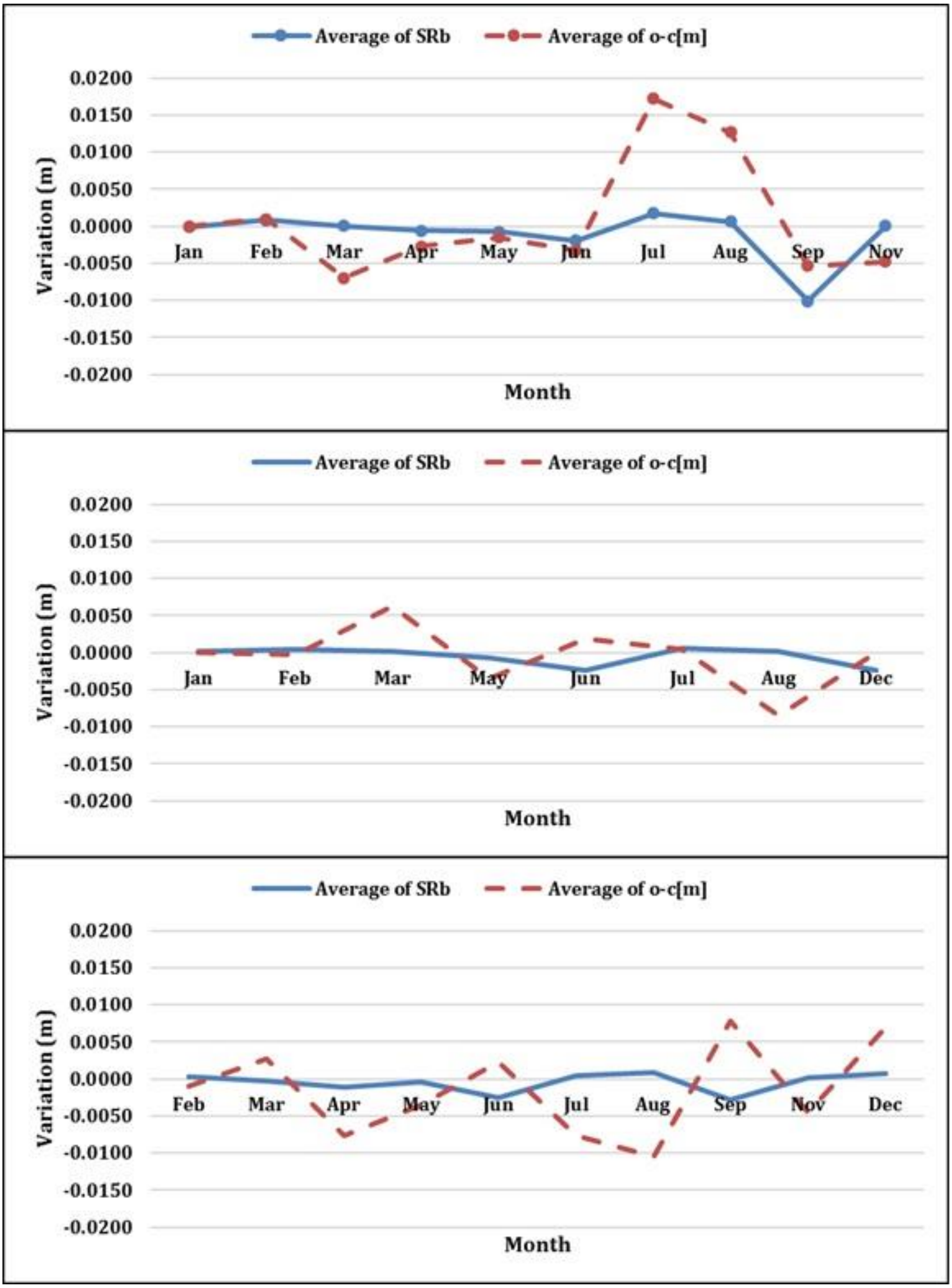

Figure 34. Comparison of monthly variation in range bias and standard deviation of O-C after adjusting pressure by -1 mbar (Top Row), 0 mbar baseline (Middle Row) and +1 mbar (Bottom Row) for HartRAO.

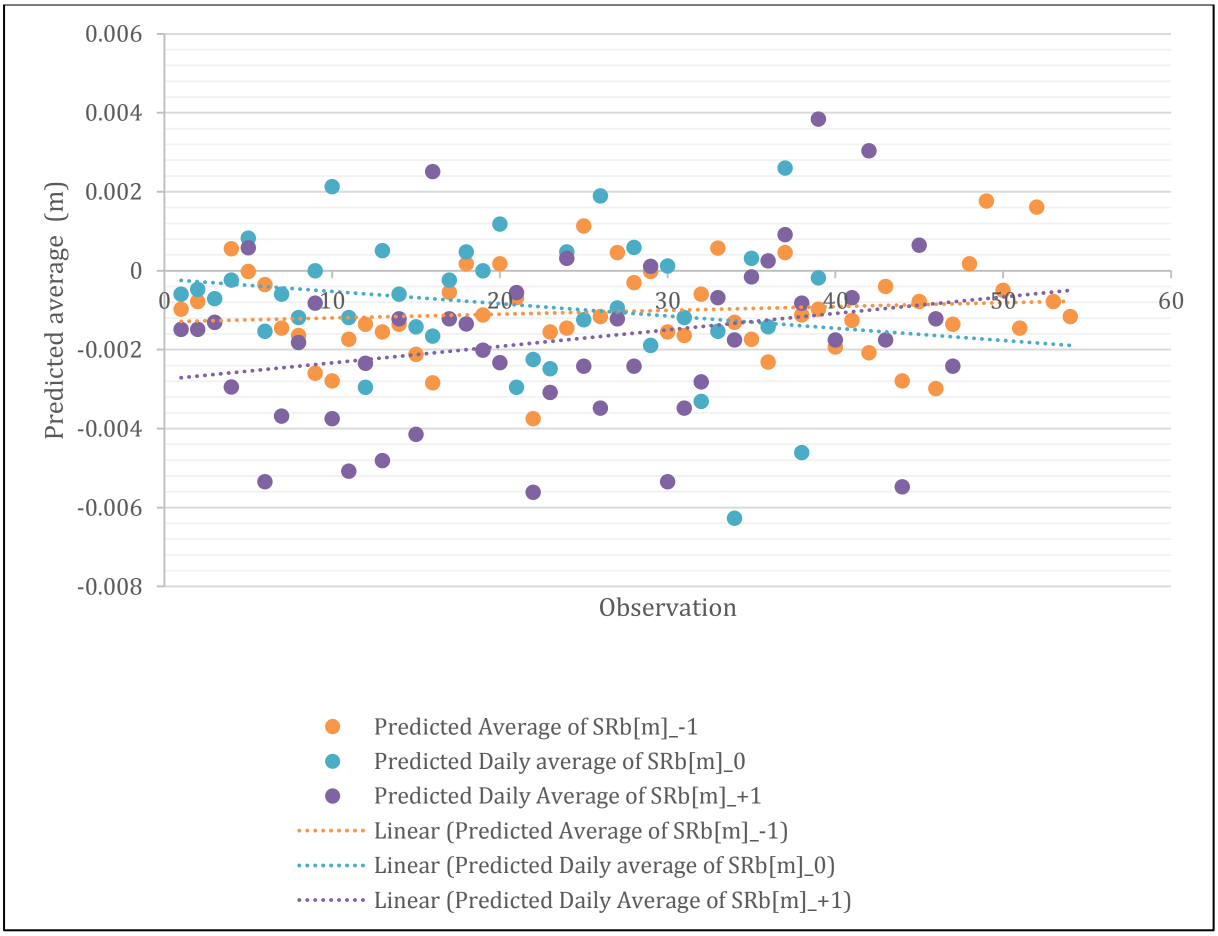

Figure 35. Predicted average values at -1 mbar, baseline (no adjustment made to pressure) and +1 mbar.

Finally, the O-C residuals vs Range bias values were derived to determine if there exists any correlation between the two parameters. The plots are illustrated in Figure 36.

There is a wider scattering of points with both a negative and a positive change in the pressure in the O-C vs Range bias. The unit for both variables is in metres. A summary of each data set’s regression statistics and ANOVA is appended as Table 12 – 17 in Appendix 9. The plots are arranged in sets of monthly, weekly and daily timelines for ease of visual comparison. The results depicted in Figure 36 and

Figure 37 confirm the dynamic alterations on range bias affecting localized deviations. The pressure changes cause an adjustment within the SDAS models to minimize the O-C whilst varying the range bias among other parameters. There is a more negative shift of points caused by – 1 mbar while the +1 mbar causes points to deviate to the right-hand side. Further, it is evident that the scattering of points is more pronounced in both negative and positive alterations of pressure.

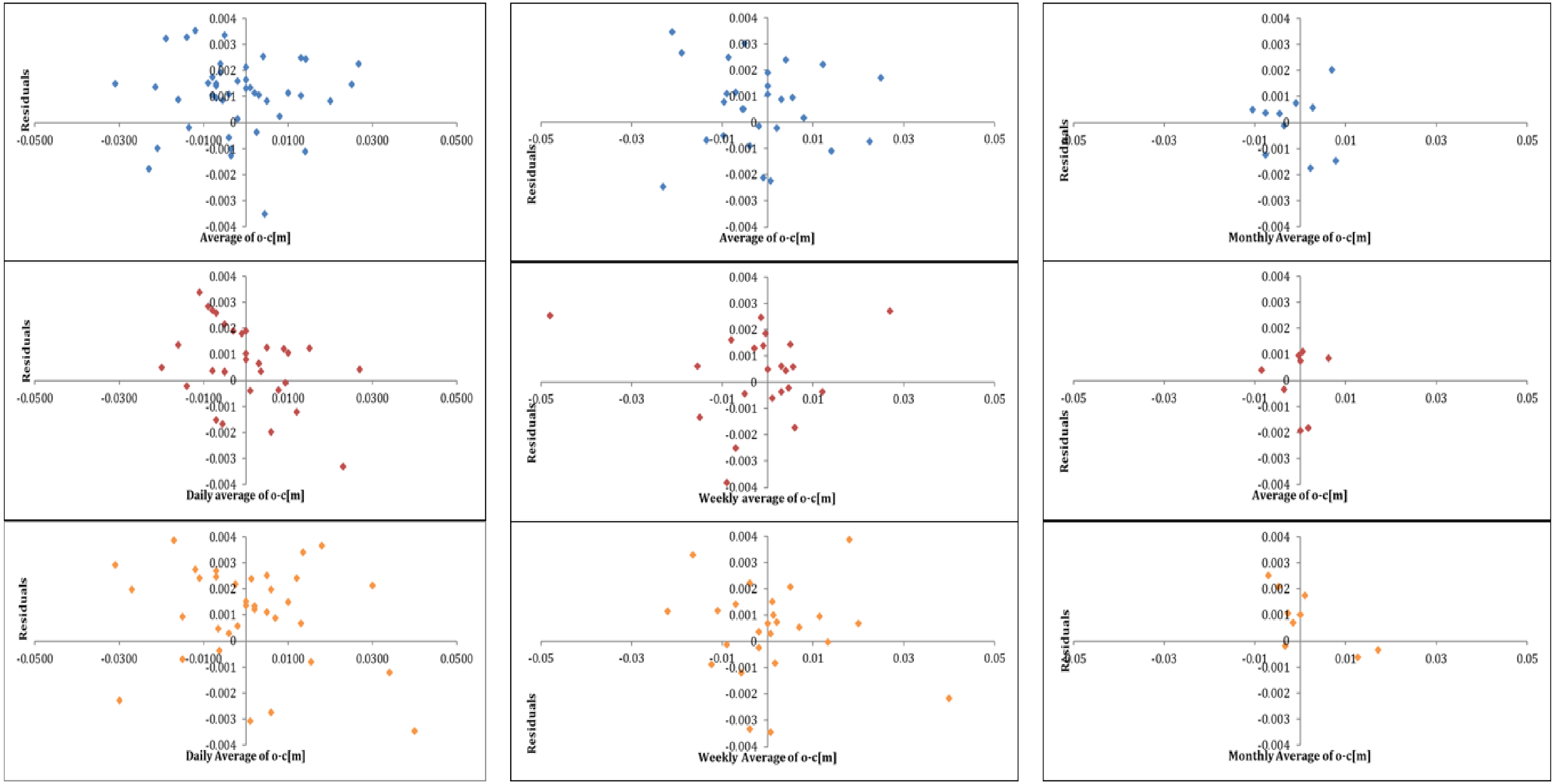

Figure 36. Residuals of O-C with and without pressure adjustment at one (HartRAO) SLR station. The residuals are for daily (column 1), Weekly (column 2) and Monthly (column 3) with Row 1 (-1 mbar), Row 2 (0 mbar) ad Row 3 (+1 mbar) pressure adjustments.

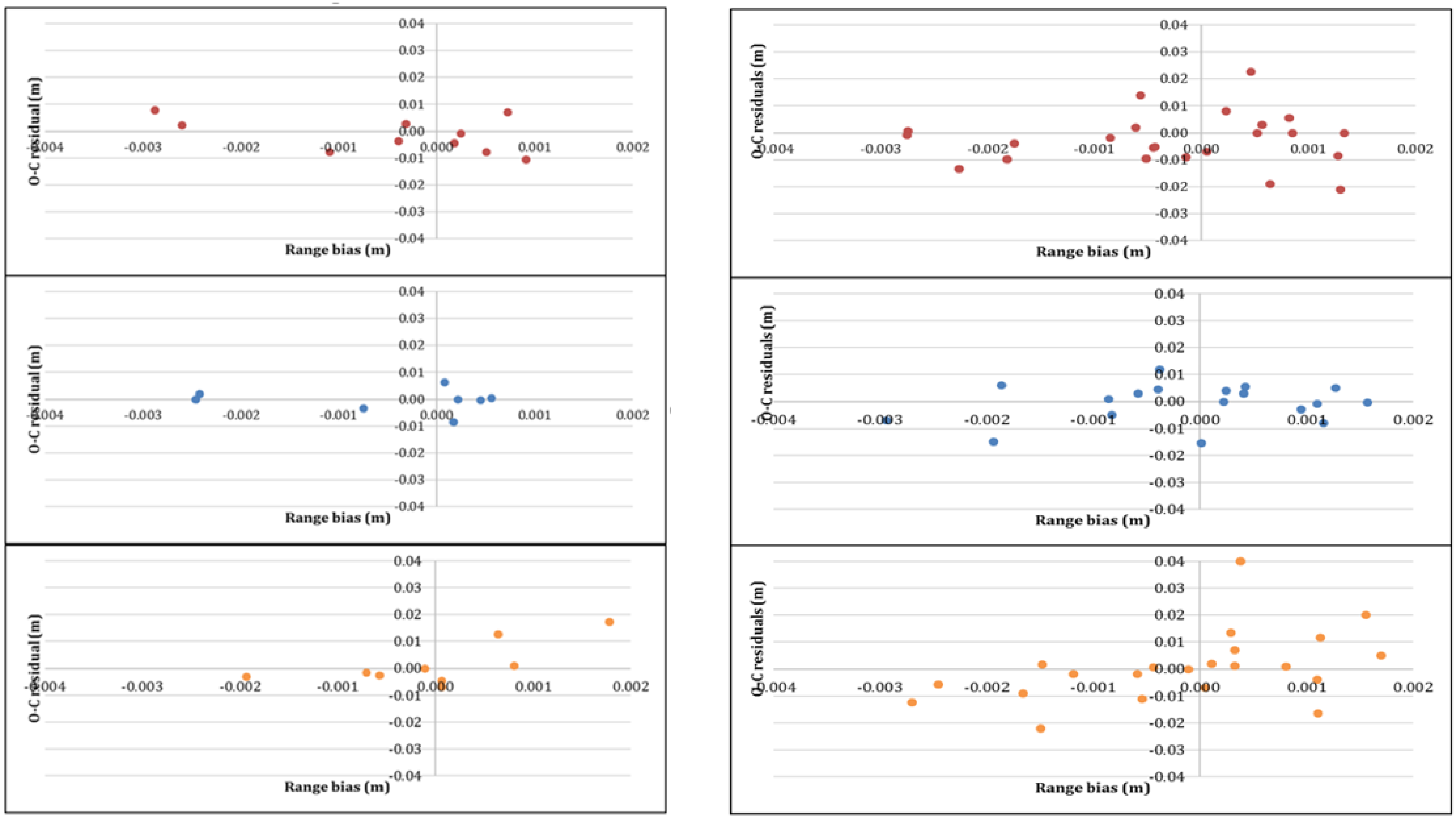

Figure 37. The monthly average (First Column) and weekly average (Second Column) of standard deviation of O-C (m) vs Rb (m) at pressure -1 mbar (Top Row), 0 mbar (Middle Row) and +1 mbar (Bottom Row).

4.3 Assessment of the differences between baseline and adjusted pressure O-C residuals

The O-C residuals were plotted and by visual inspection there is evidence that the pressure adjustments affected the results. However, in order to ascertain whether these differences are significant three statistical tests, namely the F-Test, t-Test and Analysis of Variance (ANOVA) were performed. A summary of each test together with the relevant results are presented. The F-statistic is a ratio of two variances, where the variances are a measure of how much the data are scattered from the mean value. Larger values indicate more dispersion. The T-test allows one to compare means between data sets. ANOVA is a valuable statistical method that determines whether there is a statistically significant difference among samples in a population.

4.3.1 F-Test two-sample for variances

The first step was to perform an F-Test to determine if the variances of both the baseline and the adjusted pressure results are equal. In this case, our baseline results (highlighted in grey) were used as the control and paired with results obtained by adjusting the pressure. The test was performed on the smallest ±0.01, the median ±0.05 and largest ±1.00 mbar adjustments (see Table 8). The outcome is that F > F critical one-tail hence we reject the null hypothesis that the variances of two populations are equal. On this premise, we proceeded to the next test.

4.3.2 t-Test two-sample for variances

The preceding F-Test confirmed that the variances are unequal. In performing the t-Test, we seek to determine if the means of the two sets (control and adjusted) are equal. The method used was a t-Test (two-sample assuming unequal variances). A two-tail test (inequality) was applied. Thus, if t-Stat < -t Critical two-tail or t Stat > t Critical two-tail then we reject the null hypothesis. A summary of the results is in Table 9.

The test was applied to the extreme ±1.00 mbar and subsequent levels of adjustments to be done to determine at what level the differences become significant. The results -2.160369 < 1.552496 < 2.160369, and -2.16037 < 1.77093 < 2.16037 imply that we cannot reject the null hypothesis that the means of the two samples are equal. Statistically therefore, the observed difference between the sample means is not sufficiently convincing to determine that the average O-C residuals between the baseline and adjusted pressure residuals are significantly different.

Table 8. F-Test two-sample for variances

	0.01	***0***	***-0.01***	***0***	***0.05***	***0***	***-0.05***	***0***	***1***	***0***	***-1***
Mean	0.005223	0.011532	0.006206	0.011532	0.004702	0.011532	0.004973	0.011532	0.004123	0.011532	0.003902
Variance	0.000021	0.000301	0.000097	0.000301	0.000028	0.000301	0.000022	0.000301	0.000012	0.000301	0.000013
Observations	13	13	13	13	13	13	13	13	13	13	13
Df	12	12	12	12	12	12	12	12	12	12	12
F		3.103911		10.73667		13.83694		13.83694		22.51161	
P(F<=f) one-tail		0.03043		0.000121		3.22E-05		3.22E-05		2.27E-06	
F Critical one-tail		2.686637		2.686637		2.686637		2.686637		2.686637	

Table 9. t-Test: two-sample assuming unequal variances

	0	*-1*	*0*	*1*
Mean	0.011532	0.003902	0.011532	0.004123
Variance	0.000301	1.34E-05	0.000301	1.19E-05
Observations	13	13	13	13
Hypothesized Mean Difference	0		0	
Df	13		13	
t Stat	1.552496		1.511189	
P(T<=t) one-tail	0.072271		0.077331	
t Critical one-tail	1.770933		1.770933	
P(T<=t) two-tail	0.144541		0.154661	
t Critical two-tail	2.160369		2.160369	

4.3.3 Analysis of variance (ANOVA) for O-C residuals

The last analysis was to test the null hypothesis that the means of several populations are all equal. In this case we combine all the adjustments together (including the baseline residuals) and analyse.

If F > F crit, then we reject the null hypothesis but in this case F= 1.055148572 while F crit = 1.693791. The results are summarised in Figure 38. Therefore, the null hypothesis holds true that the means of the 17 sets are all equal and therefore not statistically significantly different.

4.3.4 Analysis of variance (ANOVA) for Range bias (Rb) residuals

Another statistical test which was performed on the results was to the station range bias (Rb). During analysis, the software attempts to adjust other parameters to improve the solution until no further improvement can be achieved.

The Range bias (Rb) was examined, and the results are contained in Table 10. The outcome depicts that F < F crit hence we accept the null hypothesis that the means of the populations are equal despite the variations in values.

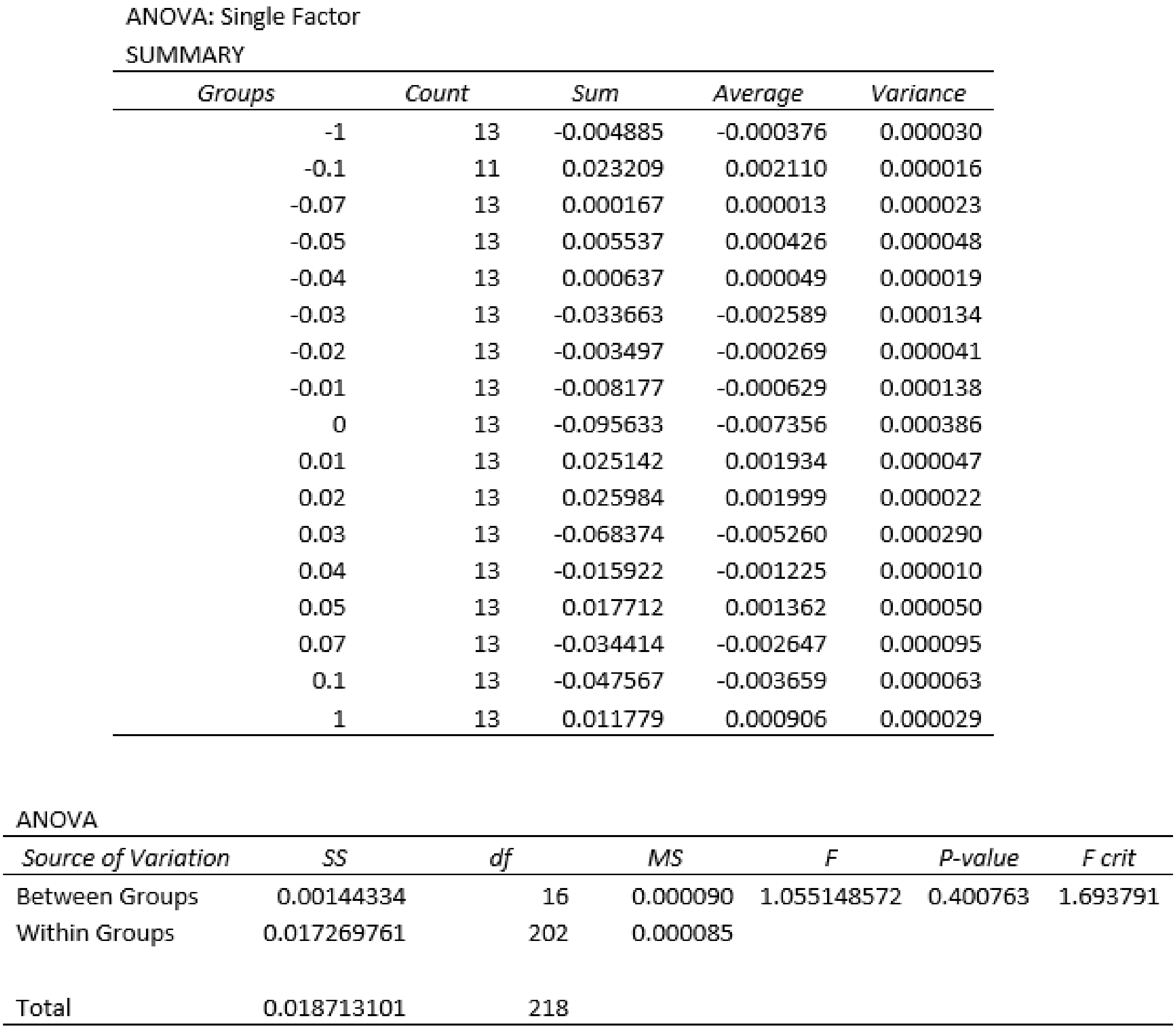

ANOVA: Single Factor

SUMMARY

Groups	Count	Sum	Average	Variance
-1	13	-0.004885	-0.000376	0.000030
-0.1	11	0.023209	0.002110	0.000016
-0.07	13	0.000167	0.000013	0.000023
-0.05	13	0.005537	0.000426	0.000048
-0.04	13	0.000637	0.000049	0.000019
-0.03	13	-0.033663	-0.002589	0.000134
-0.02	13	-0.003497	-0.000269	0.000041
-0.01	13	-0.008177	-0.000629	0.000138
0	13	-0.095633	-0.007356	0.000386
0.01	13	0.025142	0.001934	0.000047
0.02	13	0.025984	0.001999	0.000022
0.03	13	-0.068374	-0.005260	0.000290
0.04	13	-0.015922	-0.001225	0.000010
0.05	13	0.017712	0.001362	0.000050
0.07	13	-0.034414	-0.002647	0.000095
0.1	13	-0.047567	-0.003659	0.000063
1	13	0.011779	0.000906	0.000029

ANOVA

Source of Variation	SS	df	MS	F	P-value	F crit
Between Groups	0.00144334	16	0.000090	1.055148572	0.400763	1.693791
Within Groups	0.017269761	202	0.000085			
Total	0.018713101	218				

Figure 38. Analysis of variance (ANOVA) results for O-C residuals

Table 10. Results from the ANOVA for the range bias

Groups	Count	Sum	Average	Variance
-1	13	0.019433	0.001495	0.000007
-0.1	11	0.009903	0.000900	0.000012
-0.07	13	0.008857	0.000681	0.000004
-0.05	13	0.005148	0.000396	0.000004
-0.04	13	0.019925	0.001533	0.000005
-0.03	13	0.009368	0.000721	0.000008
-0.02	13	0.013450	0.001035	0.000003
-0.01	13	0.009075	0.000698	0.000007
0	13	-0.005690	-0.000438	0.000007
0.01	13	0.014684	0.001130	0.000014
0.02	13	0.007178	0.000552	0.000005

0.03	13	0.003875	0.000298	0.000007
0.04	13	0.005065	0.000390	0.000004
0.05	13	0.009611	0.000739	0.000007
0.07	13	0.009660	0.000743	0.000007
0.1	13	0.009383	0.000722	0.000005
1	13	-0.002848	-0.000219	0.000006

ANOVA

Source of Variation	*SS*	*Df*	*MS*	*F*	*P-value*	*F crit*
Between Groups	0.000054	16.000000	0.000003	0.511382	0.939569	1.693791
Within Groups	0.001333	202.000000	0.000007			
Total	0.001387	218				

4.3.5 Site sensitivity

In this section the sites were ranked to examine how the global adjustments affected their residuals. The intention was to determine if sites with zero height offsets had any advantage over those that had higher offsets as well as identify which sites were most sensitive to these variations.

Given that only site log sheets where site eccentricity files were extracted for analysis, it did not matter whether the survey results indicated that the values had been estimated or measured. The ranking of stations with the minimum deviations from the baseline are contained in Table 11 while those with the maximum deviations are in Table 12. It can be deduced from the findings that there is no advantage of zero offset at both Yarragadee and McDonald Observatory, Texas had zero-offsets yet they did not depict the same sensitivity. In all the 16 pressure adjustments Yarragadee had minimum disturbance in 6 while the most sensitive station to pressure adjustments was McDonald Observatory, Texas which had maximum deviations from the baseline in 5 pressure adjustments.

Table 11. The number of times a station appeared with the minimum deviation of O-C residual at different pressure adjustments

Station Name	Station Code	Count	offset
Yarragadee, Australia	7090	6	0.0000
Greenbelt, Maryland	7105	4	-0.1500
Mt Stromlo, Australia	7825	3	-0.2863
Matera, Italy (MLRO)	7941	2	2.0000
Hartebeesthoek, South Africa	7501	1	-0.1500
Zimmerwald, Switzerland	7810	1	2.0000
McDonald Observatory, Texas	7080	0	0.0000
Monument Peak, California	7110	0	-0.1500
Beijing, China	7249	0	-1.2000
Riyadh, Saudi Arabia	7832	0	2.0000
Graz, Austria	7839	0	0.0000
Herstmonceux, United Kingdom	7840	0	0.0000
Wettzell, Germany (WLRS)	8834	0	0.0000

Table 12. The number of times a station appeared with the maximum deviation of O-C residual at different pressure adjustments

Station Name	Station Code	Count	Column1
McDonald Observatory, Texas	7080	5	0.0000
Beijing, China	7249	4	-1.2000
Wettzell, Germany (WLRS)	8834	4	0.0000
Monument Peak, California	7110	1	-0.1500
Herstmonceux, United Kingdom	7840	1	-0.1500
Graz, Austria	7839	1	0.0000
Riyadh, Saudi Arabia	7832	1	2.0000
Yarragadee, Australia	7090	**0**	0.0000
Greenbelt, Maryland	7105	0	-0.1500
Matera, Italy (MLRO)	7941	0	2.0000
Hartebeesthoek, South Africa	7501	0	-0.1500
Zimmerwald, Switzerland	7810	0	2.0000
Mt Stromlo, Australia	7825	0	-0.2863

4.4 Summary

It was noted that there were some discrepancies of metadata between the feedback from the electronic survey and the site log sheet. There is need to ensure that the log sheet is updated frequently. For instance, in the case of Zimmerwald, Switzerland the meteorological unit was installed in 1997 and is still in use. There is no indication if any maintenance has been performed and this creates doubt if indeed it is still the same unit after more than 20 years of operation. An annual update regarding such an instrument would greatly alleviate any doubts. Besides what is the shelf life of a meteorological unit? If indeed the unit is still functional how reliable is the current meteorological data?

According to Stefan Riepl's email correspondence dated 3rd June 2019, a backtracking analysis of the pressure sensor offset at the Geodetic Observatory Wettzell, Germany revealed a drift of approximately -0.025hPa/year. The faulty sensor was replaced on 2019-05-28 18:15 UT and data delivered before 2019-05-28 18:15 UT to be corrected for release. Are other stations performing periodic calibrations? It is noted from the survey feedback that the calibration time varies from 1 year, 2 years, "every few years" and "as needed". Given that pressure sensor drifting has been noted in Wettzell, is it not prudent for other stations to perform frequent calibrations?

Although there is clear visual evidence from the plots that adjusting pressure values affects the O-C residuals, statistical analysis depicts no statistically significant differences between the variances of paired groups (the baseline and the adjusted pressure results). Further, it is determined that the means of paired groups (the baseline with any pressure adjusted results) and the entire set of all the results are not significantly different.

The analysis of SLR data is time consuming and resource intensive. There is need to perform analysis on a lager dataset for a longer duration for more insight.

Lastly, the height of the pressure sensor need not be at zero offset to the IVP as there is no evidence of any advantage in determining the range bias.

Chapter 5 Conclusion and recommendations

5.1 Conclusion

This study has demonstrated that there is an effect of pressure values on the ranging solutions after scrutinizing the standard deviation of O-C residuals. Ranging sites that registered measured values had better results compared to those that did not. Further those that had large offsets from the IVP also had larger errors compared to those that recorded 0 offset. There is need to ensure that all estimated values are measured. It is very crucial especially for the ranging sites in the Southern Hemisphere to minimize chances of their data being rejected (e.g. as outlier values) by the analysis software so that their input contributes towards generating more representative global parameters to improve the atmospheric correction models. Errors that can be mitigated should therefore be addressed.

5.2 The main objectives *vis a vis* the results

The main objectives of this study are:

1. *To assess the accuracy of the height offsets between meteorological sensors and the SLR invariant point recorded in the SLR site log sheets.*

   Site log files from active ILRS sites were retrieved from the database repository. In one instance, the met unit on the log file was installed in 1997. To validate metadata, an online survey was conducted by sending an email questionnaire to contact persons. The responses obtained were summarized and tabulated. Some discrepancies were noted. Further, personal communication was made to the Secretary, ILRS Central Bureau, Carrey Noll as of July 2018 to seek clarity on the network status.

2. *To determine the effect of pressure differences due to simulated sensor height offsets on the SLR ranges biases.*

   Data was analysed ‘as is’ and latter changes made to the pressure values in source code of SDAS written in C++ programming language. Visual examination confirmed that there were differences in the O-C residuals for all the pressure adjustments. To determine whether these differences were significant, an F-Test, t-Test and ANOVA were performed. Accordingly, there is no statistically significant difference in the means of all the O-C residuals with or without pressure adjustments.

3. *To characterize the differences of the sensor height offsets and SLR range biases across the SLR network.*

   The minimum offset at zero metres and the maximum is -2.3723 m. According to the results, the heights do not disadvantage a station during analysis. In ranking both the stations with the minimum and maximum deviations, there lacks evidence to determine that those with lesser offsets outperformed those with higher offsets. However, since all stations experienced variations to the O-C, it is important to ensure that the pressure instrument position is known precisely.

5.3 Recommendations

Based on the outcome of the analysis it is recommended that:

1. A long term SLR network range bias analysis be performed. The outcome will be useful to determine any trends or abnormal results that may be attributed to changes in instruments, seasons or even personnel (SLR operators).
2. For future stations the meteorological units, specifically the actual height of the barometric centre must be tied in to the ITRF, the SRP and IVP. In this regard, the term ‘height of a meteorological instrument’ should be clarified to determine the exact reference point on the instrument.
3. The ILRS to perform an audit to verify if there have been any changes to instrumentation at stations which reported to have estimated their meteorological instrument height offsets.
4. Further, stations should be urged to update their log files as soon as any system changes occur. This will enable association of any abnormal behaviour in the results to the event that occurred at the specific site during the time period where an anomaly is detected.
5. Pressure sensor drifting of -0.025 hPa/year has been detected at the Geodetic Observatory Wettzell making it crucial for other SLR network stations to calibrate their instruments frequently.

References

Abshire, J. B., and Gardner, C. S. 1985. Atmospheric Refractivity Correction is Satellite Laser Ranging. *IEE Transactions on Geoscience and Remote Sensing*, vol. 23 no.4, pp. 414-425. [Online] Available from: https://ieeexplore.ieee.org [Accessed 14 October 2018].

Boller and Chivens. 2020. *Boller and Chivens*. Available from: http://bollerandchivens.com/. [Accessed 08 February 2020].

Ciddor, P. E. 1996. Refractive index of air: New equations for the visible and near infrared. *Applied Optics*, vol.35, no.9, pp. 1566-1573. [Online] Available from: https://www.osapublishing.org/. [Accessed 14 October 2018].

Aviso + Satellite Altimetry Data. 2018. *CNES/AVISO*. [Online]. Available from: http://www.aviso.altimetry.fr. [Accessed 14 October 2018].

Combrinck, L. Satellite Laser Ranging. 2010. Satellite Laser Ranging. In: *Sciences of Geodesy*. Edited by Xu G. Berlin, Heidelberg, Germany. Springer. [Online]. Available from: https://www.researchgate.net. [Accessed 15 October 2018].

Combrinck, L. and Suberlak, V. 2007. Earth-tide as parameter for crustal motion correction for SLR station displacement. *South African Journal of Geology*, vol.110,e no.2-3, pp. 203-210. [Online]. Available from: https://www.researchgate.net [Accessed 15 October 2018].

Coulot, D., Berio, P. H., Laurain, O., Feraudy, D. and Exertier, P. 2006. An original approach to compute SLR ranging biases. *Proceedings of the 15th International Laser Ranging Workshop*. Canberra, Australia. [Online]. Available from: http://lareg.ensg.eu [Accessed 15 October 2018].

Degnan, J. J. 1985. Satellite Laser Ranging: Current status and future prospects. *IEEE Trans. on Geoscience and Remote Sensing*, vol.23, no.4, pp.398-413.

Degnan, J. 2006. The History and Future of Satellite Laser Ranging - ILRS - NASA. *ILRS.* [Online]. Available from: https://ilrs.cddis.eosdis.nasa.gov [Accessed 15 October 2018].

Donovan, H., Patterson, D., Wetzel, S., Marzouk, J., Mcgarry, J., Degnan, J., Nelson, A., Hall, F., Horvath, J., Cheek, J., Shappirio, M. and Hoffman, E. 2016. 'The Gimbal and Telescope Assembly for NASA's Next Generation Space Geodesy SLR Systems'. *20th International Laser Ranging Workshop. Potsdam, Germany October 9 – 14.*

Doornbos, E. and Willis, P. 2007. Analysis of DORIS range-rate residuals for TOPEX/Poseidon, Jason, Envisat and SPOT. *Acta Astronautica*, vol.60, no.8-9, pp.611-621.

Dunn, P., Pearce, W. and Borman, K. 1984. The effects of atmospheric refraction in laser ranging measurements. *Proceedings of the General Meeting International Geodesy. Tokyo, Japan. September.*

ESA. 2018. *European Space Agency*. [Online]. Available from: http://www.esa.int [Accessed 15 October 2018].

Exertier, P., Nicolas, J. and Barlier, F. 2000. SLR: A point of view on scientific achievements and future requirements. *12th International Workshop Laser Ranging. Matera, Italy.*

Fisher, S., Johnston, G. and Neilan, R. 2016. Global Geodetic Observing System of the International Association of Geodesy Status Report. *IAG.* [Online]. Available from: http://www.iag-aig.org/. [Accessed 15 October 2018].

Freeman, J. J. 1962. Range error compensation for a troposphere with exponentially varying refractivity. *Journal of Research of the National Bureau of Standards-D. Radio Propagation,* vol.66, no. 6, pp. 695-697.

Früngel, F. B. A. 1965. *Optical Pulses – Lasers - Measuring Techniques.* Academic Press. Cambridge, Massachusetts.

Gardner, C. S. 1977. Correction of laser tracking data for the effects of horizontal refractivity gradients. *Appied. Optics*, vol.16, no.9, pp.2427-2432. [Online]. Available from: https://www.osapublishing.org/ [Accessed 15 October 2018].

Gibbs, B. P., and V. Majer. 1981. 'Accuracy assessment of the atmospheric correction used in the NASA laser ranging program'. *Business and Technology Systems Technical Report*. pp. 81-166. [Online] Available from: https://wenku.baidu.com/ [Accessed 15 October 2018].

Gross, R. S. 2009. Ocean tidal effects on earth rotation. *Journal of Geodynamics*, vol.48, no. 3, pp.201-225.

HartRAO. 2018. *Hartebeesthoek Radio Astronomy Observatory*. [Online]. Available from:http://hartrao.ac.za. [Accessed 15 October 2018].

Hegarty, C. J. and Chatre, E. 2008. Evolution of the Global Navigation Satellite System (GNSS). *IEEE*, vol.96, no. 12. [Online]. Available from: https://wenku.baidu.com [Accessed 15 October 2018].

Hopfield, H.S. 1969. Two-quartic tropospheric refractivity profile for correcting satellite data. *Journal of Geophysical Research,* vol.74, no.18, pp. 4487-4499.

Hulley, G. and Pavlis, E. C. 2007. Improvement of Current Refraction Modeling in Satellite Laser Ranging (SLR) by Ray Tracing through Meteorological Data. *Journal of Geophysical Research: Solid Earth*, vol.112, no.B6.

IAC. 2018. *Information and Analysis Center for Positioning, Navigation and Timing*. [Online]. Available from: http://www.glonass-iac.ru. [Accessed 15 October 2018].

IAG. 1963. *Resolution No. 1 of the 13th General Assembly*. [Online]. Available from: http://www.iag-aig.org [Accessed 15 October 2018].

IDS. 2018. *International DORIS Serive* .[Online]. Available from: http://ids-doris.org [Accessed 15 October 2018].

IGS. 2018. *International GNSS Service*. [Online]. Available from: http://www.mgex.igs.org [Accessed 15 October 2018].

ILRS. 2018. *International Laser Ranging Service*. [Online]. Available from: http://ilrs.gsfc.nasa.gov/. [Accessed 15 October 2018].

ISRO. 2018. *Indian Space Research Organization*. [Online]. Available from: http://www.isro.gov.in. [Accessed 15 October 2018].

Johnson, T. S., Plotkin, H. H. and Spadin, P. L. 1967. A laser satellite ranging system - Part 1: Equipment description. *IEEE Journal Quontum Electronics*, vol.3, pp.435-439.

Johnston G., Riddell A., Hausler G. (2017) The International GNSS Service. In: Teunissen P.J., Montenbruck O. (eds) Springer Handbook of Global Navigation Satellite Systems. Springer Handbooks. Springer, Cham. https://doi.org/10.1007/978-3-319-42928-1_33

Kaula, W. 1982. The Terrestrial Environment: Solid Earth and Ocean Physics. *Applications of Space Research Letters*, vol.9, pp.1263-1266.

Marini, J. W. 1972. Correction of Satellite Tracking Data for an Arbitrary Tropospheric Profile. *Radio Science*, vol.7, no.2.

Marini, J. W. and Murray, C. W. 1973. Correction of Laser Tracking Data for Atmospheric refraction at Elevation Angles Above 10 Degrees. Maryland, USA: GSFC, 1973.

Mendes, V. B., Prates, G., Pavlis, E. C., Pavlis, D. E. and Langley, R. B. 2002. Improved mapping functions for atmospheric refraction correction in SLR. *Geophysical Research Letters*, vol.29, no.10.

Mohinder, S. G., Angus, P. A. and Chris, G. B. 2013. *Global Navigation Satellite Systems, Inertial Navigation, and Integration*. 3rd ed. Wiley-Interscience.

Montenbruck, O. and Gill, E. 2000. *Satellite orbits: models, methods and applications*. Berlin: Springer.

NASA. 2018. *National Aeronautics and Space Administration*. [Online]. Available from: http://igscb.jpl.nasa.gov/. [Accessed 15 October 2018].

Niell, A. E. 1996. Global mapping functions for the atmosphere delay at radio wavelengths. *Journal of Geophysical Research*, vol.101, no.B2, pp.3227-3246.

Paroscientific. 2018. *Paroscientific Instruments Inc.* [Online]. Available from: http://www.paroscientific.com. [Accessed 15 October 2018].

Pearlman, M. 1984. Laser System Characterization. [Online]. Available from: https://ilrs.cddis.eosdis.nasa.gov/ [Accessed 15 October 2018].

Pearlman, M. and Taggart, L. 1999. 1999 Annual Report. [Online]. Available from: https://ilrs.cddis.eosdis.nasa.gov/ [Accessed 15 October 2018].

Petrachenko, W. T., Niell, A. E., Corey, B. E. Behrend, B. Schuh, H. and Wresnik. J. 2012. *Next_Generation VLBI System for Geodesy and Astrometry*. Berlin, Heidelberg: Springer.

Plag, H. P., and Pearlman, M. (eds.). 2009. *Global geodetic Observing System Meeting the Requirements of a Global Society on a Changing Planet in 2020*. Berlin, Heidelberg: Springer.

Pugh, J. 2004. History of satellite laser ranging in Australia. [Online]. Available from: https://cddis.nasa.gov/. [Accessed 15 October 2018].

QZSS. 2018. *Quasi-Zenith Satellite System*. [Online]. Available from: http://www.qzss.go.jp [Accessed 15 October 2018].

Rowlandson, L., and Moldt. 1969. Derivation of Closed Functions to Compensate Range and Angle Errors in an Exponential Atmosphere. *Radio Science*, vol.4, no.10, pp.927-933.

Saastamoinen, J. 1972a. Atmospheric Correction for Troposphere and Stratosphere in Radio Ranging of Satellites. Edited by A. M. Soren, W. Henriksen, and B. H. Chovitz. American Geophysical Union, Geophysical Monograph, vol.15, pp.247.

Saastamoinen, J. 1972b. Contributions to the theory of atmospheric refraction, Part II: Refraction corrections in satellite geodesy. *Bulletin Geodesique*, vol.105, no.1, pp.279-298.

Saastamoinen, J. 1972c. Introduction to practical computation of astronomical refraction. *Bulletin Geodesique*, vol.107, no.383.

Schutz, B. E., Tapley, B. D. and Eanes, R. J. 1983. ‘Earth Rotation from Laser Ranging to LAGEOS’. *BIH Annual Report for 1983*, Paris.

Shimon, Y. N., Weiner, A. M. and Cheng, G. J. 2014. *Laser and Photonic Systems: Design and Integration*. CRC Press.

Smith, D. E., Kolenkieweiz, R., Dunn, P. J., Robbins, J. W., Torrence, M. H., Klosko, S. M., Willianson, R. G., Pavlis, E. C., Douglas, N. B. and Fricke, S. K. 1990. Tectonic plate motion and deformation from satellite laser ranging to LAGEOS. *Journal of Geophysical Research* vol.013-22, no.041, pp.22.

UN. 2018. *United Nations Global Geospatial Information*. [Online]. Available from: http://ggim.un.org. [Accessed 15 October 2018].

Appendices

Appendix A1 MET4 Specifications

Source: Paroscientific, 2018.

PRESSURE

Accuracy[1]	Better than ±0.08 hPa
Stability	Better than 0.1 hPa per year
Range	500 - 1100 hPa (7-16 psia)
Maximum Pressure	1240 hPa (18 psia)

TEMPERATURE

Performance MET4	Better than ±0.5° C
Performance MET4A (Fan-Aspirated)	Better than ±0.1° C
Resolution	0.01° C
Range	-40°C to +60°C (-40 °F to +140 °F)

HUMIDITY

Performance	Better than ±0.8% RH at 23°C
Range	0 to 100% non-condensing

ENVIRONMENTAL

Weight MET4	7.3 lb (3.31 Kg)
Calibrated Temperature Range	-50°C to +60°C
Power Requirements (MET4)	Operates from 5 to 16 VDC
Typical Current Consumption MET4	Standard Resolution (Parts per million) 40 mA MAX Nano-Resolution (Parts per billion) 70 mA MAX

Description

Model No. Part No.	Description
MET4 1563-301	Standard Configuration (Non-Aspirated) w/ Barometric Functions and Data Logging
MET4A 1564-301	Standard Configuration (Fan-Aspirated) w/ Barometric Functions and Data Logging

(1) Accuracy relative to the primary standard includes pressure hysteresis, repeatability, linearity and temperature conformance.

Appendix A2 ILRS Data Record Template

(Revision 1 - March 1997); (Revision 2 - August 2004). Source: ILRS, 2018.

Column	Description	Example
1-12	Time of day of laser firing, from 0 hours UTC in units of 0.1 microseconds. Value is given module 864000000000 if pass crosses 24 hours UTC	'214360786545'
13-24	Two-way time-of-flight corrected for system delay, in picoseconds. Not corrected for atmospheric delay, nor to the center-of-mass of the satellite.	'052035998000'
25-31	Bin RMS from the mean of raw range values minus the trend function, for accepted ranges. Two-way value in picoseconds. If point is a single raw data point, then use pass RMS.	'0000066'
32-36	Surface pressure, in units of 0.1 mbar	'10052'
37-40	Surface temperature in units of 0.1 degree Kelvin	'2932'
41-43	Relative humidity at surface in percent	'092'
44-47	Number of raw ranges (after editing) compressed into the normal point. *See Note 1: below*	'0108'
48	A flag to indicate the data release: 0: first release of data 1: first replacement release of the data, 2: second replacement release, etc.	'0'
49	For SLR data: not used before revision 2. Revision 2 and above, indicates power of ten with which to multiply number stored in bytes 44-47 in order to provide a very close approximation to the total number of returns for high yield systems (kHz systems). For LLR data: integer seconds of the two-way time of flight (columns 13-24 contain the fractional part).	'2'
50	For SLR data: not used For LLR data: normal point window indicator. Indicates the time span of the normal point (can be variable from point to point). 1: <= 5 minutes 2: 10 minutes 3: 15 minutes 4: 20 minutes 5: 25 minutes 6: 30 minutes 7: 35 minutes 8: 40 minutes 9: >= 50 minutes	'1'
51-52	For SLR data: not used For LLR data: signal to noise ratio, in units of 0.1, e.g., 00: No information 01: Signal/noise = 0.1 . 99: Signal/noise = 9.9 or greater	'00'
53-54	Checksum - integer value = to the sum of digits in columns 1-52, modulo 100 (optional)	'51'

Note 1: In September 1999, the Jaguar Team concluded "*That ILRS make **NO RESTRICTION** on the minimum number of returns used to generate Normal Points.*"

Appendix A3 Stepwise variation charts for O-C residuals

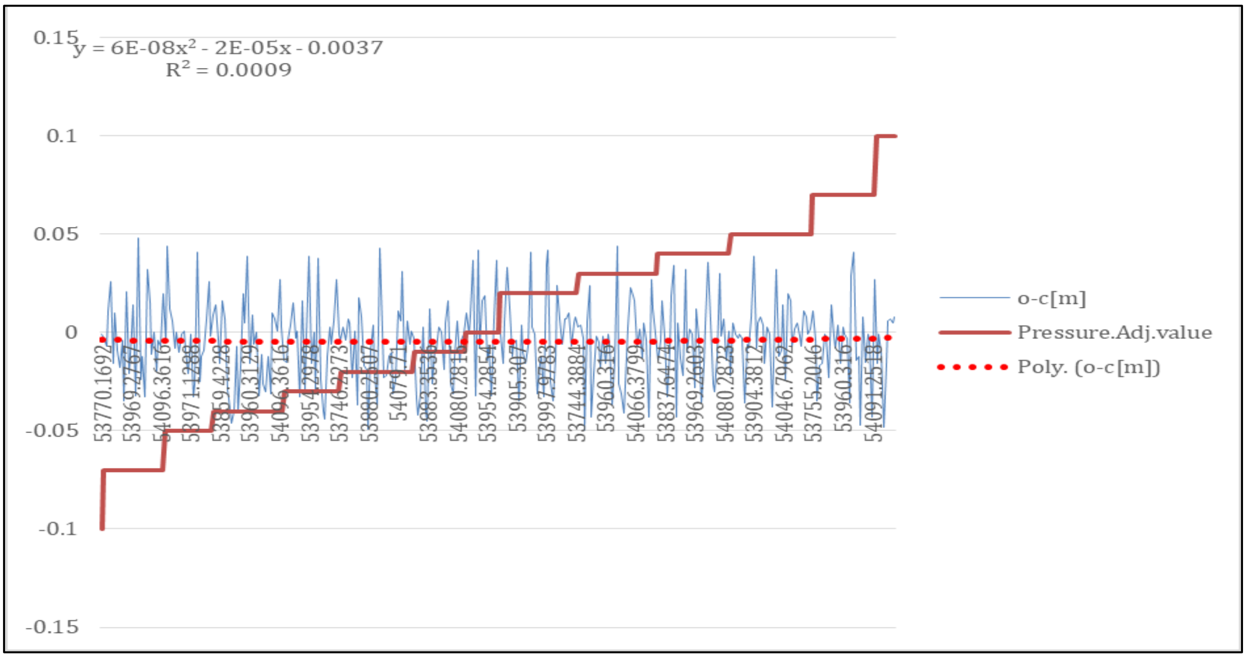

Figure 39. The O-C variations with stepwise adjustment of pressure for McDonald, USA.

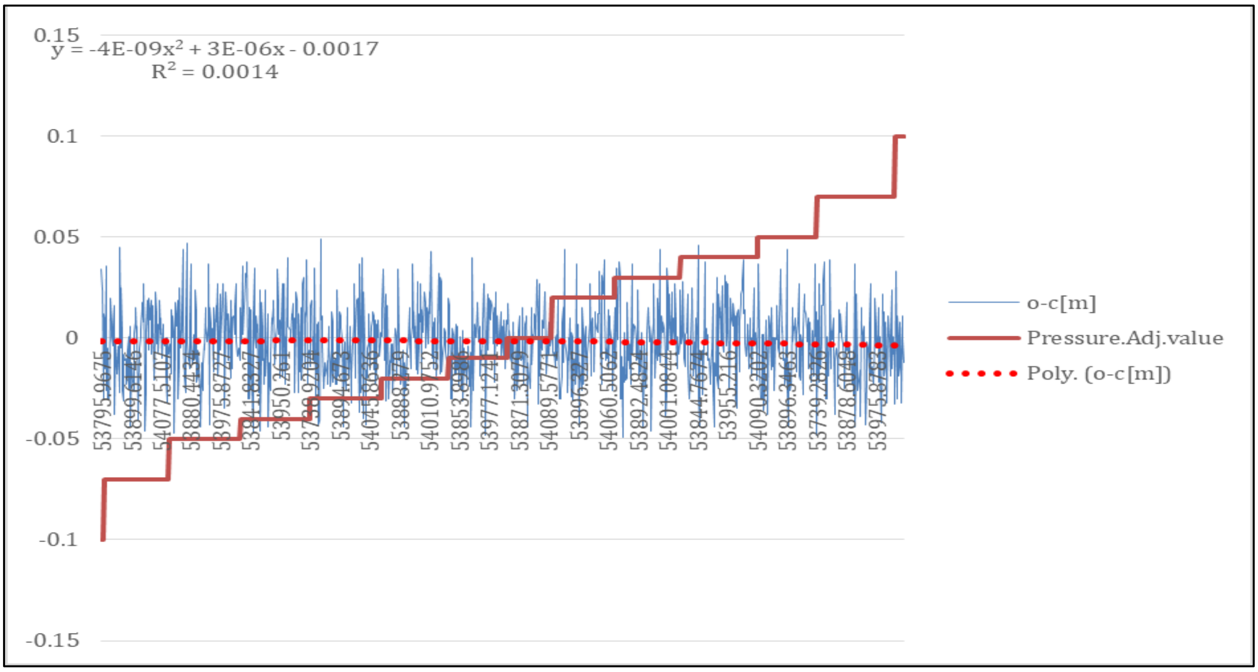

Figure 40. The O-C variations with stepwise adjustment of pressure for Monument Peak, USA.

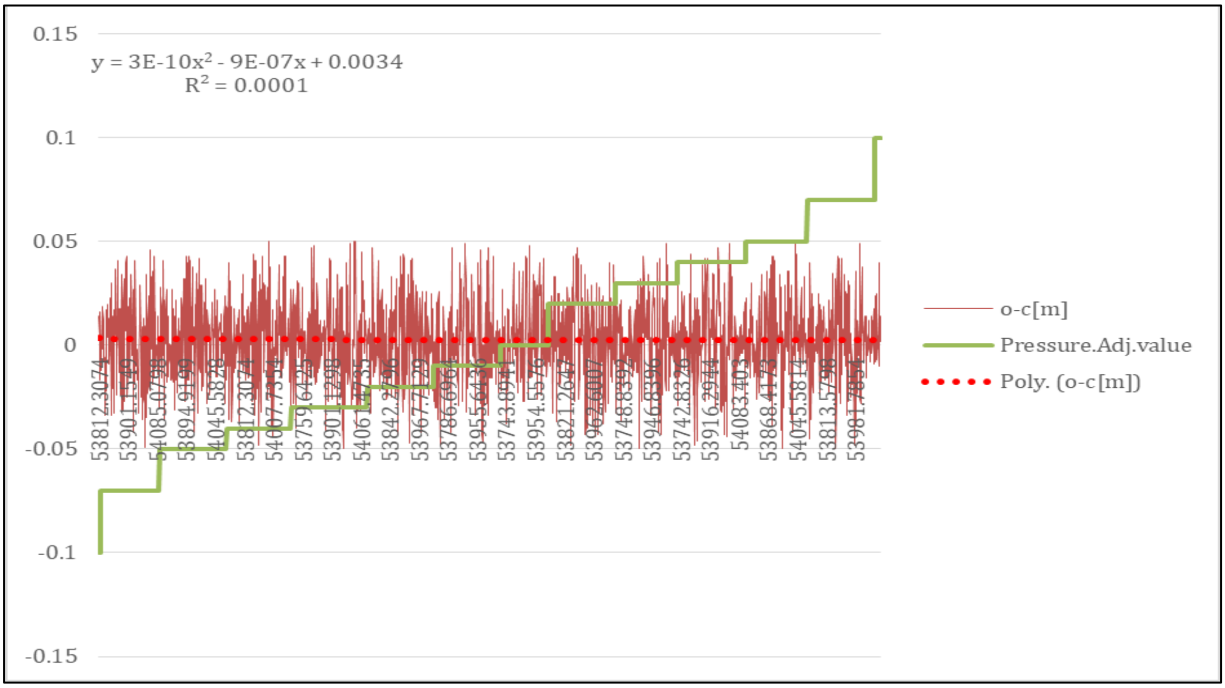

Figure 41. The O-C variations with stepwise adjustment of pressure for Zimmerwald, Switzerland.

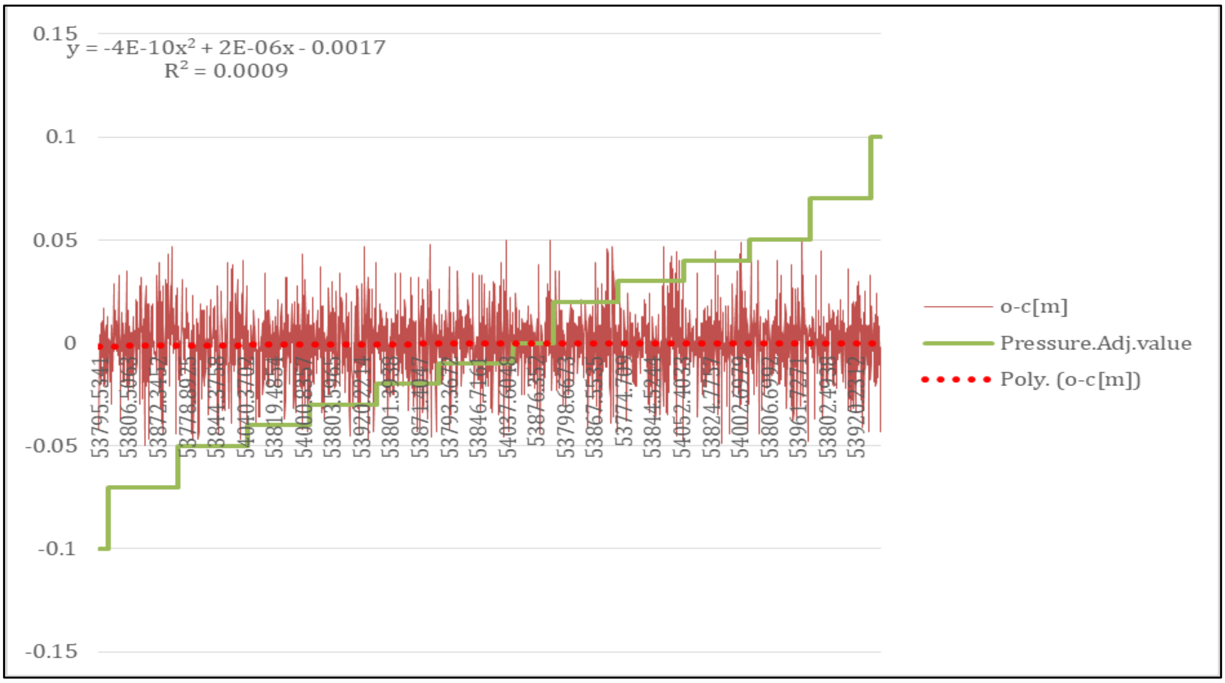

Figure 42. The O-C variations with stepwise adjustment of pressure for Mt. Stromlo, Australia.

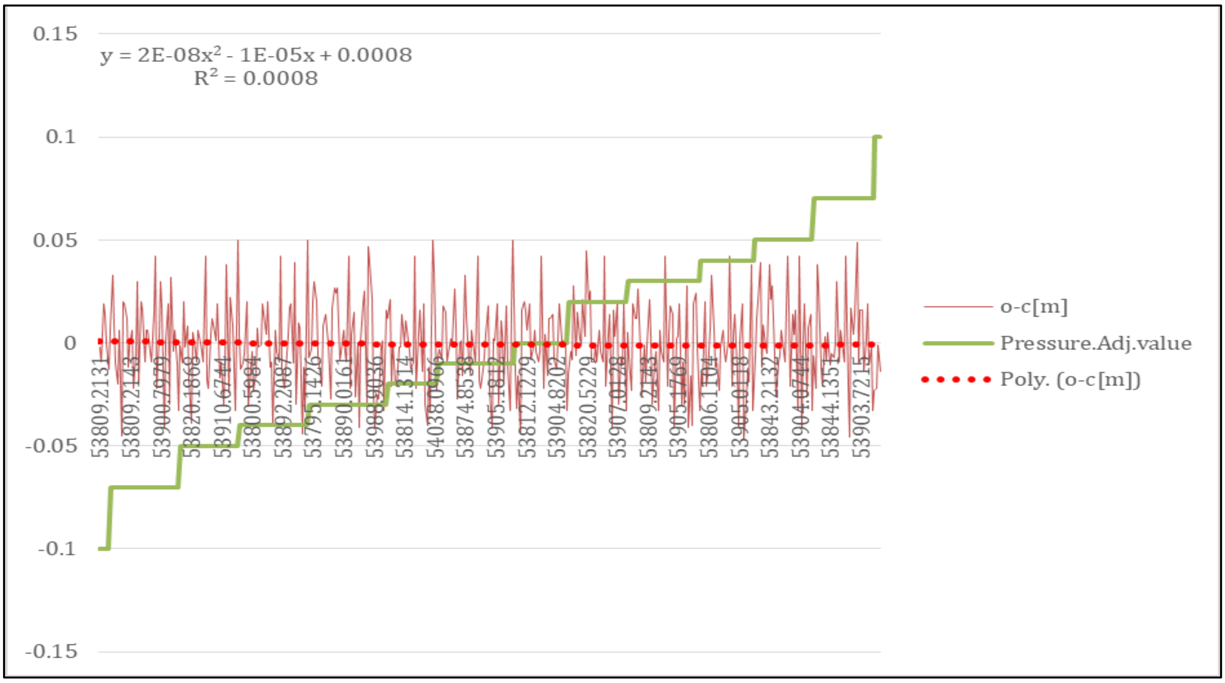

Figure 43. The O-C variations with stepwise adjustment of pressure for Riyadh, Saudi Arabia.

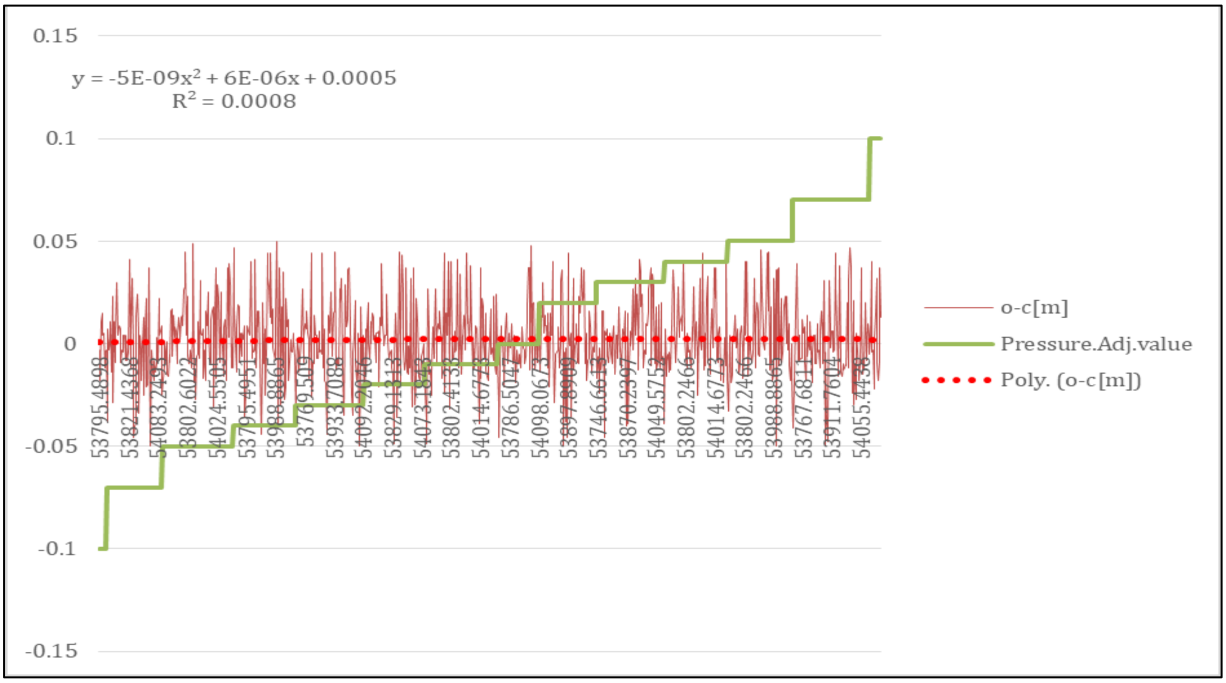

Figure 44. The O-C variations with stepwise adjustment of pressure for Graz, Austria.

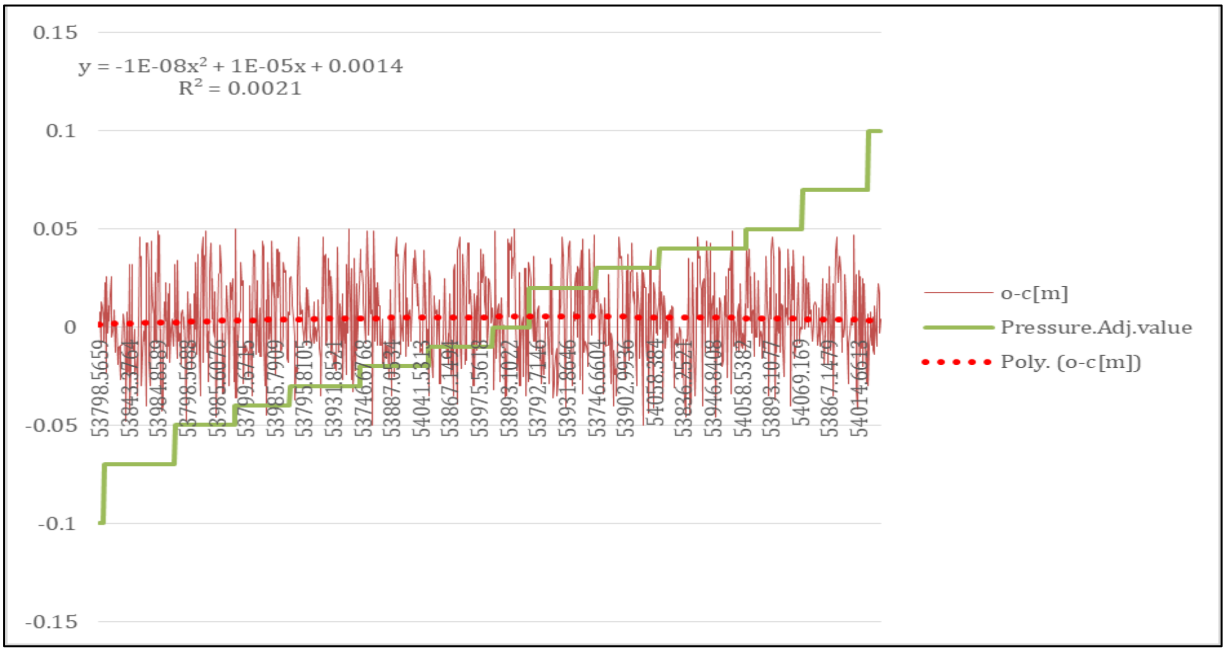

Figure 45. The O-C variations with stepwise adjustment of pressure for Hertmonceux, UK.

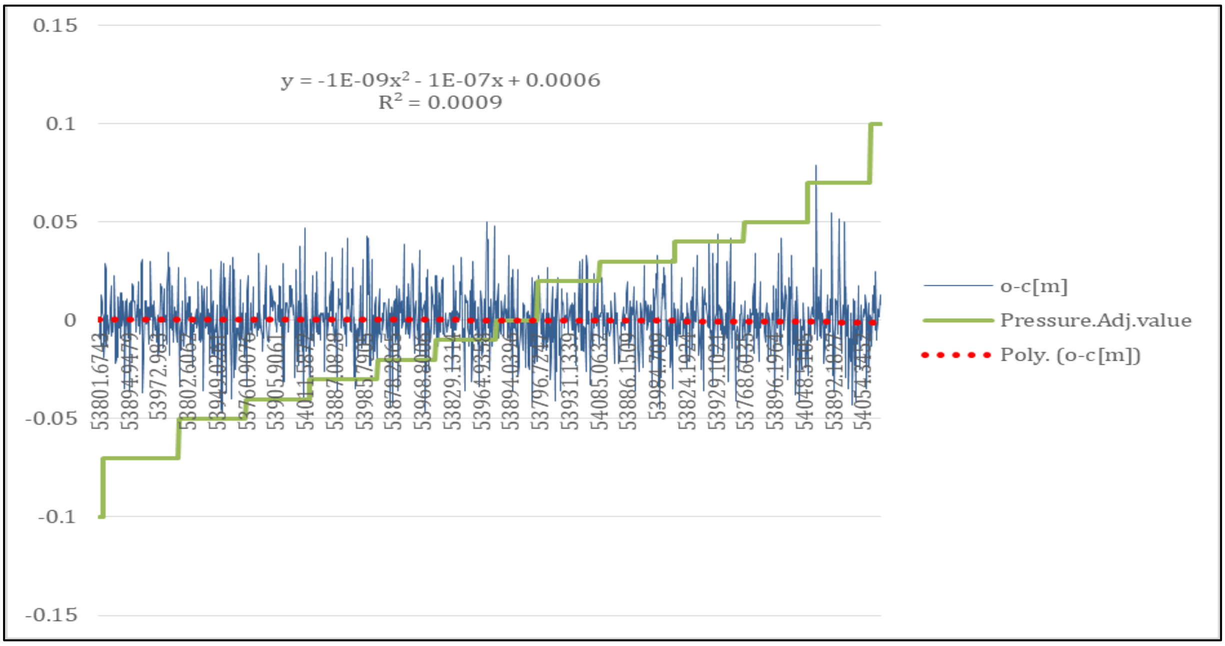

Figure 46. The O-C variations with stepwise adjustment of pressure for Matera, Italy.

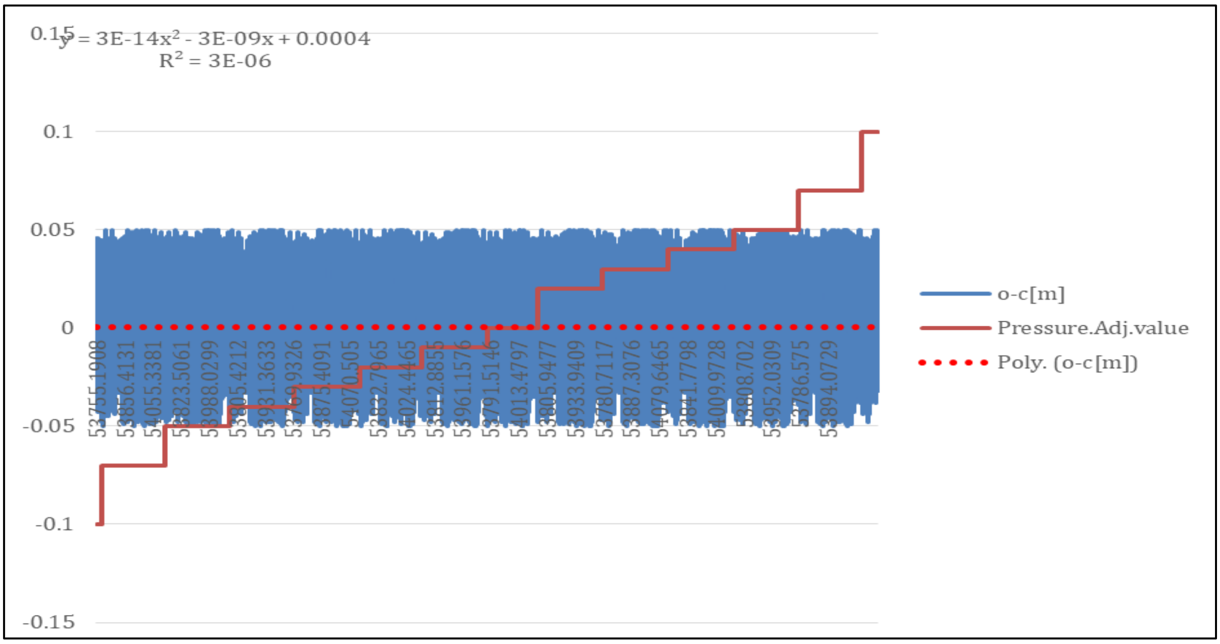

Figure 47. The O-C variations with stepwise adjustment of pressure for Greenbelt, USA.

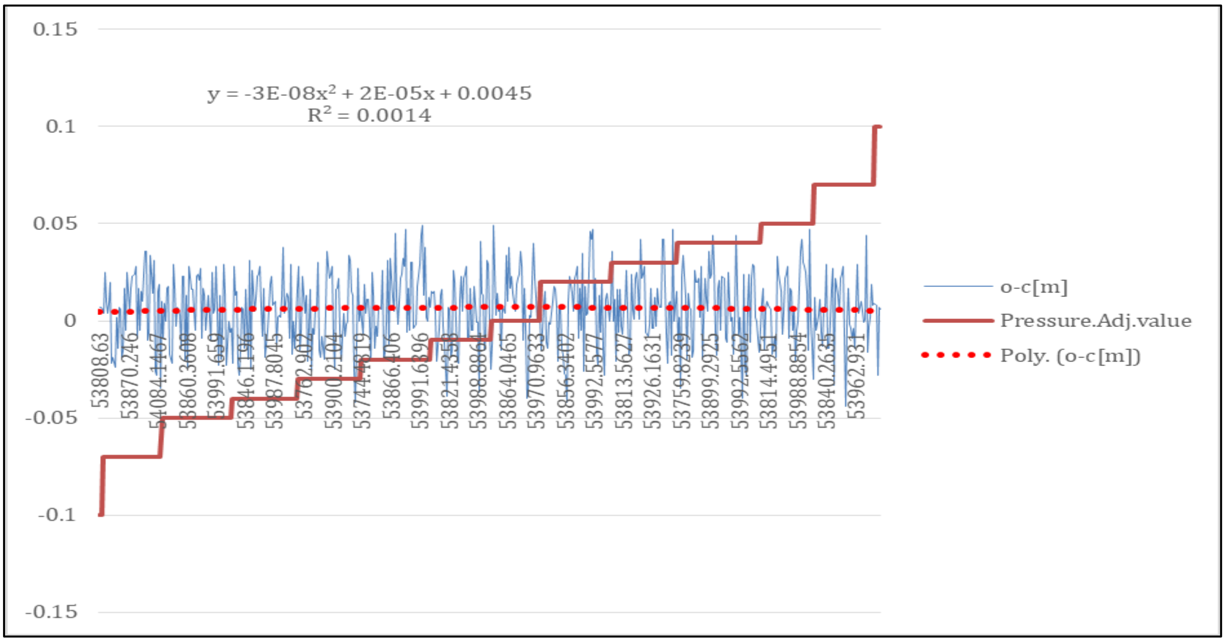

Figure 48. The O-C variations with stepwise adjustment of pressure for Wettzell, Germany.

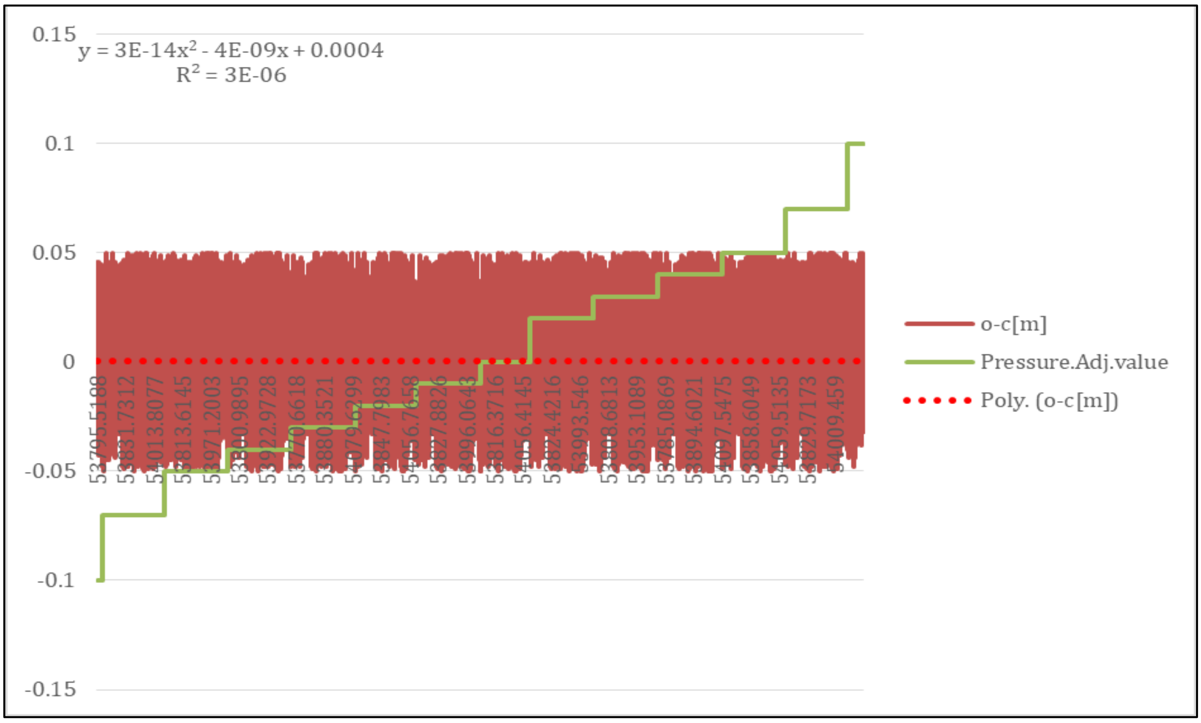

Figure 49. The O-C variations with stepwise adjustment of pressure for Yarragadee, Australia.

Appendix A4 Clustered O-C residuals at different pressure values

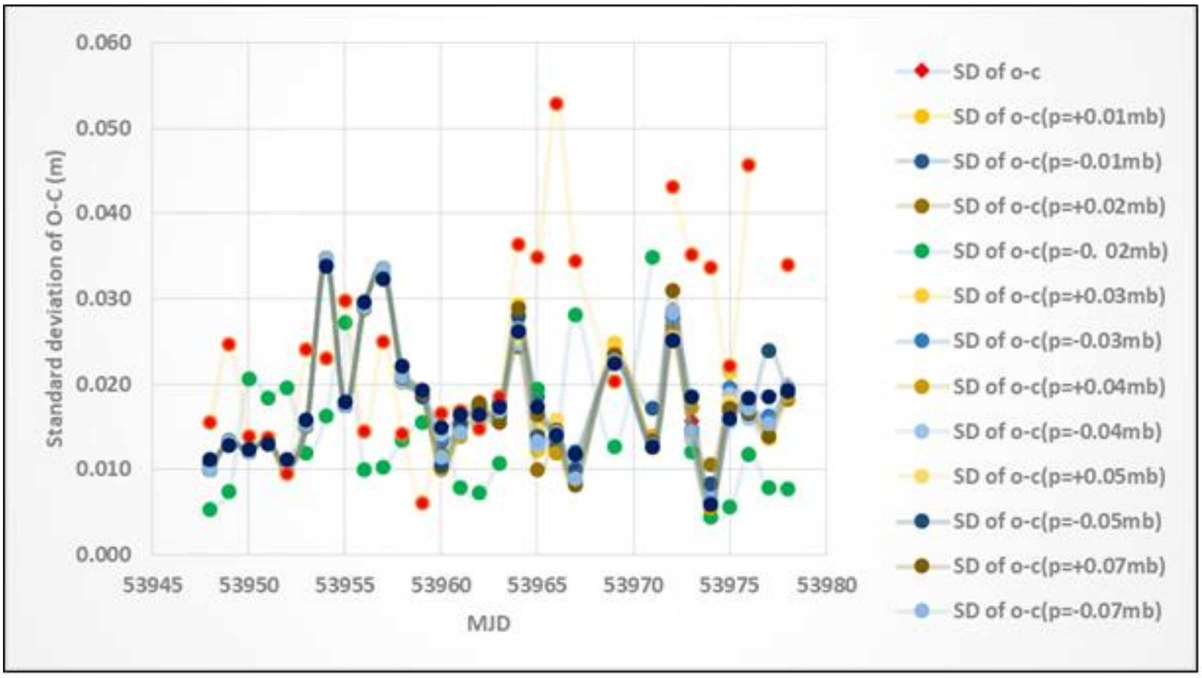

Figure 50. Standard deviation of O-C for August 2006.

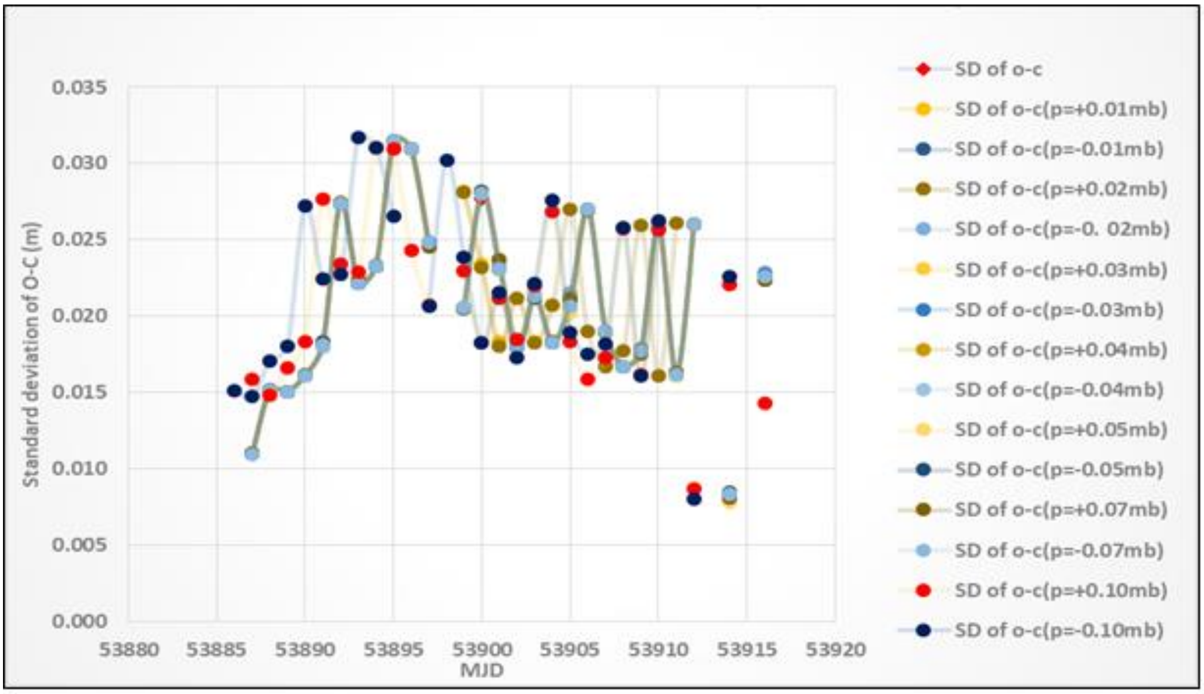

Figure 51. Standard deviation of O-C for June 2006.

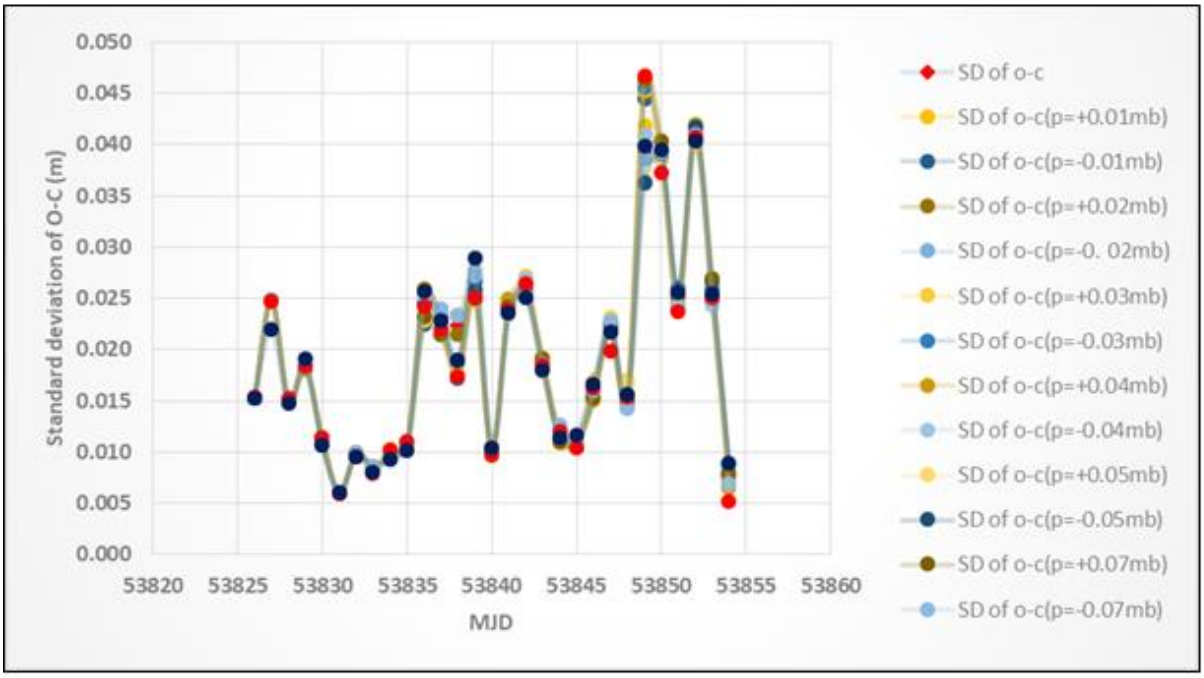

Figure 52. Standard deviation of O-C for April 2006.

Appendix A5 System Performance Standards (2015).

Source ILRS, 2018.

In 1996, at the International Workshop on Laser Ranging in Shanghai, the SLR community established a Satellite Pass Performance Standard of 1500 passes; this standard was adopted by the ILRS at the 1998 workshop in Deggendorf, Germany. The standard was broken down into LEO (1000 passes), LAGEOS (400 passes) and the newly introduced HEO satellites (100 passes). At the time, the ILRS had far fewer satellites on its tracking roster.

We recognized that stations had different cloud cover conditions, different levels of technology and operational readiness, and different staffing levels. The standard was set conservatively to give stations a target for improved performance on one hand and to recognize high achieving stations on the other.

Since that time our technologies have evolved, our procedures have improved, and we have considerably more ranging experience. We are more successful with daylight tracking and our retroreflector designs are more efficient. Above all, however, the number of targets has increased dramatically. As a result, it is now time to set a greater expectation. As of late 2015, the network is tracking 23 LEO satellites, 3 LAGEOS–class satellites (including LARES), and 30–50 HEO (including GNSS and GEO) satellites.

The Governing Board has set a new ILRS Pass Performance Standard at 3500 passes per year. In redefining the ILRS Pass Performance Standard we considered the following guidelines as a basis:

2 passes per week on each LEO satellite (2300 LEO passes per year)

4 passes per week on each LAGEOS satellite (600 LAGEOS passes per year)

2 passes per week on each HEO satellite (>3000 HEO passes per year)

Data quality guidelines are:

1 mm LAGEOS NP precision

5 mm short term bias stability (1)

2 mm long term bias stability (2)

(1) the standard deviation about the mean of the pass-by-pass range biases (see global report card - Monthly | Quarterly).

(2) the standard deviation of the monthly range bias estimates for at least 8 of the last 12 months (see global report card -

Monthly | Quarterly).

Operational compliance guidelines are:

Data delivery within 2 hours (data latency)

Specified ILRS NP data format (CRD)

Current site and system information form submitted and maintained (i.e., site log, system log)

Appendix A6 SLR Global Performance Report Card

April 1, 2017 through March 31, 2018.

Source ILRS, 2018.

The performance report card containing (see Table 13) performance parameters based on data volume, on-site processing statistics and operational compliance issues is presented. More information can be obtained from ILRS website https://ilrs.cddis.eosdis.nasa.gov.

Below are the detailed descriptions of each column in Table 13 *plots of the columns are linked in this description and in Table 1:*

- **Column 1** is the station location name.
- **Column 2** is the monument marker number.
- **Column 3** is the LEO pass total during the past 12 months.
- **Column 4** is the LAGEOS pass total during the past 12 months.
- **Column 5** is the high satellite pass total during the past 12 months.
- **Column 6** is the pass total (i.e., all satellites) during the past 12 months.
- **Column 7** is the LEO NP total during the past 12 months.
- **Column 8** is the LAGEOS NP total during the past 12 months.
- **Column 9** is the high satellite NP total during the past 12 months.
- **Column 10** is the NP total (i.e., all satellites) during the past 12 months.
- **Column 11** is the total tracking minutes (i.e., all satellites) during the past 12 months. *This is computed by the summation of the number of normal points multiplied by its bin size in minutes.*
- **Column 12** is the average single-shot calibration RMS, in millimetres, during the last quarter.
- **Column 13** is the average single-shot Starlette RMS, in millimetres, during the last quarter.
- **Column 14** is the average single-shot LAGEOS RMS, in millimetres, during the last quarter.

The first entry in each table is for the performance baseline goal. ***Note: There are no baseline goals for NP data quantities, single shot RMS's.***

Additional Notes: Blanks in any columns implies either that there was no data or that there was insufficient data. Only stations that have supplied data within the last year are included in the table. The table is sorted in descending order by total passes.

Table 13. Global performance report

Site Information		**Data Volume**									**Data Quality**		
Column 1	2	3	4	5	6	7	8	9	10	11	12	13	14
Location	Station Number	LEO pass Tot	LAGEOS pass Tot	High pass Tot	Total passes	LEO NP Total	LAGEOS NP Total	High NP Total	Total NP	Minutes of Data	Cal. RMS	Star RMS	LAG RMS
Baseline		2300	600	3000	3500								
Yarragadee	7090	15997	2775	10652	29424	287030	25798	41315	354143	195891	3.0	4.6	4.7
Changchun	7237	9446	1074	5685	16205	83408	6938	16193	106539	56267	7.0	7.8	9.6
Mount_Stromlo_2	7825	6774	1305	4213	12292	100003	10843	15107	125953	84956	3.3	4.6	7.5
Zimmerwald_532	7810	5992	940	3040	9972	102141	12743	9952	124836	84621	11.0	11.7	14.6
Herstmonceux	7840	4263	695	3444	8402	58848	8160	10717	77725	49885	3.4	9.2	12.3
Matera_MLRO	7941	4187	1527	2628	8342	49866	12972	11953	74791	65286	.9	2.8	3.1
Greenbelt	7105	5754	931	938	7623	111687	9395	3937	125019	74011	2.1	6.5	9.2
Monument_Peak	7110	5127	645	1133	6905	90793	4877	2934	98604	52715	4.9	7.6	9.3
Graz	7839	3235	449	2391	6075	66084	3127	12253	81464	41171	2.7	4.8	5.1
Wettzell	8834	3156	461	2203	5820	27712	2827	8171	38710	23695	7.0	8.5	12.0
Shanghai_2	7821	2510	549	2582	5641	22390	6043	10682	39115	30421	10.0	10.5	8.5
Potsdam_3	7841	4109	454	647	5210	70617	4331	3043	77991	42272	6.7	12.1	12.3
Wettzell_SOSW	7827	1534	351	2003	3888	15548	1893	5765	23206	12413	6.5	9.4	9.6
Hartebeesthoek	7501	2274	616	780	3670	32587	4495	3374	40456	29595	3.5	8.4	10.2
Beijing	7249	1843	366	1414	3623	15331	2545	5090	22966	16044	13.3	15.0	21.6
Kunming	7819	1813	308	1065	3186	25316	1475	3070	29861	15562	7.3	12.9	12.0
Altay	1879	244	345	2554	3143	4320	1973	9316	15609	7391			32.5
Haleakala	7119	2262	468	1	2731	35115	3604	3	38722	27134	2.7	6.6	7.9
Arequipa	7403	2479	113		2592	29218	615		29833	18199	6.0	7.1	
Simeiz	1873	1949	304	203	2456	22642	1933	951	25526	16342	21.1	11.3	14.3

Site Information		**Data Volume**									**Data Quality**		
Komsomolsk	1868	119	223	1988	2330	2036	1292	7304	10632	4630			31.6
Badary	1890	2036	129	90	2255	19300	635	301	20236	11212		27.8	27.8
Katzively	1893	1812	248	58	2118	19237	1916	329	21482	15469	27.0	10.3	9.9
Brasilia	7407	567	396	1099	2062	2085	1390	3915	7390	5363	37.5		32.8
Simosato	7838	1376	386	8	1770	21745	6152	28	27925	33104	4.1	6.9	11.1
Irkutsk	1891	1013	198	556	1767	9129	1621	1206	11956	9290	11.9	29.9	35.8
Papeete	7124	1030	184	437	1651	17665	1640	2212	21517	13061	6.9	8.5	9.8
Baikonur	1887	98	387	982	1467	607	1619	3629	5855	5419			31.2
Zelenchukskya	1889	739	170	310	1219	7457	1222	864	9543	7974		26.7	36.6
Arkhyz	1886	420	170	383	973	3282	769	1220	5271	4257		34.4	33.1
Riga	1884	732	55	19	806	13028	423	79	13530	6270	12.5	18.4	18.0
Grasse_MEO	7845	338	345	24	707	7977	4291	781	13049	18204	9.1		14.6
Borowiec	7811	518	129	4	651	8693	1352	22	10067	8130	11.3	17.9	15.3
Mendeleevo	1874	147	63	278	488	2690	995	871	4556	3859	-0.1		34.1
Kiev	1824	352	33		385	2404	180		2584	2119	11.4	27.1	26.9
McDonald	7080	314	42	1	357	2468	260	2	2730	2281	7.2	9.4	13.6
Sejong	7394	303	45	1	349	4350	461	5	4816	3912	4.0	8.7	10.9
Svetloe	1888	68	1	2	71	741	1	5	747	265			

Appendix A7 CRD Format Overview

Version V1.01

Due to recent technology changes, the existing International Laser Ranging Service (ILRS) formats for exchange of laser fullrate, sampled engineering and normal point data are in need of revision. The main technology drivers are the increased use of kilohertz firing rate lasers which make the fullrate data format cumbersome, and anticipated transponder missions, especially the Lunar Reconnaissance Orbiter (LRO), for which various field sizes are either too small or nonexistent. Rather than patching the existing format, a new flexible format encompassing the 3 data types and anticipated target types has been created.

The purpose of the Consolidated Laser Ranging Data Format (CRD) is to provide a flexible, extensible format for the ILRS fullrate, sampled engineering, and normal point data. The primary motivations for creating a new format at this time is to allow for transponder data, and to handle highrepetitionrate laser data without unnecessary redundancy. This format is based on the same features found in the ILRS Consolidated Prediction Format (CPF), including separate header and data record types assembled in a building block fashion as required for a particular target. There are 3 separate sections to the data format: 1) the header section which contains data on the such topics as station, target, and start time; 2) the configuration section containing an expanded version of data previously described by the SCI and SCH fields; and 3) the data section containing laser transmit and receive times, and other highly dynamic information. The data headers are fixed format and similar in content to those of the CPF files. The configuration and data records are free format with spaces between entries. Records can be added as needed for the specific data types and at frequencies commensurate with the data rate. For example, at a 2 kHz ranging rate, meteorological data and pointing angles are commonly read far less frequently than the ranges. Note that 1 way outbound, 1 way inbound, and 2 way ranges could all appear within one file. Also note that multiple colors could appear in one file.

Advantages of this format over the current ILRS formats are as follows:

- Flexibility. The data files can be simple and compact for kiloHertz ranging or comprehensive for more complex data structures, as appropriate.
- The building block structure with multiple record type allows for including and omitting certain records types as needed by a station or target.
- Configuration descriptions are addressed in a more explicit, logical and extensible manner than the current format.
- A single integrated format can be used for current and future data and target types.
- Multiple color data, multiple ranging modes (transponder one and twoway ranges) and multiple configurations can be included naturally within a single data file.
- The format can be expanded in the future as needs expand without abandoning the entire format.
- All data types (full rate, sampled engineering, and normal point) can be managed in a single file if desired, e.g., for archival and reference purposes.
- Extensibility to XML is provided for in the design.
- Fields in the Configuration sections are compatible with the SLR Engineering Data File (EDF) format.

Appendix A8 Summary statistics and ANOVA

Table 14. A monthly summary statistic for the data used to derive monthly average of standard deviation of O-C vs station range bias (m) after adjusting met unit by -1 m.

SUMMARY OUTPUT

Regression Statistics	
Multiple R	0.473245236
R Square	0.223961053
Adjusted R Square	0.126956185
Standard Error	0.001244255
Observations	10

ANOVA

	df	*SS*	*MS*	*F*	*Significance F*
Regression	1	3.57436E-06	3.57436E-06	2.308760962	0.167132014
Residual	8	1.23854E-05	1.54817E-06		
Total	9	1.59597E-05			

	Coefficients	*Standard Error*	*t Stat*	*P-value*	*Lower 95%*	*Upper 95%*	*Lower 95.0%*	*Upper 95.0%*
Intercept	-0.000619471	0.000405664	-1.527055551	0.165264742	-0.001554933	0.000315991	-0.001554933	0.000315991
Monthly Average of o-c(m)	-0.099225554	0.065303137	-1.519460747	0.167132014	-0.249814858	0.051363751	-0.249814858	0.051363751

Table 15. A weekly statistical summary of the data used in the weekly average of the standard deviation of O-C vs station range bias (m) after adjusting met unit by -1 m.

SUMMARY OUTPUT

Regression Statistics	
Multiple R	0.266997
R Square	0.071287
Adjusted R Square	0.04033
Standard Error	0.003111
Observations	32

ANOVA

	df	*SS*	*MS*	*F*	*Significance F*
Regression	1	2.23E-05	2.23E-05	2.302777	0.139611
Residual	30	0.00029	9.68E-06		
Total	31	0.000313			

	Coefficients	*Standard Error*	*t Stat*	*P-value*	*Lower 95%*	*Upper 95%*	*Lower 95.0%*	*Upper 95.0%*
Intercept	-0.00055	0.000558	-0.99027	0.329962	-0.00169	0.000587	-0.00169	0.000587
Average of o-c(m)	0.076751	0.050577	1.51749	0.139611	-0.02654	0.180044	-0.02654	0.180044

Table 16. Daily statistical summary of the daily average of standard deviation of O-C vs station range bias (m) after adjusting the met unit by -1 m.

SUMMARY OUTPUT

Regression Statistics	
Multiple R	0.233391
R Square	0.054471
Adjusted R Square	0.036288
Standard Error	0.004811
Observations	54

ANOVA

	df	*SS*	*MS*	*F*	*Significance F*
Regression	1	6.93E-05	6.93E-05	2.99568	0.089417
Residual	52	0.001203	2.31E-05		
Total	53	0.001273			

	Coefficients	*Standard Error*	*t Stat*	*P-value*	*Lower 95%*	*Upper 95%*	*Lower 95.0%*	*Upper 95.0%*
Intercept	-0.00079	0.000669	-1.17646	0.244767	-0.00213	0.000555	-0.00213	0.000555
Average of o-c(m)	0.09563	0.055252	1.730803	0.089417	-0.01524	0.206502	-0.01524	0.206502

Table 17. Monthly statistical summary of the daily average of standard deviation of O-C vs station range bias (m) for the baseline (no adjustment made to pressure).

SUMMARY OUTPUT

Regression Statistics	
Multiple R	0.122978
R Square	0.015123
Adjusted R Square	-0.14902
Standard Error	0.001339
Observations	8

ANOVA

	df	*SS*	*MS*	*F*	*Significance F*
Regression	1	1.65E-07	1.65E-07	0.092134	0.771731
Residual	6	1.08E-05	1.79E-06		
Total	7	1.09E-05			

	Coefficients	*Standard Error*	*t Stat*	*P-value*	*Lower 95%*	*Upper 95%*	*Lower 95.0%*	*Upper 95.0%*
Intercept	-0.00054	0.000477	-1.12253	0.304538	-0.0017	0.000632	-0.0017	0.000632
Average of o-c(m)	-0.03635	0.119757	-0.30354	0.771731	-0.32939	0.256684	-0.32939	0.256684

Table 18. Weekly statistical summary of the daily average of standard deviation of O-C vs station range bias (m) for the baseline (no adjustment made to pressure).

SUMMARY OUTPUT

Regression Statistics	
Multiple R	0.131663
R Square	0.017335
Adjusted R Square	-0.02946
Standard Error	0.002233
Observations	23

ANOVA

	df	*SS*	*MS*	*F*	*Significance F*
Regression	1	1.85E-06	1.85E-06	0.37046	0.549281
Residual	21	0.000105	4.99E-06		
Total	22	0.000107			

	Coefficients	*Standard Error*	*t Stat*	*P-value*	*Lower 95%*	*Upper 95%*	*Lower 95.0%*	*Upper 95.0%*
Intercept	-0.00028	0.000471	-0.59054	0.561133	-0.00126	0.000701	-0.00126	0.000701
Weekly average of o-c(m)	0.021653	0.035575	0.608655	0.549281	-0.05233	0.095635	-0.05233	0.095635

Table 19. Daily statistical summary of the daily average of standard deviation of O-C vs station range bias (m) for the baseline (no adjustment made to pressure).

SUMMARY OUTPUT

Regression Statistics	
Multiple R	0.371500
R Square	0.138012
Adjusted R Square	0.114715
Standard Error	0.004402
Observations	39

ANOVA

	df	*SS*	*MS*	*F*	*Significance F*
Regression	1	0.000115	0.000115	5.924036	0.019882
Residual	37	0.000717	1.94E-05		
Total	38	0.000832			

	Coefficients	*Standard Error*	*t Stat*	*P-value*	*Lower 95%*	*Upper 95%*	*Lower 95.0%*	*Upper 95.0%*
Intercept	-0.0006	0.000712	-0.83597	0.408539	-0.00204	0.000847	-0.00204	0.000847
Daily average of o-c(m)	0.118232	0.048576	2.433934	0.019882	0.019807	0.216657	0.019807	0.216657

Table 20. Monthly statistical summary of the daily average of standard deviation of O-C vs station range bias (m) after adjusting pressure by +1.0 mbar.

SUMMARY OUTPUT

Regression Statistics	
Multiple R	0.449270
R Square	0.201844
Adjusted R Square	0.102074
Standard Error	0.003175
Observations	10

ANOVA

	df	*SS*	*MS*	*F*	*Significance F*
Regression	1	2.04E-05	2.04E-05	2.023097	0.19272
Residual	8	8.06E-05	1.01E-05		
Total	9	0.000101			

	Coefficients	*Standard Error*	*t Stat*	*P-value*	*Lower 95%*	*Upper 95%*	*Lower 95.0%*	*Upper 95.0%*
Intercept	-0.00113	0.001007	-1.11746	0.29623	-0.00345	0.001197	-0.00345	0.001197
Monthly Average of o-c(m)	0.188486	0.132517	1.422356	0.19272	-0.1171	0.49407	-0.1171	0.49407

Table 21. Weekly statistical summary of the daily average of standard deviation of O-C vs station range bias (m) after adjusting pressure by +1.0 mbar.

SUMMARY OUTPUT

Regression Statistics	
Multiple R	0.268801
R Square	0.072254
Adjusted R Square	0.036571
Standard Error	0.00371
Observations	28

ANOVA

	Df	*SS*	*MS*	*F*	*Significance F*
Regression	1	2.79E-05	2.79E-05	2.024912	0.166627
Residual	26	0.000358	1.38E-05		
Total	27	0.000386			

	Coefficients	*Standard Error*	*t Stat*	*P-value*	*Lower 95%*	*Upper 95%*	*Lower 95.0%*	*Upper 95.0%*
Intercept	-0.00079	0.000702	-1.13252	0.267751	-0.00224	0.000648	-0.00224	0.000648
Weekly Average of o-c(m)	0.083474	0.058661	1.422994	0.166627	-0.03711	0.204053	-0.03711	0.204053

Table 22. Daily statistical summary of the daily average of standard deviation of O-C vs station range bias (m) after adjusting pressure by +1.0 mbar.

SUMMARY OUTPUT

Regression Statistics	
Multiple R	0.335388
R Square	0.112485
Adjusted R Square	0.092762
Standard Error	0.006109
Observations	47

ANOVA

	df	*SS*	*MS*	*F*	*Significance F*
Regression	1	0.000213	0.000213	5.703363	0.02119
Residual	45	0.001679	3.73E-05		
Total	46	0.001892			

	Coefficients	*Standard Error*	*t Stat*	*P-value*	*Lower 95%*	*Upper 95%*	*Lower 95.0%*	*Upper 95.0%*
Intercept	-0.00149	0.000898	-1.657	0.104477	-0.0033	0.000321	-0.0033	0.000321
Daily Average of o-c(m)	0.13309	0.055729	2.388172	0.02119	0.020846	0.245333	0.020846	0.245333